GEOPOLYMER-DERIVED CERAMICS AND COMPOSITES

BY

ANDREW JACOB STEVESON

DISSERTATION

Submitted in partial fulfillment of the requirements
for the degree of Doctor of Philosophy in Materials Science and Engineering
in the Graduate College of the
University of Illinois at Urbana-Champaign, 2020

Urbana, Illinois

Doctoral Committee:

Professor Waltraud M. Kriven, Chair and Director of Research
Emeritus Professor Jay D. Bass
Professor David A. Lange
Assistant Professor Jessica A. Krogstad
Assistant Professor C. Robert E. Maaß

ABSTRACT

The development of ceramics and composites from geopolymer precursors is leading to exciting new avenues in ceramic synthesis and composite applications. In this work, we developed, synthesized, and characterized materials derived from geopolymers for use in extreme environments.

In the first section, a method of engineering tectosilicate material systems with tailorable thermal expansion was developed with the goal of designing new candidate materials for environmental barrier applications. The materials were studied with *in situ* high temperature synchrotron X-ray diffraction to explore the atomic mechanisms responsible for the thermal evolution of these compounds. The framework distortions identified were then systematically manipulated to give tailored thermal expansion values. Several material candidates were identified for environmental barrier coating applications.

Rule of mixtures models were used to predict unit cell volumes and thermal expansion coefficients for compounds of intermediate composition. The error in such predictions did not exceed 0.19% (4.98 $Å^3$) in unit cell volume and 0.132 10^{-5}/°C (9.13%) in thermal expansion coefficients.

In the second section, geopolymer matrix composites were developed to improve the toughness over unreinforced geopolymers. The ultimate flexure strengths in 3-point bending of fiber-reinforced and minibar-reinforced composite systems were 20% and 59% higher than that of the pure potassium geopolymer, respectively; ultimate compressive strengths were 41% and 36% lower; and fracture toughness was 936% and 4243% higher, as measured by the single-edge notched beam method.

ACKNOWLEDGEMENTS

I would like to thank my family and friends for their love and support through this process: Emily Steveson, Ada Steveson, Shunda Steveson, Sarah Steveson, Barry Steveson, and Penny Hodgins. You are my foundation.

I would like to thank my friends and colleagues for discussions about research and everything but research, when the time called for it: Doctor Steven Letourneau, Doctor Kevin Seymour, Ben Hulbert, Professor Scott McCormack, Kuo-Pin Tseng, Patrick Szuta, Brian Rice, Doctor Robert Hughes, Curtis and Michelle Royse, Matthew Greenberg, Mark Huls, Norman Anderson, Sarah Christensen, Chase Bonhag, Collins Okafur, Devna Sharma, Cindy Lu, Zachary and Amanda Jones, and Sean and Ashlei Musil. Your friendship has enriched my journey.

I would lastly like to thank my mentors, inside and outside the laboratory, for their grace, patience, and wisdom: Professor Waltraud Kriven, Professor Pankaj Sarin, Jack McVicker, Mark Lockwood, Professor Jeffrey Lowenstein, and Dr. Christian Schlepütz. Your insight and guidance have made this work possible.

To the journey

TABLE OF CONTENTS

CHAPTER 1 – INTRODUCTION AND BACKGROUND

The synthesis and properties of crystalline alkali aluminosilicate materials offer some exciting research opportunities. As some of the most abundant minerals in the earth's crust, geologists have naturally contributed most of the scientific understanding of these materials. The purity and composition of geological samples vary with their geographic origin as do their characteristic properties (e.g. melting point, thermal expansion, phase transitions). Engineering applications, however, necessitate material systems with reliable properties. As minerals with excellent refractory properties, the alkali aluminosilicates are attractive for a wide range of high temperature applications. In order to take advantage of these materials, synthetic pathways to high purity samples and systematic characterization of their properties are crucial. This has utility in both the fundamental scientific understanding of alkali aluminosilicates and possible other related systems, as well as substantial potential for engineering applications. The goal of this thesis is to establish a facile synthetic route to high-purity, crystalline alkali aluminosilicate materials, describe the temperature-driven structural changes in air at atmospheric pressure, and to demonstrate chemical modification of their crystal structures to produce tailorable bulk properties.

Environmental Barrier Coating (EBC) Systems

Gas turbine engines generate about 20% of the world's electricity and propel commercial and military aircraft.[1] Because of this, there is continuous, strong demand for more efficient and powerful engines. The efficiency and power of these systems scale with the gas inlet temperature in the hottest part of the engine, the "hot sections". Thus, increasing the high temperature tolerance of parts in these sections is a primary theme in research efforts for gas turbine technology. The advent of silicon carbide fiber/silicon carbide ceramic matrix composite

(SiC_f/SiC CMC) components for hot sections in turbine engines are enabling drastic improvements in thermodynamic efficiency over the previous generations of nickel superalloy-based components (Figure 1).[2] The CMC components exhibit exceptional dimensional stability over a wide range of temperatures, lower density than metallic parts, and better mechanical properties at high temperatures.

A central limitation in the utilization of SiC_f/SiC CMC parts is chemical attack during operation at high temperature. At typical operating temperatures and pressures, SiC is oxidized to vitreous silica and cristobalite by reaction with water vapor, which is a by-product of the combustion of organic fuels. This reaction leads to unacceptably high recession rates of the structural components, on the order of millimeters per hour.[3], [4] Protection from such deleterious reactions has been the impetus behind the development of environmental barrier coating (EBC) and thermal/environmental barrier coating systems (TBC/TEBC), the latter of which incorporates additional refractory coating layers to enhance the high temperature capabilities of the system.

Because the chemical protection of the CMC is the main function of the EBC, candidate materials are typically refractory silicate ceramics with low water permeability, silica activity, and thermal expansion in the operating temperature range. Because oxide materials typically do not bond well to the non-oxide CMC materials, a bond coat of Si is applied. This bond coat is thermally oxidized to silica, SiO_2, to promote bonding as well as to passivate the surface of the CMC to further oxidation. When exposed to water vapor at operating temperatures and pressures, however, the protective SiO_2 layer is volatilized to $Si(OH)_4$ gas.[5] If the SiO_2 layer is depleted, this can lead to debonding of the EBC layer. Therefore, silica activity of the EBC

material defines the chemical susceptibility of the EBC to water in the same way that the permeability to water defines its physical susceptibility.[5], [6]

The rare earth disilicates, $RE_2Si_2O_7$ or $RE_2O_3 \cdot 2\ SiO_2$ (RE = Ce, Dy, Er, Eu, Gd, Ho, La, Lu, Nd, Pr, Pm, Sm, Sc, Tb, Tm, Yb, Y) are the most popular choice for EBC materials and are already in commercial use. These materials are grown by physical vapor deposition the bond layer. They are highly refractory and exhibit low silica activity. As an example, the melting point of $Y_2Si_2O_7$ is 1780 ℃ and its silica activity, a_{SiO2}, is approximately 0.33.[7] The central constraint of this system is that the thermal expansion mismatch between adjacent layers must be small in order to prevent cracking and delamination. Thus, the range of candidate material systems is limited.

The most common growth methods for EBCs and related systems are vapor deposition techniques, the most advanced being plasma spray-physical vapor deposition (PVD). This process uses a high-energy plasma gun to vaporize ceramic powder in a low-pressure environment. Pressure from the plasma jet propels the powder towards the substrate surface. This procedure can generate high growth rates and excellent coverage of complex parts.[8]

Geopolymer Science

Geopolymer materials are nanoporous framework aluminosilicate structures.[9] The framework backbone is composed of silicate ($[SiO_4]^{4-}$) and aluminate ($[AlO_4]^{5-}$) tetrahedral units arranged in three-dimensional glass-like networks. Alkali cations serve as network modifiers by coordinating with unshared oxygen atoms in the framework and are randomly distributed in pores throughout the framework (Figure 2).[10]–[13] These materials are X-ray amorphous, typically displaying a characteristic, broad “amorphous hump” centered around approximately 22 degrees 2-theta in X-ray diffraction experiments using a Copper Kα radiation source.

Geopolymers are most widely used as an alternative construction material to concrete. In this work, however, the formation of geopolymers was exploited as a facile, low-energy synthetic route to crystalline ceramics.

Crystalline phase formation in geopolymers was first reported by Rahier in 1997.[14] Subsequent studies were aimed at elucidating the compositional and processing variables that affect crystalline phase formation. For structural applications, it is ideal to resist the crystallization of the amorphous phase. It was discovered that the thermal stability of the amorphous geopolymer phase is strongly dependent upon stoichiometry. Formation of crystalline phases was found to be promoted by high curing temperatures (the temperature at which the geopolymer gel sets), high aluminum oxide (Al_2O_3) content, small interframework cation size, low SiO_2 content and aging time (metastability of the geopolymer phase naturally leads to crystallization after some time has passed).[14]–[19]

The local structure of geopolymers, within 1-2 nearest neighbor atoms, is identical to that of framework zeolites of equivalent compositions. X-ray pair distribution function (PDF) experiments showed that the potassium- and cesium-based geopolymers have the same short-range, <approximately 4Å, as the minerals leucite, $K[AlSi_2O_6]$ or $K_2O{\cdot}Al_2O_3{\cdot}4SiO_2$, and pollucite, $Cs[AlSi_2O_6]$ or $Cs_2O{\cdot}Al_2O_3{\cdot}4SiO_2$, respectively (Figure 3).[20], [21] These results were confirmed by neutron pair distribution function experiments, which gave better information about the position of oxygen atoms.[22] Magic angle spinning nuclear magnetic resonance (MAS NMR) spectral studies of the Aluminum-27 and Silicon-29 nuclei showed that fully-reacted geopolymers are dominated by Q^4-linked aluminate and silicate species (Figure 4).[19], [23]–[25] This indicates that these species are primarily found as fully-linked, corner-sharing tetrahedra. In context, the extent of “order” are the boundaries of the aluminate and silicate

tetrahedral units of the framework. In the intermediate range, 4-8Å, the crystalline models were poorer fits. This reflects a moderate amount of patterning of inter-tetrahedral bonds, which can be explained by the tendency of these frameworks to avoid Al-O-Al bonds due to the high energetic cost relative to Al-O-Si bonds.[26] Beyond 8Å, no detectable order exists in the atomic structure of geopolymers.

On heat treatment to an appropriate temperature, the long-range structure of potassium and cesium geopolymers undergo reorganization. The local structure of aluminate and silicate tetrahedra are retained.[19] The loss of coordinating water molecules and surface hydroxyl, $[OH]^-$, groups gives rise to the consolidation of Q^3- and lower-linked tetrahedral groups.[27]

In 2009, Bell reported the first purposeful crystallization of geopolymers as a synthetic route for ceramics.[28], [29] They found that geopolymers of the formula $M_2O{\cdot}Al_2O_3{\cdot}4SiO_2{\cdot}11H_2O$, with M = K, Cs, crystallized to form multiphase ceramics when heated above a critical temperature and quenched. Potassium-based geopolymer crystallized to form multi-phase tetragonal leucite ($K[AlSi_2O_6]$) and kalsilite ($K[AlSiO_4]$) ceramics above 1000℃ and achieved 99.7% theoretical density of leucite by 1100℃ (Figure 5).[28] Cesium-based geopolymers crystallized to form cubic pollucite when heated above 900℃ and achieved 98% theoretical density by 1600℃ (Figure 6).[29] After heating geopolymers of the composition $M_2O{\cdot}Al_2O_3{\cdot}5SiO_2{\cdot}11H_2O$, with M = K, Na, to 1000℃, Duxson reported an approximately 30% amorphous-to-ceramic conversion rate to nepheline ($NaAlSi_2O_4$) in sodium-based geopolymer and a mixture of kaliophilite ($K[AlSiO_4]$) and leucite ($K[AlSi_2O_6]$) in potassium-based geopolymer.[15]

Research on geopolymer systems with multiple alkali cations is sparse. One study previously mentioned studied sodium-potassium systems.[15] On heating, development of multiple crystalline phases were observed. Most recently, an investigation into the potassium-cesium system of the stoichiometry $M_2O{\cdot}Al_2O_3{\cdot}5SiO_2{\cdot}11H_2O$ revealed modification of phase transition behavior in crystalline leucite-pollucite ceramics.[30] The general details of the phase transition behavior in these systems is addressed in Chapter 3.

To produce the polycrystalline powders which are the subject of this thesis, geopolymers were heat treated to induce crystallization. This work began as an investigation into the high temperature phase formation and dynamics of geopolymer materials. In this process, geopolymer crystallization has proven to be a reliable synthetic method for producing crystalline alkali aluminosilicates. Other synthetic methods have been employed in the literature, including ion exchange [31], hydrothermal synthesis [32], and organic steric entrapment [33], but the geopolymer crystallization approach has some distinct advantages.

Geopolymer crystallization does not require specialized or hazardous laboratory equipment, like the mineralization bomb required for hydrothermal syntheses. This is an advantage both for practical accessibility as well as for scaling up the production process.

The only byproduct of the geopolymer crystallization process is water vapor. Sol gel processing routes and the organic steric entrapment method both require the use of nitrate precursors and organic additives during processing. In order to recover the final product, these materials are burned off, producing NO_x and CO_x gases, both of which are greenhouse gases.

Amorphous geopolymer materials are synthesized by the reaction of an alkali silicate solution with a clay mineral. Commercial variations of both reactants are available, but the poor

stoichiometric control of commercial silicate solutions inspired the development of our own process for producing solutions of higher quality. Commercial products are already improving in quality, due in part to research being conducted in the Kriven group.

Framework aluminosilicates (tectosilicates)

In general, framework aluminosilicate structures are three-dimensional networks of corner-sharing aluminate and silicate tetrahedra that form cages of various shapes in their interstices (Figure 7).[34] The cages can be occupied by cations, positively charged ionic molecular groups (e.g. NH^{4+}), or water molecules.[35] Structures that fall under this definition include alkaline and alkaline earth glasses, the feldspars, the feldspathoids, the scapolites, the zeolites, and several other types of compounds.

The framework units display sp^3-hybridization with four oxygens surrounding central silicon (Si^{2+}) or aluminum (Al^{3+}) cations. These units are relatively rigid compared to the overall framework.[36], [37] Therefore, reorientation of the tetrahedral framework without the breaking of bonds in response to an imposed stress or strain can require much less energy than distortion of the tetrahedra.

The relative motion of tetrahedra is constrained by the framework arrangement and the cations present, both in the interstices and in the tetrahedral centers. Interstitial cations serve to charge-balance the tetrahedral units and “open” the framework by promoting larger inter-tetrahedral bonding angles (Figure 8). The opening effect increases with the size of the cation. The similarity between the framework-opening distortion and that of many temperature-induced distortions and phase transition has drawn some natural comparisons between the structural changes associated with increasing temperature and those associated with increasing cation size, but the similarity is superficial. Because increasing temperature involves increasing the effective

size of interstitial cations *and* those of all other atoms, the comparison does not convey a complete picture of temperature-induced structural changes.

Crystallography and X-ray Radiation

In 1611, Johannes Kepler first hypothesized the regular packing of crystalline materials on the molecular scale after observing the symmetry of falling snowflakes. Over the next three centuries, scientists further developed the hypothesis through systematic observations of crystal faces (Steno, Haüy, and Miller) and mathematical reasoning (Hessel, Bravais, Fedorov, Schönflies, and Barlow) that led to the complete descriptions of all the possible three-dimensional crystal symmetries before the first direct observation of crystalline atomic order was ever made.

In 1895, Röntgen discovered X-ray radiation. The applications were numerous and rapid. The contributions of Compton, Laue, Ewald, W.H. Bragg, and W.L. Bragg set the stage for the physical understanding of X-rays and diffraction events to be applied to studies of crystalline materials.

Debye and Scherrer developed the methods of powder diffraction to apply the techniques of single crystal diffraction to the analysis of polycrystalline diffraction patterns. In the powder diffraction method, polycrystalline samples are used and assumed to have random orientation relative to the incident radiation. With enough randomly-oriented particles, the discrete Laue spots observed in single crystal diffraction patterns are replaced by smooth rings (Figure 9). Intensity in high quality powder diffraction patterns, therefore, only vary in one dimension (scattering angle) rather than two.

In 1912, Coolidge developed the first reliable X-ray generating technology, now dubbed the Coolidge tube, which provides the basis for all modern laboratory X-ray sources.[38] The tube produces X-rays by heating a thermionic cathode to produce a beam of electrons that strike a positively charged target anode. Characteristic X-rays are produced when the incident beam promotes a core-shell electron in the anode and a higher-shell electron falls into the hole left behind. The energy difference between the two shell levels is emitted as a photon. The energies of these X-rays are characteristic of the anode material and are tightly distributed, though commonly more than one type of relaxation event is induced, producing X-rays of more than one characteristic energy at a time. Bremsstrahlung X-ray radiation is produced when the electrons change direction under the influence of the positively charged anode. The energies are mostly a function of the accelerating voltage of the ionizing electrons and are broadly distributed. The total X-ray energy profile of a copper anode tube is provided as Figure 10.[39]

One of the limitations of the standard tube geometry is the heating of the anode by the incident beam. Rotating anode sources were developed to improve the cooling system and allow higher electron beam flux, in turn producing more brilliant X-ray radiation. This is the current state-of-the-art for laboratory X-ray sources.

Synchrotron radiation, first discovered in 1946 by researchers at General Electric, is an alternative X-ray generation technology.[40] In the synchrotron system, electrons are accelerated to relativistic speed by a linear accelerator. The electrons are injected into a magnetic tube that bends their trajectory. The acceleration of a charged particle by a magnetic field results in the emission of a photon. This produces a broad distribution of radiation, which can be passed through X-ray optical components to alter its characteristics (chromaticity, intensity, beam size). Advantages over laboratory sources include tunable wavelength, minimal divergence, linear

polarization, and extremely high brilliance. Figure 11 shows the brilliance of historical X-ray radiation sources.

Brilliance is the fundamental determinant of the signal-to-noise ratio in diffraction experiments and is given by:

$$Brilliance = \frac{photon\ flux}{(angular\ divergence)^2\ (energetic\ divergence)}$$

where photon flux is in units of $\frac{photons}{s-mm^2}$, angular divergence is in units of $mrad$, and energetic divergence is considered by limiting the photons counted to those within 0.1% of the central frequency of the radiation. The exceptional brilliance of synchrotron sources allows extremely sensitive analysis of phase composition, atomic positions, vibrational parameters, and even site occupancy factors.

Chromaticity and brilliance are the key differentiators in the analytical utility of diffraction data collected from synchrotron sources. Advanced X-ray optical components installed at the beamlines allow selection of a narrow band of radiation energies through diffracting, diverging and converging the X-ray beam. This removes the complexity of analysis associated with diffraction patterns collected from tube generator sources, which produce a broader spectrum of radiation wavelengths. The practicality of these components for standard laboratory machines is limited by their size and cost.

Thermal Expansion

Coefficients of thermal expansion (CTEs) describe dimensional changes in solids resulting from changes in their temperature. The coefficients can be positive (indicating an

increase in dimension with temperature), negative (indicating a contraction), or zero. The one-dimensional temperature-induced strain in a material, ε_L, is given by:

$$\varepsilon_L = \frac{\Delta L}{L_0} = \alpha \Delta T$$

where ΔL is the length change in the sample dimension, L_0 is the sample dimension at a reference temperature, α is the linear coefficient of thermal expansion, and ΔT is the temperature difference from some reference state. Rearranging the equation to solve for α gives

$$\alpha = \frac{1}{L_0}\frac{\Delta L}{\Delta T}$$

The linear CTE is commonly measured in two different ways.

In a dilatometer, a cylindrical or rectangular prismatic sample is suspended between two supports. One support is rigid and the other is a mobile pushrod, held in place by guiding frames and a weak spring. At the end of the pushrod opposite the sample is a displacement transducer. The sample chamber is surrounded by a furnace to heat the chamber. As the chamber changes temperature, the sample deforms and pushes against the pushrod, actuating the displacement transducer. (Figure 12).[41]

The other common method for measuring CTEs is by diffraction experiments. This is a much more detailed approach, because, in general, the thermal expansion of a material's unit cell may be unique in any direction, except where limited by symmetry. Thus, the description of crystallographic thermal expansion takes the form of a second-rank tensor:

$$d\varepsilon_{ij} = \begin{bmatrix} \alpha_{11} & \alpha_{12} & \alpha_{13} \\ \alpha_{21} & \alpha_{22} & \alpha_{23} \\ \alpha_{31} & \alpha_{32} & \alpha_{33} \end{bmatrix} dT$$

where $d\varepsilon_{ij}$ is the strain tensor associated with the differential temperature change dT and the α_{ij}'s are the thermal expansion coefficients in the principal crystallographic directions. Unit cell symmetry reduces the number of unique coefficients for a given material. The reduced CTE tensors for crystal systems investigated in this work are:

$$d\varepsilon_{ij,cubic} = \begin{bmatrix} \alpha_{11} & \alpha_{11} & \alpha_{11} \\ & \alpha_{11} & \alpha_{11} \\ symm. & & \alpha_{11} \end{bmatrix} dT$$

$$d\varepsilon_{ij,tetragonal} = \begin{bmatrix} \alpha_{11} & \alpha_{12} & \alpha_{13} \\ & \alpha_{11} & \alpha_{13} \\ symm. & & \alpha_{33} \end{bmatrix} dT$$

In three dimensions, the volume change associated with a change in temperature, ε_V, is given by:

$$\varepsilon_V = \frac{\Delta V}{V_0} = \beta \Delta T$$

where β is the volumetric coefficient of thermal expansion and ΔT is the temperature difference from some reference state. Solving this equation for β gives

$$\beta = \frac{1}{V_0}\frac{\Delta V}{\Delta T}$$

The most commonly reported CTE values from dilatometry experiments are for a polycrystalline sample with no preferred orientation. For such a sample, the linear CTE for the bulk material is an average of the unique coefficients of the CTE tensor:

$$\alpha = \frac{(\sum_{h=0}^{1}\sum_{k=0}^{1}\sum_{l=0}^{1}\alpha_{hkl})}{n_{hkl}} = \frac{\sum_{i=1}^{3}\sum_{j=1}^{3}\alpha_{ij}}{n_{ij}}$$

where α_{hkl} are the Miller indices of all of the crystallographic planes, α_{ij} are the coefficients of the second-rank thermal expansion tensor, and n_{hkl} and n_{ij} are the number of planes in the unit cell used in the summation and the number of linearly independent coefficients in the CTE tensor, respectively.

To compare the results between the two types of experiments, the relationship between α and β can be derived as follows: In a polycrystalline sample with no preferred orientation, volume change is isotropic. The instantaneous sample volume is:

$$V = L^3$$

Taking the logarithm:

$$\ln V = 3 \ln L$$

Differentiating both sides with respect to temperature:

$$\frac{1}{V}\frac{dV}{dT} = 3\frac{1}{L}\frac{dL}{dT}$$

Substituting the definitions of α and β from above, we find:

$$\beta = 3\alpha$$

This relationship can be used to easily compare results from dilatometric and crystallographic experiments.

Objectives and Approach

The systemic constraints of the EBC application require candidate materials to have highly refractory behavior with low silica activity. Current solutions are limited by their thermal expansion behavior. In this thesis, alkali aluminosilicate materials were synthesized,

characterized, and assessed as candidates for EBC materials on the basis of tailorable thermal expansion over a suitable temperature range.

In Chapter 2, the utility of the geopolymer crystallization processing method for synthesizing high-purity, single-phase crystalline alkali aluminosilicate materials was demonstrated. A systematic design of experiments was used to optimize the procedure for the purpose of synthesizing target compounds.

In Chapter 3, the thermal evolution of these materials systems was examined by *in situ* high temperature X-ray diffraction experiments performed at synchrotron beamlines. The mechanisms that drive the thermal expansion and phase transitions in these materials were studied with the goal of exploiting atomic mechanisms to engineer tailorable thermal expansion values.

The $K_xCs_{1-x}[AlSi_2O_6]$ system was then used as a prototype for mechanistic analysis in order to understand the influence of framework and bond dynamics on the thermal evolution of these materials. Building on that work, the analysis was extended to $Rb[AlSi_2O_6]$. This work provided a quantitative framework with which to understand the atomistic dynamics and phase transitions in these systems, and possibly other framework structures, and how chemical modification can be used to manipulate these features to control bulk properties, namely the thermal expansion behavior.

Chapter 4 presents a secondary body of work. It is the result of an investigation into the mechanical properties of basalt-reinforced geopolymer composites. These materials were developed as structural composites with high temperature resilience. All characterization was

done at room temperature. The results from previous chapters, therefore, will be critical to the extension of this work to *in situ* high temperature mechanical testing.

Chapter 5 suggests future directions for research based on the results obtained in the previous chapters and the context of the broader body of scientific literature.

Figures

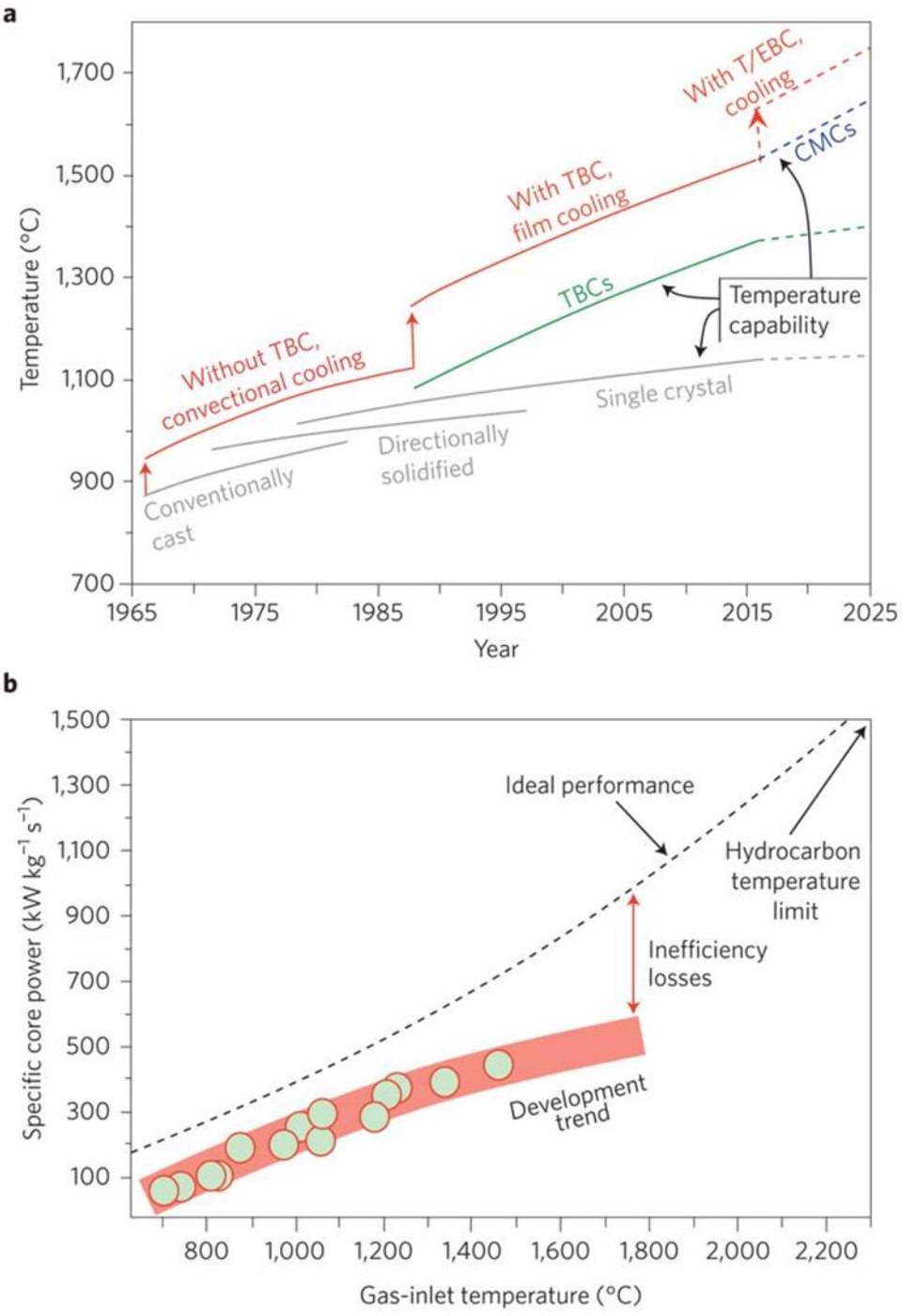

Figure 1 – Historical temperature and efficiency in turbine engines and improvements in coating technology.[2]

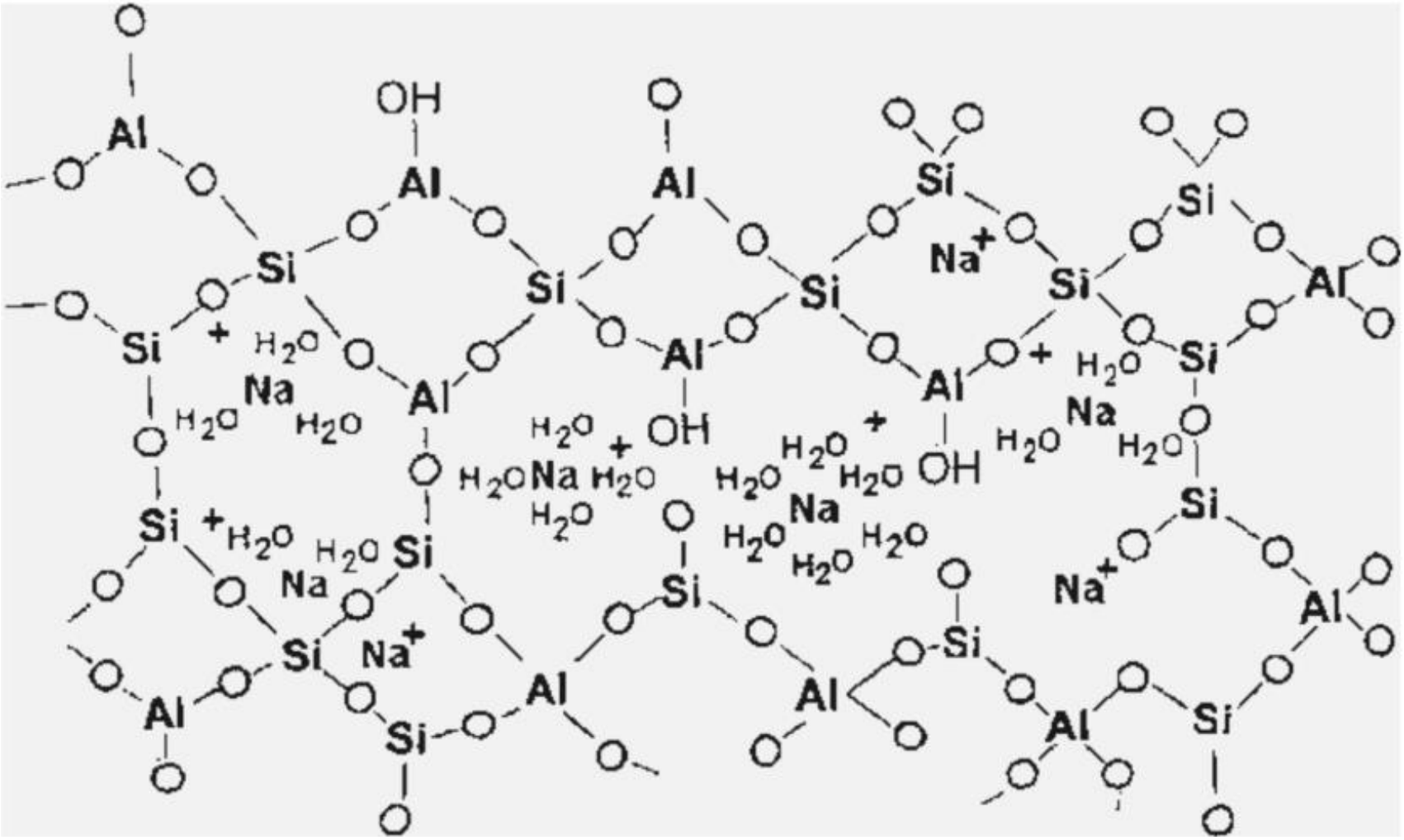
Al
OH
Si
Na+
H2O
Si
Al
Si
Al
Si
Al

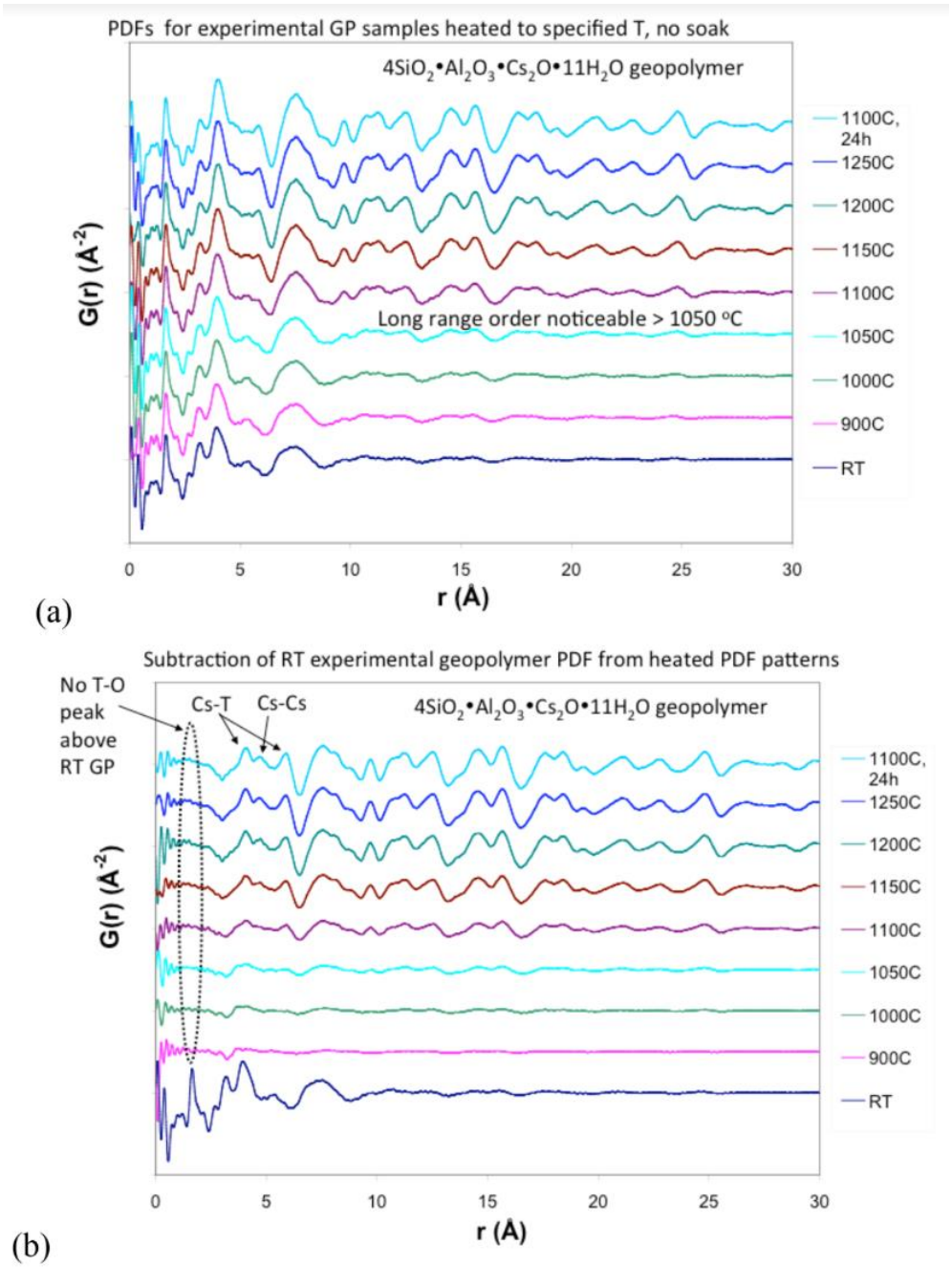

Figure 3 - In situ synchrotron measurements of cesium geopolymer powders (a) heated to 1100 showing that $[SiO_4]^{4-}$ and $[AlO_4]^{5-}$ tetrahedral units formed at ambient temperatures at less than 5 nm interatomic distances. The difference PDF plots in (b) confirmed that there were no differences between PDF plots at less than 3 nm in geopolymer before or after crystallization.

[20], [21]

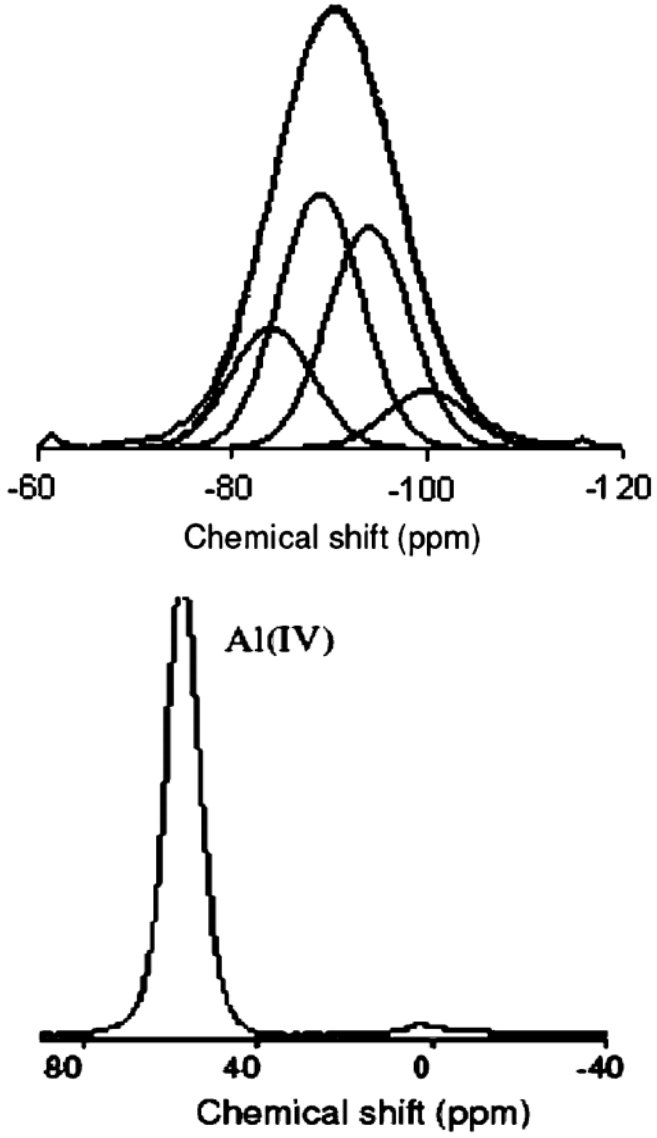

Figure 4 - ^{29}Si NMR (top) and ^{27}Al NMR (bottom) showing the distribution and connectivity of $[SiO_4]^{4-}$ and $[AlO_4]^{5-}$ tetrahedra units in the geopolymer phase. Multiple peaks in the fitted spectra of ^{29}Si NMR indicate the existence of Q^1-Q^4-bonded silicate species. Tetrahedra without full bonding are stabilized by alkali cations and water molecules.[27]

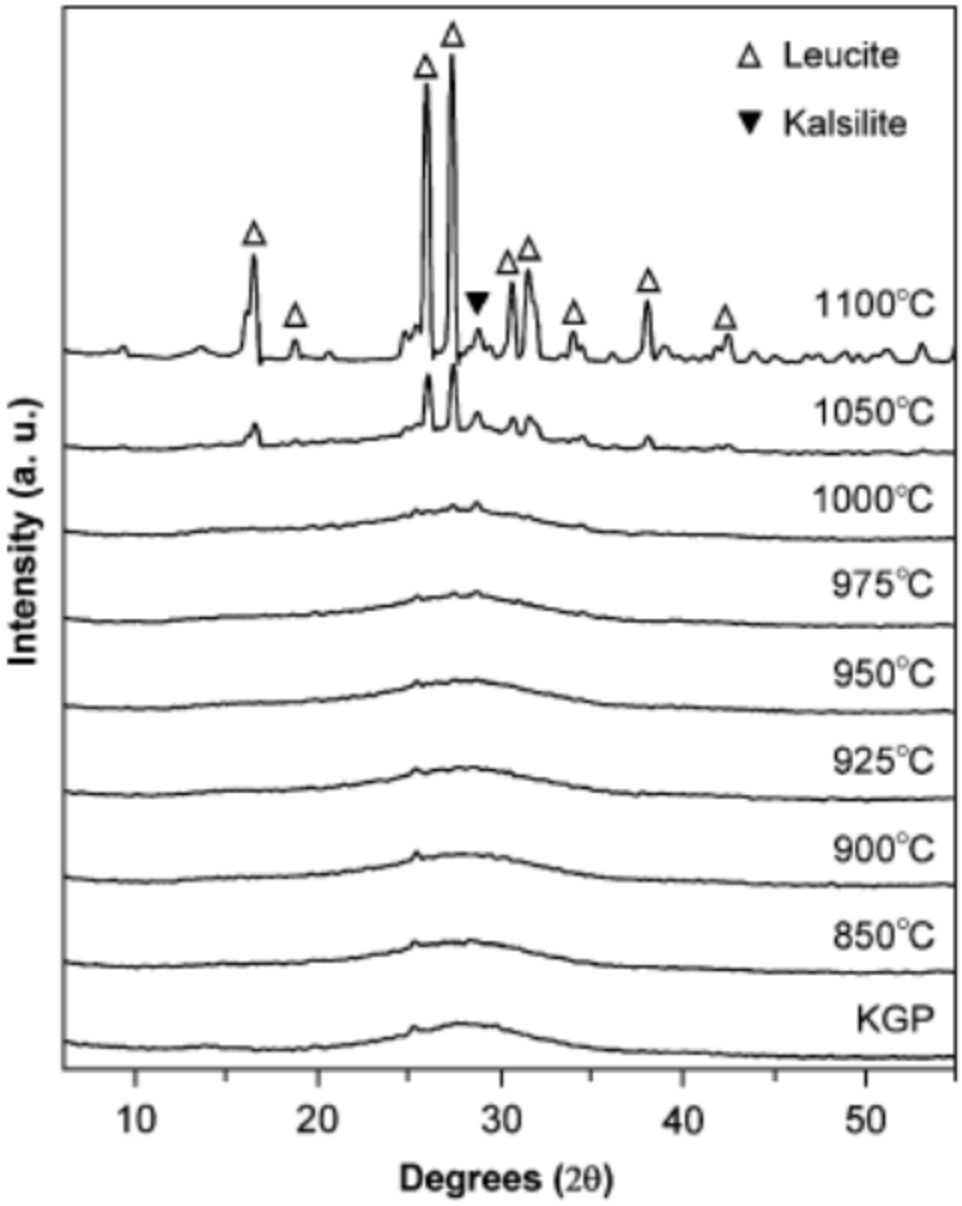

Figure 5 – X-ray diffractograms for unheated K-geopolymer, and after being heated to the specified temperature at 10°C/min heating and cooling rates, with no isothermal soak. After heating to ≥ 1000°C and cooling, KGP crystallized into tetragonal leucite ($K_2O{\cdot}Al_2O_3{\cdot}4SiO_2$) and a minor amount of kalsilite ($K_2O{\cdot}Al_2O_3{\cdot}2SiO_2$).[28]

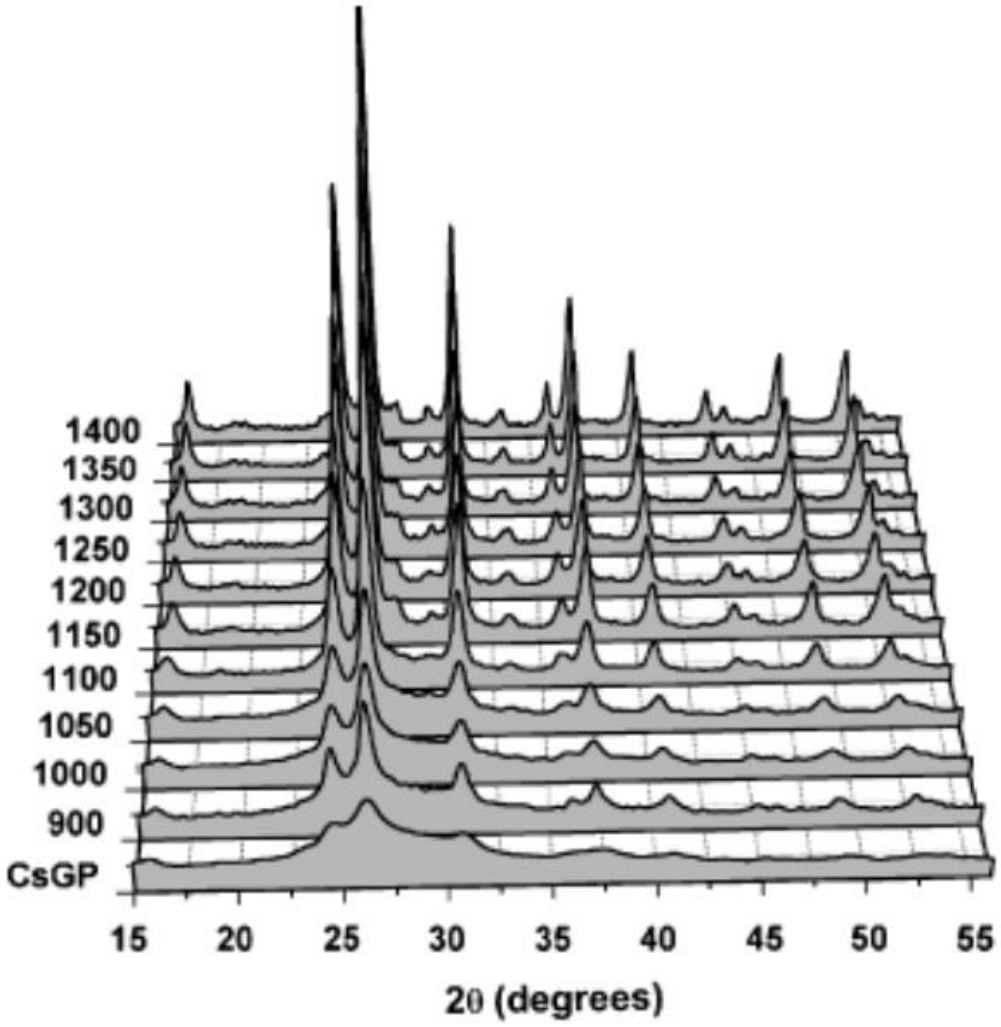

Figure 6 – X-ray diffractograms for Cs geopolymer, and after being heated to the specified temperatures (in °C) shown to the left at 10°C/min heating and cooling rates, with no soak.[29]

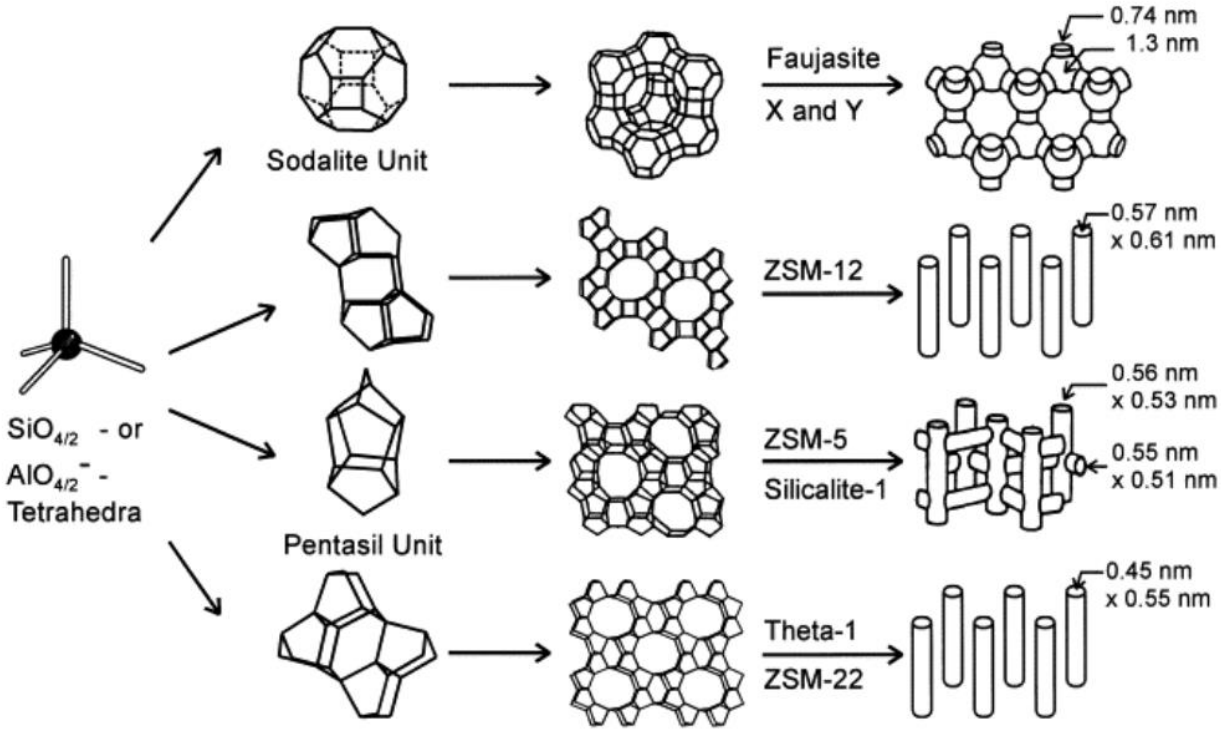

Figure 7 – The hierarchical development of framework structures. From left to right, the aluminate and silicate tetrahedral units, secondary units, framework structures, and pore geometry.[34]

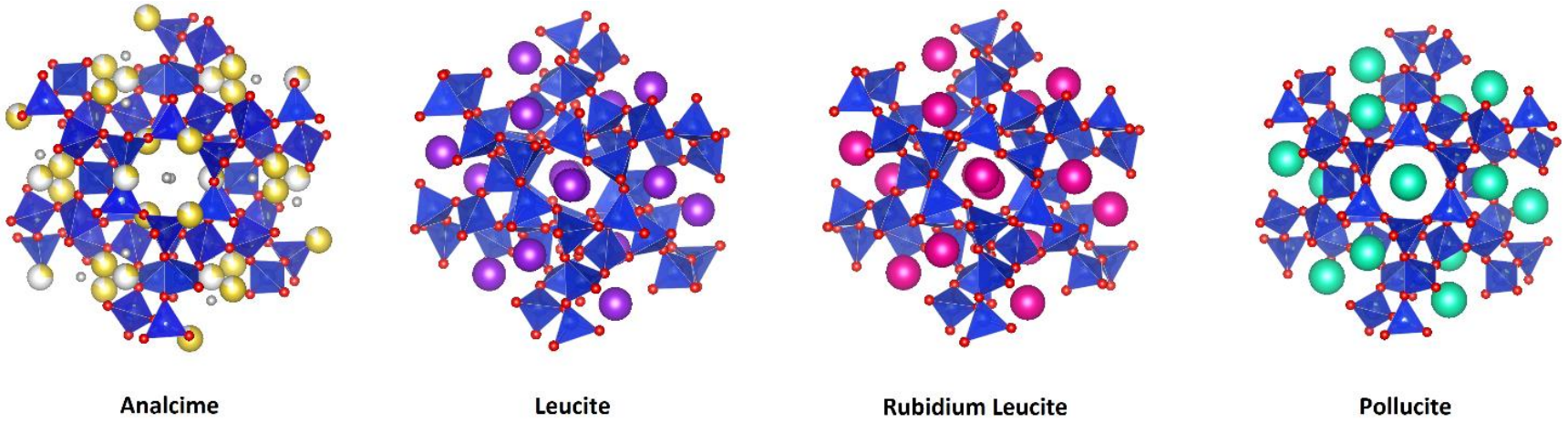

Figure 8 – The room temperature crystal structures of the analcime compositional family. The sodium-based structure, analcime, is hydrated, containing water in structural pore channels. The other structures host larger K, Rb, or Cs cations in the pore channels. The aluminosilicate framework flexes to accommodate the interstitial ions and molecules

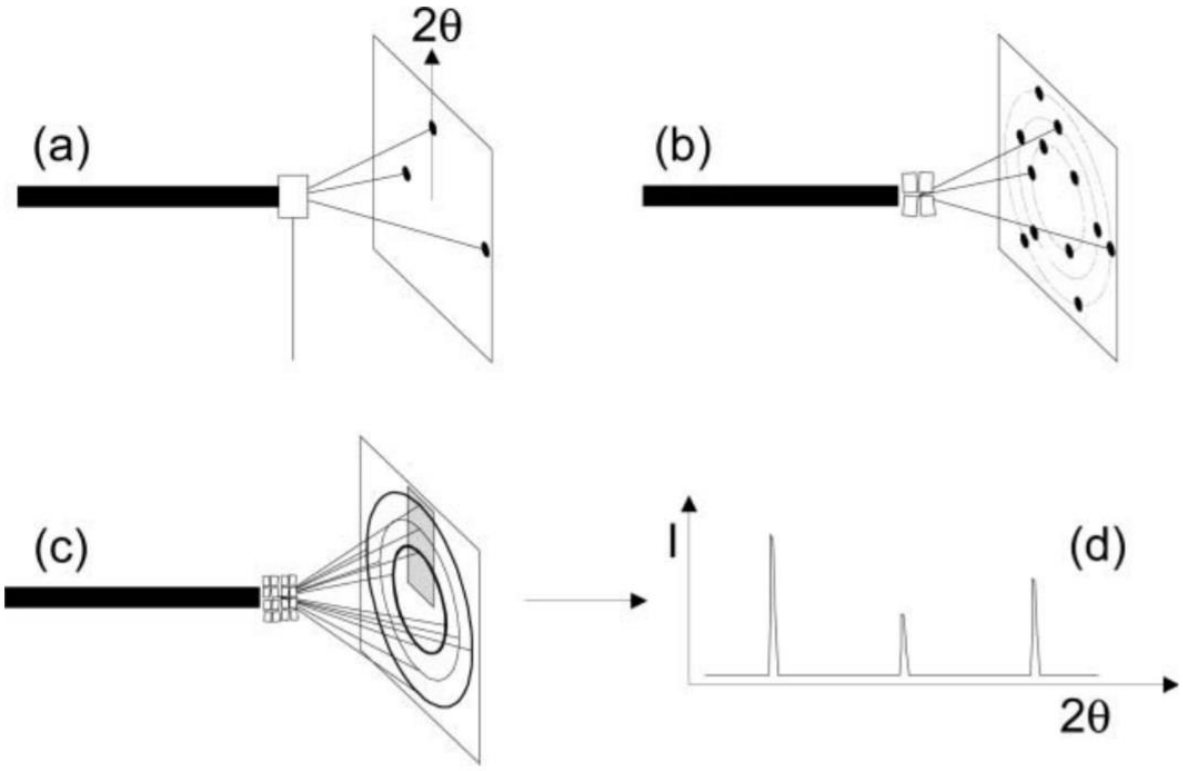

Figure 9 – (a) Diffraction from an oriented single crystal, (b) from a collection of four crystals at different orientations with respect to the incident beam and (c) from a polycrystalline material. One dimensional powder patterns (d) can be obtained by scanning a detector across the cones of diffracted intensity.[42]

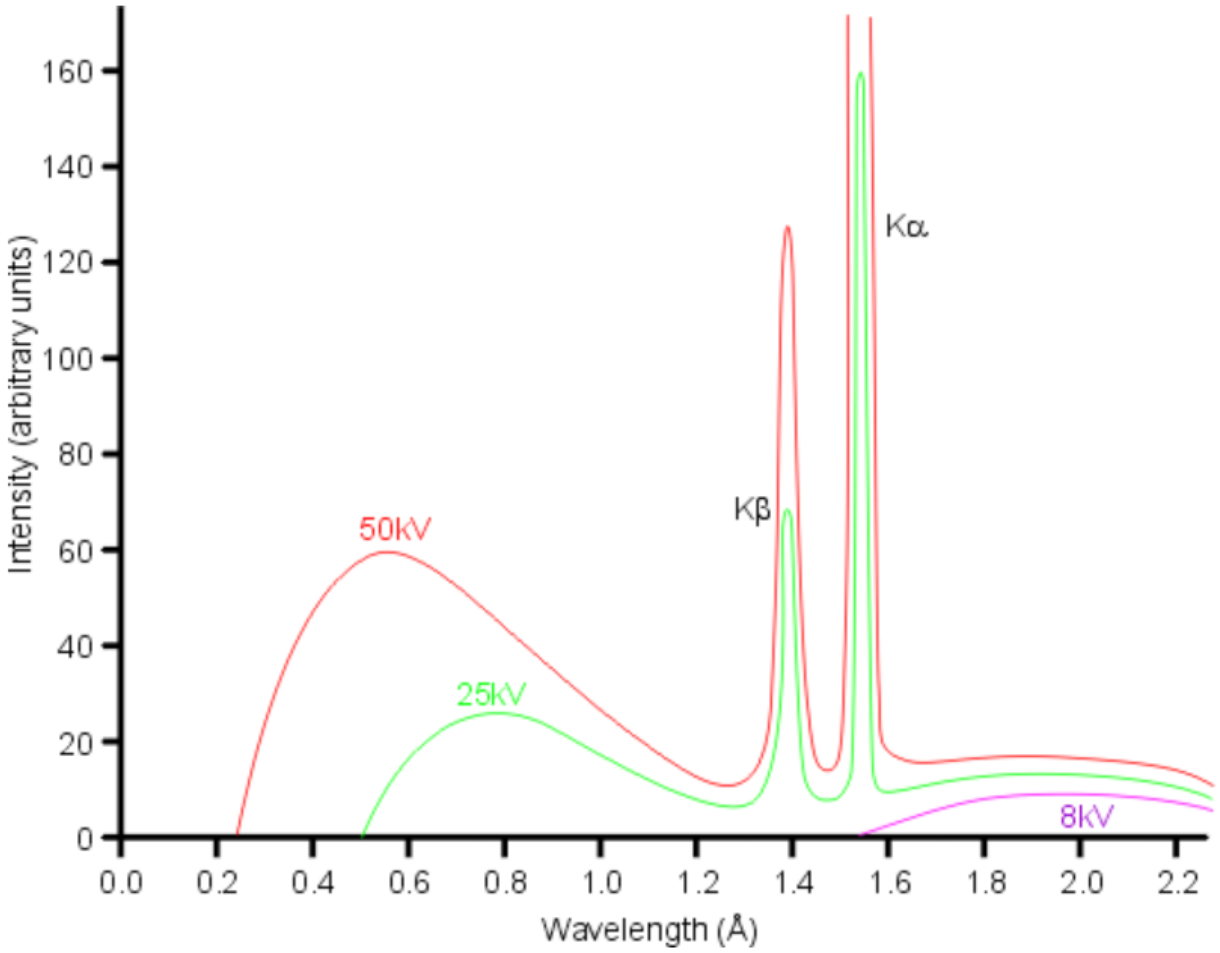

Figure 10 – The complete radiation profile for a copper X-ray source calculated for various voltages. The sharp peaks are "characteristic peaks" used for the interpretation of diffraction patterns. The broad, wavy background "Bremsstrahlung radiation" is an artifact of the radiation generation process. Note that the Kα ionizing potential for copper is approximately 8.04 keV, such that the 8kV accelerating voltage does not generate characteristic radiation.[39]

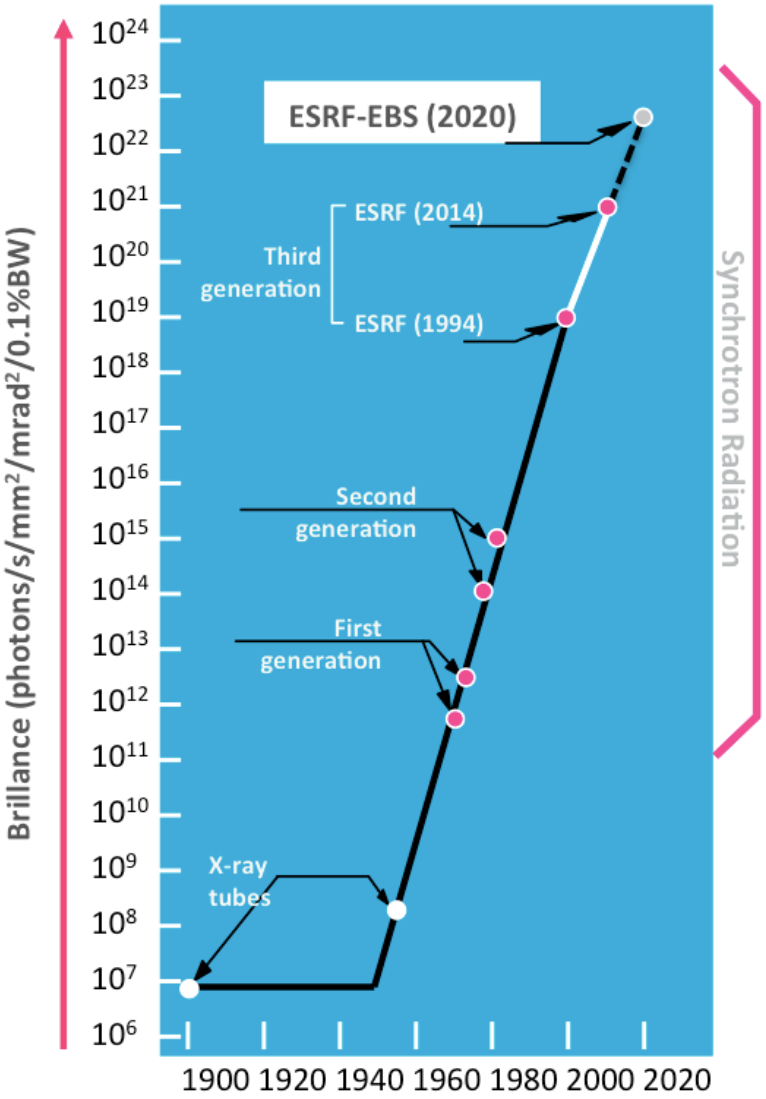

Figure 11 – Historical brilliance of X-ray sources.

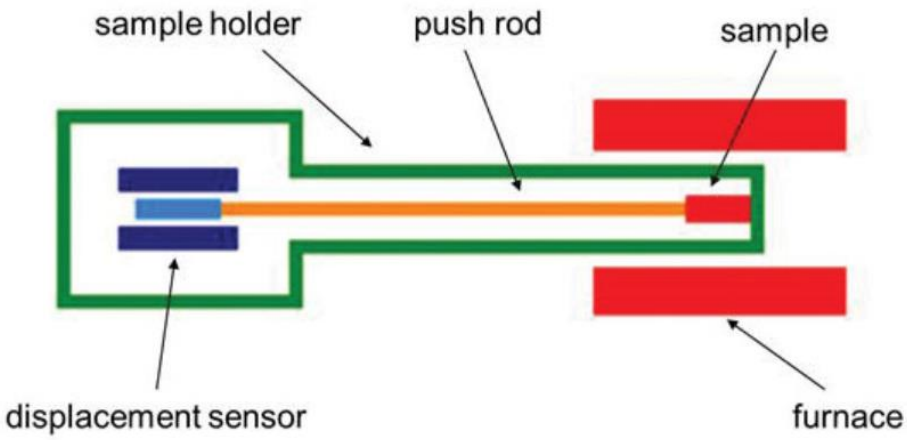

Figure 12 – Schematic of a horizontal dilatometer.[41]

CHAPTER 2 – EXPERIMENTAL METHODS

The synthetic method presented here reflects an effort to establish a facile synthesis to create high-purity, single-phase ceramics that can be translated easily into application. Rationale and commentary derived from the development of the synthesis is provided to assist in translational efforts, should any be made.

This method does not require specialty laboratory equipment beyond a high temperature furnace. Some of the steps could be avoided using commercial products as noted in Chapter 1, but current offerings do not allow enough control of stoichiometry to produce single-phase ceramics. Most of the steps are amenable to automation. Finally, the general steps for synthesis of many of the samples were the same. For conciseness, the details unique to individual materials are left for discussion in the corresponding subsequent chapters.

Geopolymer Crystallization Procedure

To produce high quality alkali silicate solutions, first, alkali hydroxide pellets (sodium hydroxide, 99% purity; potassium hydroxide, 99% purity; cesium hydroxide, 99% purity; Fisher Scientific, Hampton, NH) were dissolved in deionized water in a stainless-steel container in a water bath using low-speed stirring on a magnetic stir plate. The dissolution of alkali hydroxides is highly exothermic and concentrated solutions can attack borosilicate glass, with which most commercial laboratory glassware is made. The steel container helps to cool the solution more quickly while resisting chemical attack. It is important to cool the solution as much as possible before the next step due to the temperature sensitivity of silicate polymerization.[43]

After cooling the alkali hydroxide solution to room temperature, silica fume (Cab-O-Sil EH5; Cabot Corp., Tuscola, IL) was dissolved in the alkali hydroxide solution using low-speed stirring on a magnetic stir plate. This step must be performed slowly because, like the last step, it

is highly exothermic and can interfere with the desired morphology of the silica in solution. After complete dissolution and cooling, the solutions were stored in a refrigerator at 4 ℃ for at least 24 hours prior to use in the next step to allow equilibration of the silicate units. For mixed-cation systems, the appropriate alkali silicate solutions were mixed in proportion to the desired stoichiometry under low-speed stirring on a magnetic plate for 24 hours and then allowed to cool again in a refrigerator before proceeding.

To form the geopolymer gel, metakaolin powder (MetaMax Al_2O_3:$2SiO_2$; BASF, Ludwigshafen, Germany) was added to the alkali silicate solution using an overhead mixer (Model no.: RW 20; IKA, Staufen, Germany) equipped with a high shear mixing blade for 10 minutes, followed by 5 minutes of mixing at 1800 rpm in a planetary mixer (model no.: ARE-250; Thinky, Tokyo, Japan). Because of the tightly controlled chemistry of this system and the prevalence of unreacted metakaolin in geopolymers, high-shear mixing was used to slough away geopolymer gel from the surface of metakaolin particles to prevent passivation and to physically decompose the particles.[12], [23] Other researchers have found success with resonant acoustic mixing (RAM)**.** [30] Other mixing technologies can be validated by analyzing unreacted metakaolin content in the solid geopolymer before crystallization.

To ensure a dense solid geopolymer was formed, the gel was degassed in a planetary mixer. Degassing minimizes the air content in the gel using centrifugation. This reduced the number and size of pores in which gases and water can become trapped. We did not rigorously study the effect of degassing on the formation of crystalline phases, but the presence of porosity should be expected to influence densification mechanisms.

To allow the geopolymer gel to set, the gels were poured into Delrin plastic, disc-shaped molds 2-inches in diameter by ¼-inch in depth. The molds were sealed and stored in low-

temperature curing ovens at 50 ℃ for 24 hours. Curing conditions were kept the same for all samples because it has been shown that curing conditions can affect the crystalline product.[15]

After curing, the solid geopolymer was heat treated to convert to the crystalline phase. Samples were exposed to the maximum temperature for 1 hour using 5 ℃/minute heating and cooling rates. The optimum crystallization temperature varies with the alkali cation and the framework stoichiometry. For example, sodium-based geopolymers of the $Na_2O{\cdot}Al_2O_3{\cdot}2SiO_2{\cdot}11H_2O$ chemistry will crystallize at as low as 800 ℃, potassium-based geopolymers of the $K_2O{\cdot}Al_2O_3{\cdot}4SiO_2{\cdot}11H_2O$ chemistry will crystallize at approximately 1000 ℃, and cesium geopolymers of the $Cs_2O{\cdot}Al_2O_3{\cdot}4SiO_2{\cdot}11H_2O$ chemistry require heating above 1100 ℃ to crystallize. After crystallization, pellets were ground into powders using a mortar and pestle.

Phase Identification

Because usage time at the synchrotron facilities is awarded by a competitive, proposal-based system, we made extensive efforts to characterize our samples at the Frederick Seitz Materials Research Laboratory prior to performing diffraction experiments at the synchrotron beamline. Preliminary room temperature X-ray diffraction data was collected with a Siemens D5000 diffractometer (Bruker AXS Inc., Madison, WI) equipped with a copper anode (Cu-Kα, λ=1.5418 Å, 40 kV, 30 mA). Samples were placed in a plastic powder sample holder and leveled. Typical scans covered the range of 5-65° 2-theta in 0.01° intervals with 1 second of exposure time at each scan location.

These scans were used to verify crystalline phase formation and perform phase identification. Phase identification was performed using the Search/Match algorithm in MDI Jade 9 (Materials Data Inc., Livermore, CA) to search against the PDF-4+ database (ICDD v.

2018, International Center for Diffraction Data, Newton Square, PA). This was the principal tool used to refine the processing variables in with the geopolymer crystallization synthesis. Once a single-phase material of the same composition as the bulk was obtained, the sample was prepared for testing at the synchrotron.

Sample Preparation for *in situ* High Temperature Synchrotron Diffraction

The setup employed in this work for use at the synchrotron facility has been highly customized by the Kriven group and thus necessitated specific sample preparation. Samples were prepared for synchrotron diffraction experiments by first sieving with a standard 325-mesh (45 μm) sieve. Annealed platinum powder (99.99% purity; Sigma-Aldrich, St Louis, MO) was added to approximately 10 weight percent to act as an internal temperature standard.[29] The cubic platinum phase was stable up to its melting point of approximately 1768 °C and did not react with the sample powders. The diffraction behavior of a platinum standard, characterized by the National Institute for Standards and Technology, allowed measurement of the experimental temperature to an accuracy of approximately 5 ℃.[44] Mixing platinum powder into the sample had the added benefit of enhancing the homogeneous heat distribution in the sample powders.

The combined sample and platinum powders were packed into capillary tubes (Figure 13). Quartz capillary tubes were used for samples whose melting point was below approximately 1200 ℃, which included most of the sodium-based samples and some of the potassium-based samples. Single-crystal sapphire capillary tubes were used for the rest. Sapphire allows measurement over a larger range of temperature before softening, but often contributed diffraction peaks to the patterns that could obscure sample peaks.

The capillary tubes were plugged with alumina tubes on each end with very small internal diameters (>45 μm) to prevent the sample powders from falling out, but to allow a free flow of air into the experimental chamber. This is an important detail of the experimental setup because access to air reduces the potential for oxygen vacancies to form relative to experiments in vacuum which are required by many high temperature setups. Oxygen vacancies can alter the lattice parameters of the material, can be difficult to detect by X-ray diffraction, and, furthermore, a vacuum environment does not reflect the operating environment of most of these materials in high temperature applications.

The plug tubes were secured with zirconia paste (American Elements, Los Angeles, CA). The plug-and-capillary assembly was then mounted into a larger-diameter alumina tube to provide structural support (Figures 13-15), and again secured with zirconia paste. Platinum paste was added to frame the capillary "window". This addition absorbed and re-radiated heat into the capillary window, allowing for even higher sample temperatures to be achieved.

Experimental Setup at APS Beamline 33 BM-C

The Advanced Photon Source (APS) is a synchrotron radiation source that was first commissioned in 1995. It is located on the campus of Argonne National Laboratory in Lemont, IL. The facility currently hosts 35 sectors with 84 total beamlines. Sectors are typically divided by technical specialty, e.g. life sciences, macromolecular crystallography, magnetic materials, etc. In July of 2019, Argonne National Laboratory received approval from the Department of Energy for an $815M upgrade that is expected to increase the brightness of the X-ray source by 100-1000x over the present facility, which is already one of the most advanced in the world. An image of the APS facility and a detailed map is included as Figure 16.

Our powder diffraction experiments were performed at the 33 BM-C beamline of the Advanced Photon Source at Argonne National Lab in Lemon, IL. 33BM-C is equipped with a double Si monochromator and a single focusing mirror.

Sample assemblies were mounted in a 3-axis goniometer to allow for precise alignment with the X-ray beam in the center of a Huber four-circle diffractometer. The goniometer was mounted on a rotating stage that was set to approximately 1 revolution per second. Rotating the loosely packed powders this way allowed them to tumble and prevented crystallographic texturing from affecting the measurements.

Once the sample was aligned, a quadrupole lamp furnace was mounted in place surrounding the sample and centered on the X-ray beam. Diffraction patterns were collected with a Pilatus 100k plate detector located approximately 1100 mm away from the center of the diffractometer. At this distance, the detector collected data over a range of approximately 3° 2-theta in a single image and complete scans were taken at 1° 2-theta intervals sweeping the range from 5-35° 2-theta. The beam was focused to a square cross-section of 0.5 mm x 0.5 mm on to the sample and the beam energy was approximately 21.5 keV (λ=0.577 Å).

Diffraction patterns were collected with the samples in transmission (Debye-Scherrer) geometry (Figure 17).[45] The main advantage of the transmission geometry over reflection (Bragg-Brentano) geometry is the reduction of error in the measurement of diffraction peak positions due to sample displacement, which are particularly troublesome at high temperatures due to challenges with the integral heating equipment.[46] The quadrupole lamp furnace does not rely on heating elements integrated into the structural support of the sample and therefore removes the error associated with this method of heating.

The main disadvantage of transmission geometry is incomplete transmission of the X-ray beam by the samples due to absorption. A significant photon flux reduction is observed in transmission since photons must pass completely through the sample to be recorded by the detector, rather than scattering from a small depth below the surface as in reflection geometry. Absorption is given by

$$Absorption = 1 - \frac{I}{I_0} = 1 - e^{-\left[\left(\frac{\mu}{\rho}\right)x\right]} [47]$$

where $\frac{I}{I_0}$ is the ratio of the intensities of the diffracted to beam to the incident beam, $\left(\frac{\mu}{\rho}\right)$ is the mass attenuation coefficient (calculated or determined experimentally), and $x = \rho t$ is the mass thickness (ρ is the sample density and t is the sample thickness).

Absorption is additive for compounds, so, especially for heavy-atomic mass species, it is important to have small (thin) samples. This can be problematic for the large number of particles required for the statistical assumptions underlying the powder diffraction method, but the wavelength tunability and high intensity of the synchrotron source still allowed collection of high-quality diffraction patterns.

Interaction with the beamline hardware is done using the open source Experimental Physics and Industrial Control System (EPICS) software toolset, which was developed and supported at Argonne National Laboratory. The EPICS software allows precise control and error monitoring over nearly all hardware upstream of the diffractometer at 33 BM-C. In this work, we typically employed control over the beam shutter, 2-theta motor arm, and beam shutters to collect diffraction data.

Quadrupole Lamp Furnace (QLF)

The use of thermal imaging furnaces to collect in situ diffraction patterns dates to the work of Stecura in 1968.[48] Their setup used a carbon arc furnace as a light source with mirrors to focus the light onto the sample to heat it. The maximum reported temperature for this setup was over 2800°C, but unreliable temperature control limited the functional maximum to approximately 1700°C.

In 1976, Watanabe proposed a design that operated on a principle similar to float zone systems used to synthesize single crystals.[49] In their scheme, a sample was placed at the coincident focal points of two parabolic halogen lamps coated with a layer of gold in order to increase the reflection and focusing efficiency of light onto the sample. The sample enclosure incorporates small slits through which the incident and diffracted X-ray radiation can pass without interference. Sample temperatures up to 1700°C were reported using this system.

In 1993, Schneider proposed a compact furnace that used two commercially available halogen IR-reflector lamps to the sample. Sample temperatures up to 1500°C were reported.[50] In 2005, Kriven presented a modification to Schneider's design that utilized four lamps, increasing the sample heating capacity to 2000°C.[51], [52] The design allowed for scans to be conducted with samples in open air with only limited obstruction of the beam by entry and exit slits. This new design was the quadrupole lamp furnace (QLF).

The QLF heating system consists of four IR halogen lamps (Xenophot HLX64635, 15V, 150W; OSRAM, Munich, Germany) connected in series. According to the manufacturer's specifications, the radiation profile of the bulbs extended from 500-2500 mm with maximum intensity at approximately 800 nm. The reflecting surfaces of the bulbs were coated with gold to enhance IR reflectivity. The lamps were arranged at right angles to align the real images of the

lamp filaments to converge to a disk-shaped hot zone approximately 4 mm in diameter and 4 mm in width approximately 19 mm away from the edge of the reflector in free space. The QLF frame included integral water jackets for forced convective cooling of the bulbs. A recirculating water chiller was used to provide a continuous flow of cold water to the jacket system.

For temperature control, the QLF had a screw clamp and positioning mechanism for a thermocouple. Type B or R thermocouples placed in the hot zone (but not in contact with the sample) were used to provide live temperature readings for feedback control. A proportional-integral-derivative (PID) controller was used to control power input and to monitor the temperature of the furnace. The hot zone was characterized with a B-type thermocouple (Figure 18) and showed a temperature deviation of less than 20 °C.[52] In situ high temperature X-ray diffraction patterns of standardized materials (MgO, CeO_2, and Pt) were collected to validate the setup and were found to be in good agreement with previous literature (Figure 19).[53]

In our work, thermocouple readings were found to deviate from the sample temperature, as measured from the refinement of platinum unit cell lattice parameters against diffraction peaks, by up to 150 °C at high temperatures. The combination of the low temperature threshold for signal generation for B-type thermocouples and the observed measurement deviation due to displacement of the thermocouple from the sample in space make low-temperature control challenging. Thus, for reporting, the temperature measurement determined by the platinum refinement method was preferred for its intrinsic accuracy and its physical proximity to the sample. One may also note a comparative lack of data between approximately 30-300 °C. This can be attributed again to the characteristics of the control system.

Wiring of the control equipment was routed through radiation-protected labyrinths that allowed electrical connections between hardware inside and outside of the experimental hutch.

The PID controller was thus driven directly and independently of the beamline software. There are opportunities for integrating these controls, but the frequency of software and hardware changes at the beamline complicated efforts to this effect.

Operating Procedure for *in situ* High Temperature Diffraction Experiments

A typical visit to the beamline began with consultation with the beamline scientist to coordinate the beam profile (energy, beam size, etc.) followed by beam characterization. Characterization is done by collecting a diffraction pattern from a standard reference material (SRM), in our case lanthanum hexaboride (LaB_6).[54] The SRM diffraction procedure was used to determine the precise wavelength of the beam as well as Gaussian and Lorentzian contributions to peak shape from the beam and hardware to diffraction profiles. The LaB_6 sample was provided by the beamline scientist at 33BM-C and was housed in a glass capillary that did not contribute to the diffraction profile.

Each sample was first scanned in a glass or fused silica capillary at room temperature to determine appropriate parameters for the diffraction experiments (scan range, scan step size, and exposure time). The scan range varied with the beam energy and was limited by the outlet slit of the QLF but offered far superior resolution to a laboratory diffractometer despite this limitation. A typical scan collected from approximately 0-6.4 $Å^{-1}$ scattering vectors (0-35 °2-theta at approximately 21.5 keV beam energy).

Once scan parameters were determined, the temperature setpoint was raised to the next step. The first step was determined by the output threshold of the QLF and was commonly around 300 °C. Subsequent scans were taken at temperature setpoint intervals of 100 °C until an upper limit of 1500 °C setpoint or until the crystalline peaks of the sample began to decrease in intensity, an indication of melting, whichever came first. After the final high temperature scan,

the temperature setpoint was reduced stepwise back down to room temperature and a final scan was collected.

Intensity data were integrated from the image files produced by the Pilatus detector using a custom Python script written by beamline scientists at 33BM-C. Raw images, integrated diffraction profiles, and log files were taken for record and analysis.

The synthesis, testing, and analysis of these samples is, by necessity, an iterative process. The final reported structures, thermal expansions, and phase transition behavior reported in the following chapters are products of multiple beamline visits. Often, samples that appear to contain a single phase on a laboratory diffractometer will exhibit multiple phases when confronted with the increased brilliance of the synchrotron source. Proper phase transition characterization is nearly impossible to do in a single trip.

Structural Refinements Using Crystallographic Data

Most of the crystal structures studied in this work were previously solved. In the language of crystallography, this means that the space groups (the mathematical descriptors of crystal symmetry), the lattice parameters (the edge dimensions of the unit cell), and the rough positions of atoms were established by researchers who came before us. Some of the structures we describe were solved about 80 years ago. However, the availability of higher quality crystallographic data and the advances in computer technology since have allowed us to dive deeper into the details of these structures than was possible before and, we hope to demonstrate, to great reward. Additionally, the ability to collect diffraction patterns *in situ* at high temperature represents a substantial advance over quenched samples, which often exhibit metastable phases.

In the late 1960s, Rietveld described an automated least-squares minimization procedure for structural refinement using neutron powder diffraction data.[55], [56] By the late 1970s, the methods were adopted for X-ray powder diffraction data.[57], [58]

Diffraction peaks arise due to constructive interference of radiation diffracted through a crystal. The angle through which the radiation is scattered is a function of the distance between the atomic planes from which it was scattered and the wavelength of the incident radiation:

$$\lambda = 2d_{hkl} \sin\theta$$

where λ is the wavelength of the incident radiation, d_{hkl} is the distance between the hkl atomic planes ($h, k,$ and l are miller indices), and θ is the scattering angle. The values of d_{hkl} depend on the size and shape of the unit cell and thus the position of the peaks in the diffraction profile are a result of the average atomic distances in the crystal.

The absolute intensity of the peaks on a profile depend upon several experimental conditions and sample parameters and do not have a direct physical meaning. The relative intensity of peaks for a given sample, however, are a function of the identity of the atoms in the crystal and the geometry of the diffracting planes. Mathematically, the intensity of a peak is described by

$$I = SML|F|^2PAE$$

where S is a scale factor for the relative contribution of individual phases, M is the multiplicity of the peak, L is the Lorentzian polarization factor, F is the structure factor, P is the preferred orientation factor, A is the absorption coefficient, and E is the extinction correction.

Most of these are constant for the entire profile and some vary with the scattering angle only. The structure factor, however, varies with location in crystal. Mathematically, it is defined as:

$$F_{hkl} = \sum_{j=1}^{m} N_j f_j e^{[2\pi i(hx_j + ky_j + lz_j)]}$$

where F_{hkl} is the structure factor for the hkl planes, N_j is the fraction of equivalent positions occupied by atom j, f_j is the atomic scattering factor for atom j (describes how the incident radiation interacts with the electrons of an atom), and x_j, y_j, and z_j are the fractional coordinates of atom j. Atomic scattering factors are tabulated for different energies of incident radiation and can be easily calculated.

By solving both Bragg's law and the structure factors for a crystal structure, the diffraction profile of a crystal can be calculated. The concept proposed by Rietveld was to refine theoretical structures by adjusting the structures to manipulate their calculated diffraction profile to more closely match experimental diffraction data. Computational methods allowed straightforward automation of the minimization of differences between the experimental and theoretical patterns.

From the equations above, it is evident that the effect of crystal symmetry and atomic distances have the most significant effect on the appearance of the diffraction profile. Historically, these were the first data extracted from diffraction experiments and reported for a new material. The effect of atomic positions, however, is much more subtle, appearing in the exponential term of the structure factor with each having a value from 0 to 0.999… Thus, the ability to refine these terms, along with other weaker drivers of the intensity, such as temperature

factors and site occupancies, with great accuracy rely upon the availability of higher purity samples, advanced X-ray optics, and radiation sources of higher brilliance.

Software packages are available to automate the iterative steps of a crystallographic refinement. In this work, we utilized the open source GSAS II package developed at Argonne National Laboratory.[59] The refined structures were visualized and analyzed using the free-to-download VESTA package developed at the National Museum of Nature and Science in Japan.[60]

Figures

Figure 13 – Details of the experimental setup at the APS synchrotron facility. (Top) a powder sample loaded into a quartz capillary and secured inside an alumina tube. (Bottom) A sample rod mounted into an adapter for a goniometer.

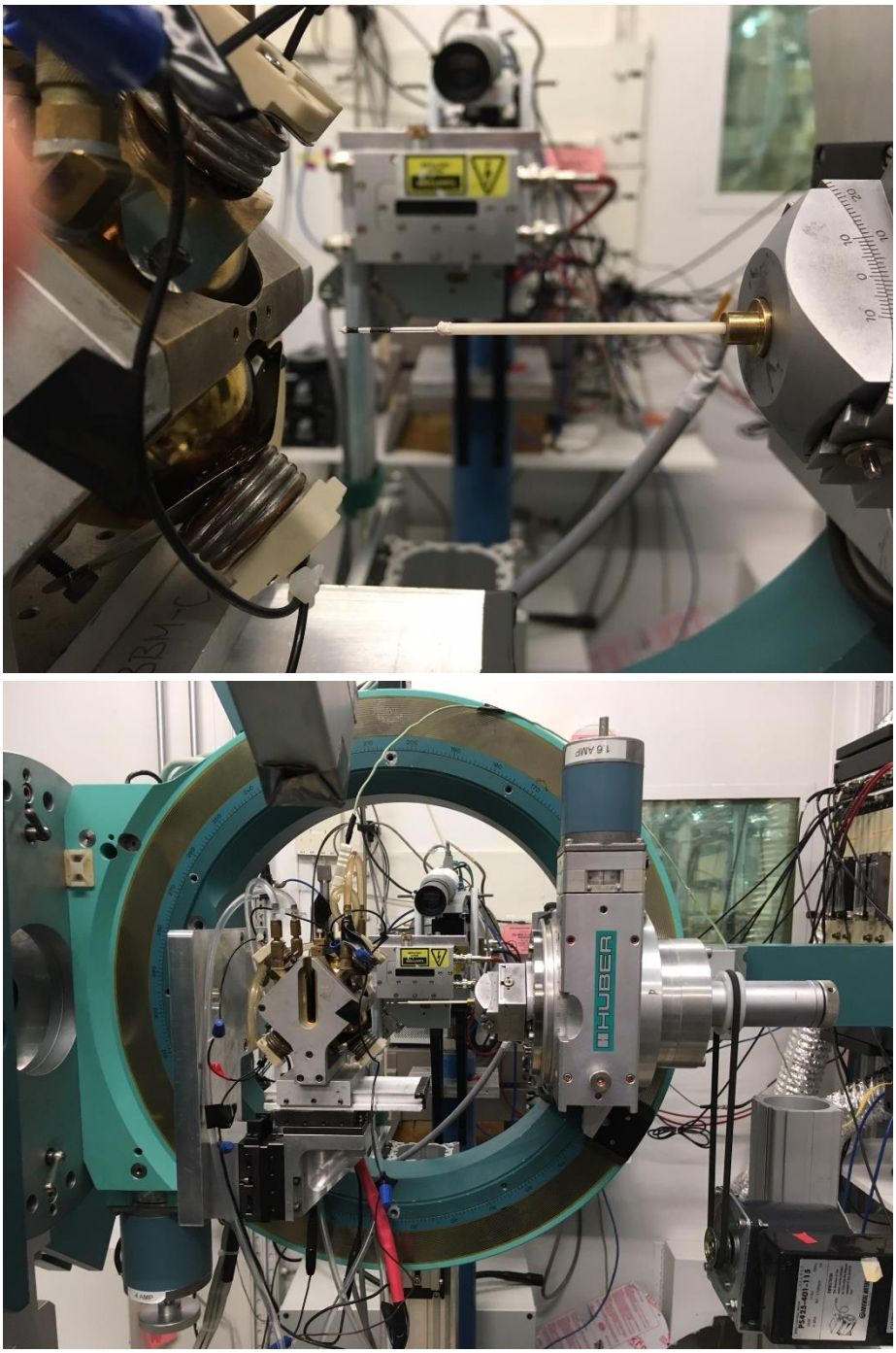

Figure 14 – Details of the experimental setup at the APS synchrotron facility. (Top) A close-up image of the sample in place at the beamline. (Bottom) A zoomed out view of the sample in place at the beamline.

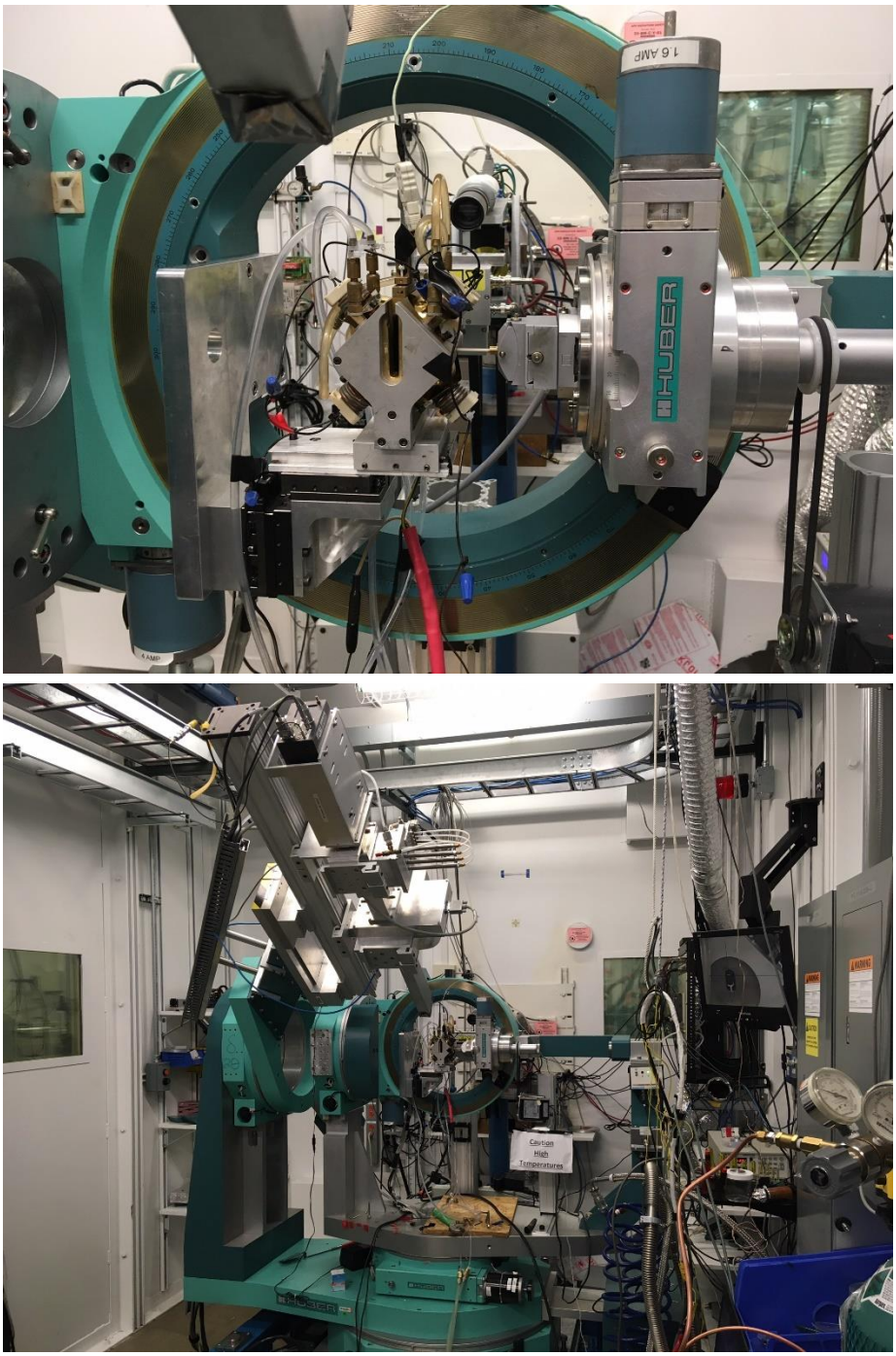

Figure 15 – Details of the experimental setup at the APS synchrotron facility. (Top) The QLF slid into place surrounding the sample and in the beam path inside the diffractometer. (Bottom) A full view of the diffractometer, sample setup with furnace, and the detector.

Figure 16 – (Top) An aerial image of the Advanced Photon Source at Argonne National Laboratory. (Bottom) A schematic view of the facility with associated research area details.

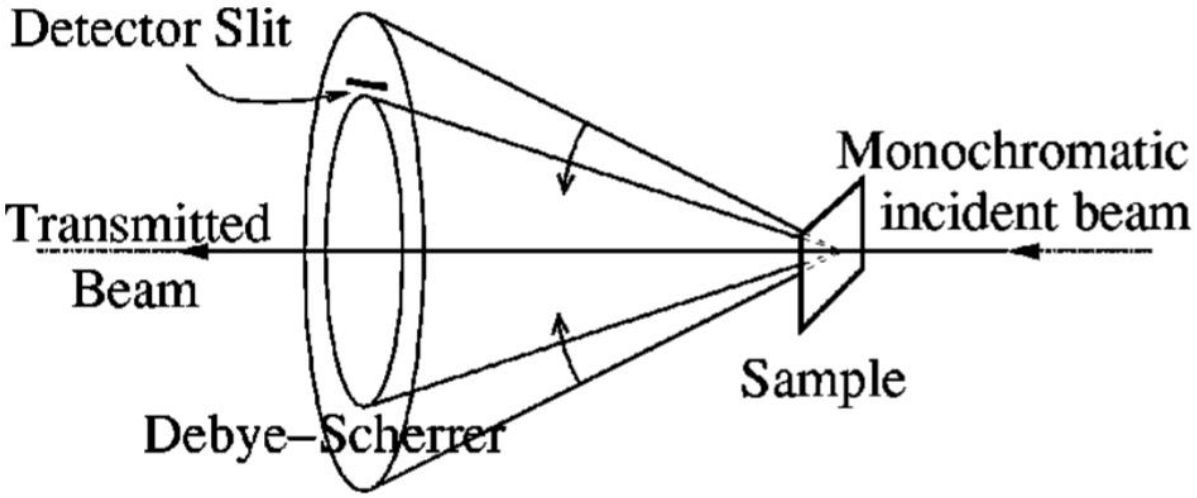

Figure 17 – Schematic of Debye-Scherrer diffraction geometry used for synchrotron diffraction experiments.[45]

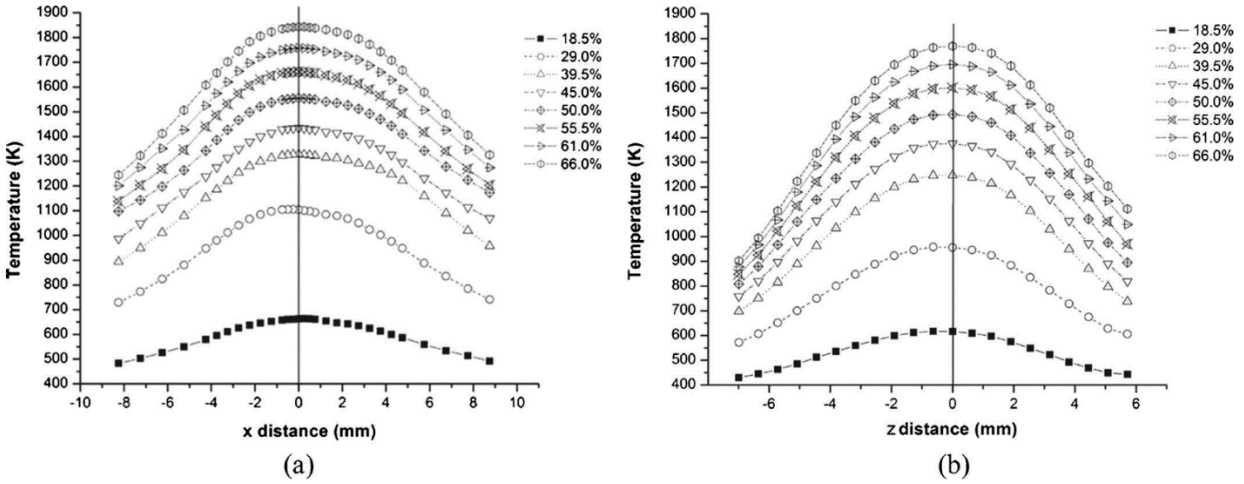

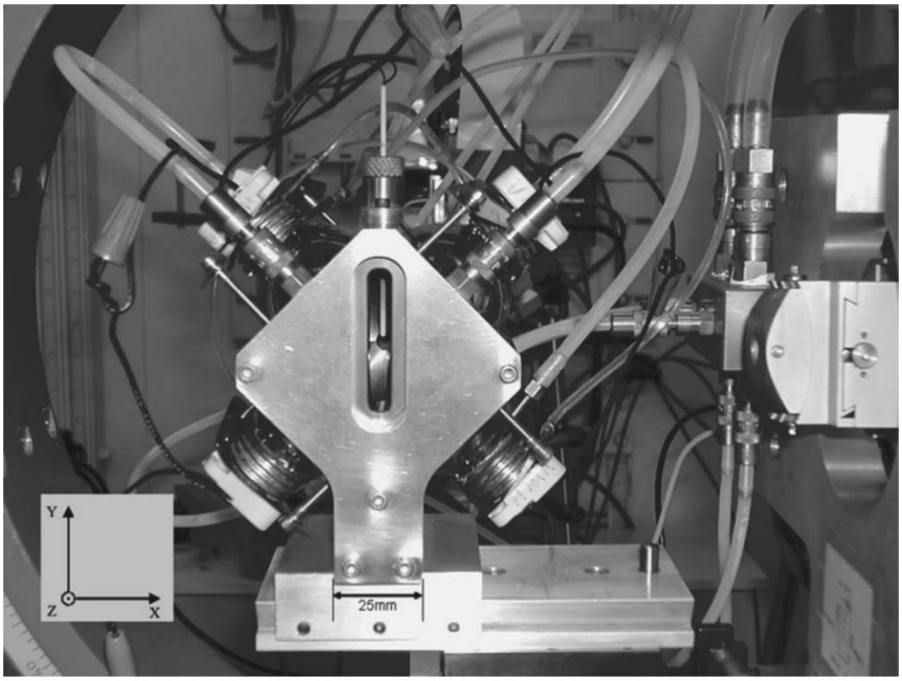

Figure 18 – (Top) The effect of power and distance from the furnace center on temperature distribution along (a) the X axis and (b) the Y axis of the furnace, as measured with a Pt30%Rh–Pt6%Rh (type B) thermocouple for the axis system shown in the second image (bottom).[52]

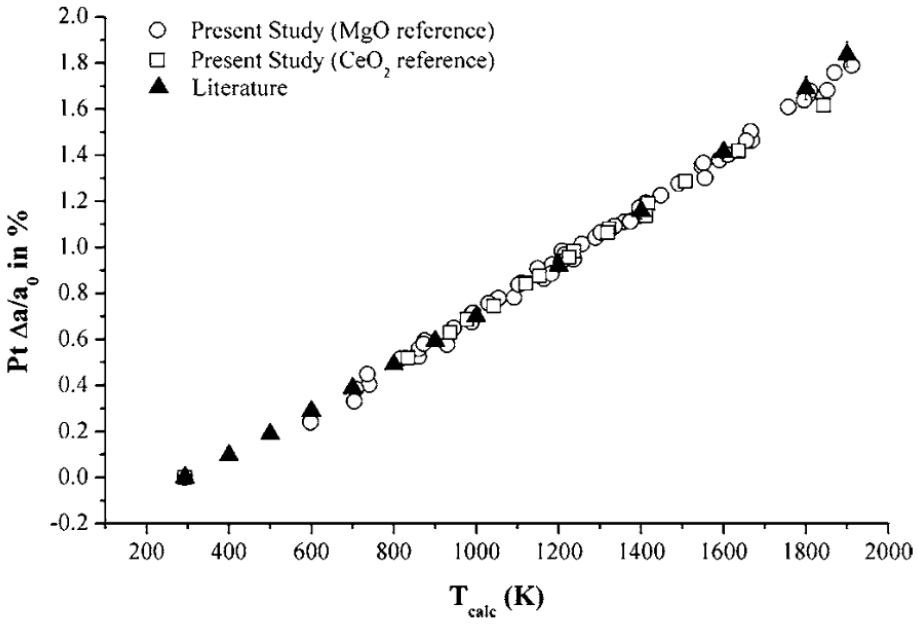

Figure 19 – Comparison of the thermal expansion of Pt measured using MgO and CeO2 as reference materials with literature. Note: The error bars are smaller than the size of the symbol.[52], [53]

CHAPTER 3 – THERMAL EXPANSION AND PHASE TRANSITIONS IN THE 1:1:4 ALKALI ALUMINOSILICATES

Materials of the tectosilicate classification can be differentiated by the ratio of the constituent elements or molecular groups. Classically, the inorganic chemist's representation embodies the former and the ceramist's the latter. For example, in the chemist's notation, the mineral anorthite would be represented as $Ca[Al_2Si_2O_8]$, where the brackets denote the ionic coordination between the Ca^{2+} cation and the aluminosilicate framework with the bulk composition $[Al_2Si_2O_8]^{2-}$. For the same compound, the ceramist would write $Ca_2O{\cdot}Al_2O_3{\cdot}2SiO_2$ to convey the ratios of standard oxide compounds. The ceramist's notation also facilitates a shorthand constructed from the identity of the interframework cation and the coefficients of the oxide compounds. Anorthite thus becomes "Calcium 1:1:2 aluminosilicate". The notations are equivalent and used in conjunction or interchangeably depending upon which best suits the discussion.

In this chapter, mixed-cation alkali aluminosilicates are investigated with the motivation of attaining tailorable thermal expansion values. The goal of this approach is to synthesize a single-phase material with the approximately equivalent thermal expansion to SiC_f/SiC CMCs.

Crystallography of the Leucites

The first family of materials studied here were the crystalline materials of the formula $M[AlSi_2O_6]$, $M_2O{\cdot}Al_2O_3{\cdot}4SiO_2$ where M = alkali cation, or "1:1:4 alkali aluminosilicates". They belong to the "analcime", also called "analcite", mineral family, named for the sodium-containing mineral, $Na[AlSi_2O_6]$. The analcime family also includes leucite, $K[AlSi_2O_6]$, and pollucite, $Cs[AlSi_2O_6]$. We will also treat the rubidium analogue of these materials, $Rb[AlSi_2O_6]$, though it has not been discovered as a naturally occurring material and thus is not a proper

member of the analcime family. This group of materials have low silica activity and are highly refractory, with melting points approaching 2000 ℃, making them potential candidates for EBC applications (Figure 20).[61], [62]

Crystallographic studies of the analcime family date back to the 1930s. A series of communications and publications from W. H. Taylor, W. L. Bragg, and G. Náray-Szabó detail the discovery of the nature of the tetrahedral aluminate and silicate frameworks and interstitial cations and determination of unit cell parameters of analcime.[35], [63]–[66] The structure of the high temperature, high symmetry cubic leucite ($K[AlSi_2O_6]$) phase was solved by single crystal methods by Peacor in 1968.[67] The solution of the structures of several of the analcime family members of tetragonal symmetry by powder diffraction methods was first reported by Mazzi in the 1970s.[68], [69]

The analcime family shares a common framework structure.[63]–[66], [70] Viewing projections down <111>-type directions (Figure 21), rings formed by six tetrahedra are aligned to form hollow channels, called “pore channels”, which alkali cations or water molecules can occupy, called “W-sites”, named for the water molecules present in these sites in the analcime crystal.

The sodium-containing species for which the analcime family is named has a starkly different arrangement of alkali cations than the rest. Sodium ions are too small to occupy W-sites and instead occupy “S-sites”, named for the sodium ions present in these sites in the analcime crystal, which are octahedral holes in the framework structure (Figure 21). Hirao suggested that the rubidium and cesium structures be referred to as leucites instead, referring to their similarity to the potassium structure with regards to the position of the alkali cations.[71] We adopted this nomenclature for the rubidium 1:1:4 aluminosilicate.

The conformation of the framework in this material family is directly related to the crystal symmetry. In appropriate conditions, i.e. temperature and pressure, the unit cells of analcime, leucite, rubidium-leucite, and pollucite exhibit tetragonal crystal symmetry, having space group $I4_1/a$. With increasing temperature, pressure, and/or average cation size, a displacive solid-solid phase transition occurs to cubic symmetry, having space group Ia3d.[70], [72]. There is a superficial similarity between the transitions that arise from changes in the different thermodynamic parameters, but ultimately the details of how the framework compensates for thermal (temperature-induced) and physical (pressure- or composition-induced) stresses are different.[73]–[77] This study is concerned with the changes observed when varying composition and temperature.

Considering the analcime structure as the "ground state" framework conformation, the pore channels can be used as an indicator of the state of the framework. In these pore channels, ions and molecules coordinate with oxygen atoms and distort bonds in the framework. The distortions can include deformation of the individual tetrahedra, by changing the angle of O-T-O bonds or the length of T-O bonds, where T=Al/Si, or of the framework conformation, by changing the angle of T-O-T bonds or the length of T-O bonds. The degree of this distortion depends upon the identity of the species occupying the channel.[73], [74]

The largest cation, cesium, causes the most severe distortion relative to analcime.[66] Room temperature cesium-leucite (pollucite), $Cs[AlSi_2O_6]$, has highly symmetric T-O-T bond angles around the channel. The ring geometry is close to a regular hexagon (small, out-of-plane distortions of the hexagon exist due to the highly interconnected nature of the framework) and the crystal symmetry is cubic. The medium-sized cations, rubidium and potassium, cause moderate distortion to the framework channel.[69], [71] At room temperature, there is a high

degree of variance in the T-O-T bond angles around the channel and pronounced out-of-plane distortion of the pore rings. The ring geometry is a distorted hexagon and the crystal symmetry is tetragonal. As mentioned above, the smallest Group 1 cation, sodium, occupies octahedral interstitial sites in the framework rather than the pore channel.[68], [78] At room temperature, water molecules occupy the channel sites and have very little influence on the T-O-T bond angles around the channel. Severe out-of-plane distortions are present.

The temperature-induced phase transition is expressed with slight modifications in leucite, rubidium-leucite, and pollucite. In leucite, this transition has been reported as occurring in both natural and synthetic samples across the temperature range from 400-750°C.[30], [31], [71], [72], [79]–[82] The exact temperature range over which the transition takes place depends upon the synthetic method used to produce the material or, in the case of natural samples, which were the subject of the bulk of the literature on the analcime family, the location from which the material was procured, due to impurities present in the sample. Before the transition, the unit cell expands along the *a* and *b* principal axes and contracts along the *c* axis. The transition is thought to involve the rotation of the tetrahedra, such that the basal oxygens in the six-membered rings are more closely aligned along the (111) planes, and the coherent movement of consecutive rings away from each other.

The $I4_1/a \rightarrow Ia3d$ structural transition has been reported in rubidium leucite over the temperature range from 350-400°C.[31], [71] We are not aware of any reports of naturally-formed rubidium leucite.

Pollucite has an even lower transition temperature. The structure is usually reported as having cubic symmetry at room temperature, i.e. the $I4_1/a \rightarrow Ia3d$ transition is complete before approximately 30°C, but one report puts the transition temperature as high as 115 °C.[31]

The significant variation in the reported properties for these materials provides additional motivation for the current work since, while full advantage was taken of previous literature to understand the general behavior of the leucites, unique details due to the novelty of the geopolymer crystallization processing route have emerged. Characterizing these details are of prime importance to the practical application of these materials.

Sample Preparation

All samples for these experiments followed the geopolymer crystallization procedure described in Chapter 2. From the literature, it was known that leucite and pollucite crystallize from the geopolymer phase at approximately 1100℃ and 1200℃, respectively.[28], [29], [83] To avoid the influence of difference processing conditions on structural differences in the samples, $K_xCs_{1-x}[AlSi_2O_6]$ and $Rb[AlSi_2O_6]$ samples were heat treated at a maximum temperature of 1200℃ for 1 hour with cooling and heating rates of 5℃/minute. During experimentation, we discovered that samples from the $Na_xK_{1-x}[AlSi_2O_6]$ system would melt to produce an amorphous glassy phase. The solution was to adjust the heat treatment to a maximum temperature of no higher than 900℃ with cooling and heating rates of 5℃/minute.

Analytical Methods

While many researchers have addressed different aspects of the phase transitions in the leucites, there has not been a systematic study of the atomic mechanisms which drive the associated change in crystal symmetry. To rigorously determine the mechanisms responsible for the changes in the structures, we evaluated several geometric parameters describing relative atomic and rigid unit motions and distortions. Some were modified from descriptions of clay structures to better describe the geometry of the leucite framework. [84], [85] Tetrahedral

flattening, τ, describes the deformation of framework tetrahedra with respect to the basal oxygen plane of the six-membered rings:

$$\tau = \left[\sum_{i=1}^{3} (O_{apical} - T - O_{basal})_i\right]/3$$

This description was modified from the more typical tetrahedral distortion parameter, which is directionless. We defined apical oxygen atoms as alternating above and below the basal planes of the rings since this is the ring geometry of the cubic leucite family of structures (Figure 22).

Basal oxygen plane corrugation, ΔD, is defined as the range of displacement of basal oxygen atoms from the ideal plane and quantifies the "twist" of the tetrahedra with respect to the basal plane:

$$\Delta D = D_{max} - D_{min}$$

$$D = \frac{ax + by + cz + d}{\sqrt{a^2 + b^2 + c^2}}$$

where D is the perpendicular distance from the center of an oxygen atom to the plane of best fit through the basal oxygen atoms; a, b, c, and d are the coefficients of the parametric equation of the basal oxygen plane; and x, y, and z are the coordinates of the oxygen atoms. Planes were found with the plane fitting function in VESTA. Miller indices of the planes and fractional coordinates of the atoms were converted to Cartesian coordinates for the calculation of D values in absolute distance.

W-W spacing is defined as the distance between neighboring alkali cations on W sites in the pore channels (Figure 22).

Tetrahedral rotation, α, is defined as the average internal angle of the hexagonal pore structure:

$$\alpha = \left[\sum_{i=1}^{6}(\varphi_i)\right] \Big/ 6$$

where φ_i's are the internal angles of the pore rings (Figure 23).

Several classical parameters were also analyzed in VESTA – average T-O bond length, bond length distortion index, quadratic elongation, and bond angle variance – to describe distortions of aluminate/silicate tetrahedra.[86]

Average T-O bond length, D_{T-O}, was calculated for each unique tetrahedral site and combined using a weighted average. For example, in tetragonal leucite with n unique tetrahedral Al/Si centers:

$$D_{T-O}^{i} = \left[\sum_{m=1}^{4}(T-O)_m\right] \Big/ 4$$

$$D_{T-O} = \left[\sum_{i=1}^{n}\left(h^i D_{T-O}^{i}\right)\right] \Big/ \left[\sum_{i=1}^{n}\left(h^i\right)\right]$$

where $(T-O)_m$ are the lengths of the individual Al/Si-O bond and the weighting functions h^i are equal to the multiplicity of the i-th tetrahedral center site in the unit cell.

The bond length distortion index, DI_{T-O}, defines the average deviation of T-O bond lengths from the mean value.[87] This was calculated as:

$$DI_{T-O}^{i} = \left[\sum_{m=1}^{4}\left|(T-O)^m - D_{T-O}\right|\right] \Big/ D_{T-O}$$

$$DI_{T-O} = \left[\sum_{i=1}^{n}\left(h^i DI_{T-O}^i\right)\right] \Big/ \left[\sum_{i=1}^{n}\left(h^i\right)\right]$$

where $(T-O)^m$ and D_{T-O} have the same meaning as above and the weighting function h^i is again the site symmetry of the i-th tetrahedral center.

Quadratic elongation, $\langle\lambda\rangle$, describes the variance of polyhedral angles.[88] It was calculated as:

$$\langle\lambda\rangle^i = \left[\sum_{i=1}^{n}(l_i - l_0)^2\right] / n$$

$$\langle\lambda\rangle = \left[\sum_{i=1}^{n}\left(h^i\langle\lambda\rangle^i\right)\right] \Big/ \left[\sum_{i=1}^{n}\left(h^i\right)\right]$$

where l_i are equivalent to $(T-O)_m$ bond lengths, l_0 is the center-to-vertex distance of a regular polyhedron of the same number of sides and volume, n is the coordination number of the central atom of the polyhedron, and the weighting function h^i is the site symmetry of the i-th tetrahedral center. A regular polyhedron has quadratic elongation of 1. Distorted polyhedra have values greater than 1.

The bond angle variance describes the variance of bond angles.

$$\sigma_i^2 = \left[\sum_{m=1}^{n}(\theta_m - \theta_0)^2\right] / (n-1)$$

$$\sigma^2 = \left[\sum_{i=1}^{n}(h_i\sigma_i^2)\right] \Big/ \left[\sum_{i=1}^{n}(h_i)\right]$$

where θ_i are the O-T-O bond angles, θ_0 is the bond angle for a regular polyhedron of the same number of sides and the weighting function h_i is the site symmetry of the i-th tetrahedral center.

Results

$K_xCs_{1-x}[AlSi_2O_6]$ System

Phase Transition Behavior

Phase transition behavior varied strongly with alkali cation stoichiometry. In $K[AlSi_2O_6]$, we observed the coexistence of the tetragonal and cubic phases between 479°C and 637°C (Figure 24). As temperature increased, the relative amount of tetragonal leucite decreased and that of cubic leucite increased. This range was defined as the temperature domain of the transition and is within the typical reported range for pure leucite.

For $K_{0.8}Cs_{0.2}[AlSi_2O_6]$, the temperature domain was dramatically different. Both phases were detected at room temperature and the tetragonal phase was completely transformed by 430°C. Tetragonal leucite was present in the room temperature scans of $K_{0.6}Cs_{0.4}[AlSi_2O_6]$ and $K_{0.4}Cs_{0.6}[AlSi_2O_6]$, but was completely transformed by the second temperature interval, 358°C and 232°C, respectively. It is important to note that temperature resolution at low temperatures is a limitation of the QLF since it employs a single thermocouple for feedback control of temperature. Therefore, it is possible that the transformation in these two samples was complete at a temperature below what our experiments detected. The phase transition temperature domain was suppressed to below room temperature in samples with greater than 60 mole percent cesium content.

Structural evolution of tetragonal phases

Because the end members are isostructural, it was assumed that the leucite-pollucite pseudo-binary phase space has a large solid solubility range in which potassium and cesium occupy the same site in proportion to the composition. Coordination with the interframework cation is known to influence the framework structure. Thus, the pore channels aligned along <111>-type directions shifted from a collapsed state to an expanded state with increasing temperature and cation size. Coordinating oxygen anions from the framework structure are more closely packed near the smaller potassium cation compared to the cesium cation in the same position. The attainment of the fully expanded state of the framework is thought to mark the completion of the phase transition. Our mechanistic study uncovered details that add nuance to this understanding.

We calculated the correlation of the unit cell volumes of each phase with the deformation parameters we evaluated. Plots of each were inspected for nonlinear relationships, but none were observed. In the following sections, we discuss the distortions with the highest correlation with unit cell volume detected in each material. Table 1 shows the correlation of each mechanism with unit cell volume for each composition tested. Table 2 gives calculated CTE values for the principal directions of each phase at various temperatures. Empirical unit cell, atomic, and distortion mechanism parameters are presented in Tables 8 – 22 in the Appendix.

In the structural framework of leucite, there are two unique rings along the <111>-oriented pore channels and a third that is equivalent to the first by symmetry of the unit cell (Figure 25). Because of the relative orientation of the two unique rings in the cell, independent distortion parameters can be correlated with the unique lattice constants of the tetragonal phase (Figure 26).

In tetragonal $K[AlSi_2O_6]$, the tetrahedral rotation distortions of the individual rings have high correlations; 0.9844 and -0.9938 for ring types 1 and 2, respectively; with the lattice constants up to the transition temperature. Above the transition temperature, the two ring types become symmetrically equivalent and the rotation angle remains approximately constant. The relationship observed here is not coincidental. An appropriate structural motif should necessarily reflect the symmetry of the unit cell.

A strong negative correlation, -0.9503, was observed between T-O bond lengths and unit cell volume (Figure 27). T-O bond contraction occurs in framework aluminosilicates due to out-of-plane vibrations of oxygen atoms, known as “bond swinging”.[86] Here the “planes” refer to those defined by the three nuclei locations of the atoms involved in T-O-T bond chains. It is theoretically possible to measure the severity of out-of-plane oxygen vibrations by refining anisotropic displacement parameters for oxygen atoms in the structure. However, oxygen has a very small X-ray scattering cross section, resulting in a small structure factor and a limited contribution to the diffraction pattern from oxygen atoms. Because of this, refinement of anisotropic displacement parameters did not yield significantly better fits in our work and in some cases led to unstable refinements and so were excluded from this analysis.

We also observed strong correlations of bond angle variance in tetrahedral units and tetrahedral flattening in the type-2 six-membered ring with increasing unit cell volume. The strong negative correlation of bond angle variance with the unit cell volume, -0.9656, indicates that the tetrahedra are becoming closer to ideal, developing a more symmetric geometry of the electron density distribution around the metal centers. The correlation of tetrahedral flattening in the type-2 rings with unit cell volume, 0.8244, indicates site-specific distortion of the framework tetrahedra. The correlation of tetrahedral flattening in the type-1 rings with unit cell volume is -

0.0864. As mentioned above, the opposing mathematical sign of this distortion for the two ring types is a result of the symmetry of the unit cell and reflects a good choice of the structural motif.

For tetragonal $K_{0.8}Cs_{0.2}[AlSi_2O_6]$, only a few data points were collected before the phase transition due to the low temperature range over which this transition occurs and the limitations of the QLF noted above, so we refrained from drawing statistical conclusions from this data.

Structural evolution of cubic phases

In c-$K[AlSi_2O_6]$, W-W spacing within the pore channels is highly correlated with unit cell volume (Figure 28). This is interpreted as an increase in W-O coordination bond lengths and results in the expansion of the pore channels perpendicular to the rings. Concomitant with W-W spacing, T-O bond lengths also show strong positive correlation with unit cell volume (Figure 29). The result is a coordinated expansion of unit cell without reorientation of the tetrahedra. The attainment of the fully expanded state of the framework during the phase transition marks the completion of tetrahedral rotation. Thus, the only mechanism by which the unit cell can expand is by elongating coordination bonds.

Samples with mixed alkali cation content exhibited increasing W-W distance and T-O bond lengths as the dominant mechanisms. Here, the framework attained a fully expanded state in the cubic phase and rigid body distortions of tetrahedra did not contribute to unit cell volume expansion. This result holds with increasing cesium concentration.

The correlations of the tetrahedral distortion index and quadratic elongation with unit cell volume monotonically approach zero with increasing cesium content (increasing average interframework cation size) for mixed-cation samples with cubic unit cell symmetry. This

suggests that the distortions of the framework tetrahedra depend upon the identity of the interframework cation in a different manner than they depend upon temperature.

In $Cs[AlSi_2O_6]$, we observed trends in W-W spacing (Figure 30) and tetrahedral rotation (Figure 31). The correlation of W-W spacing and tetrahedral rotation were 1.000 and -0.9135, respectively. Though the correlation of tetrahedral rotation is high, the uncertainty was close to the order of the change observed throughout the temperature region. Thus, although a strong trend was detected, we refrained from drawing conclusions based on this data. No other mechanisms displayed a significant correlation with unit cell volume in the pollucite sample. Thus, we identified the primary feature that gave rise to this behavior as the expansion of the framework around the interframework cesium atoms.

Thermal Expansion

In this section, the relationship between the dominant distortion mechanisms and thermal expansion is discussed, followed by a comparison with the thermal expansion range of thermal expansion values for SiC and SiC_f/SiC CMCs.

The unit cell volumes with third order polynomial fits are plotted in Figure 32. The polynomial coefficients for each fit curve are tabulated in Table 3. Calculated values of volumetric thermal expansions are plotted in Figure 33 for each of the cubic phases and Figure 34 for the phases which exhibited a phase transition.

Thermal expansion was found to be highly tailorable by controlling alkali cation stoichiometry. Comparing across temperatures, phases with cubic symmetry exhibited a monotonic decrease in volumetric thermal expansion at all temperatures with increasing cesium content. Comparing across compositions, the linearity of each curve increased with increasing

cesium content. These points illustrated that cesium-rich materials are more dimensionally stable across the temperature range.

Only $K[AlSi_2O_6]$ and $K_{0.8}Cs_{0.2}[AlSi_2O_6]$ existed in tetragonal symmetry above room temperature. In contrast to cubic phases, the tetragonal phases exhibited increasing thermal expansion with temperature. Thermal expansion tensors can give insight into the asymmetry of expansion in this system. The instantaneous thermal expansion ellipsoids of $K[AlSi_2O_6]$ at 25°C is shown in Figure 35 and at 600°C in Figure 36. From these, it was apparent that the volumetric expansion is due to expansion along the [100] and [010] axes. The cell contracted along the [001] axis contracted and did so more rapidly with increasing temperature. This reflected the inequivalence of the distortion of the two ring types as discussed previously.

The trends in thermal expansion behavior could also be attributed to the dominant distortions. Tetrahedral rotation and bond swinging (detected as contraction of T-O bonds) distortions observed in the tetragonal phases involved the motion of tetrahedra. By contrast, the dominant distortions in the prototypical cubic phase was extension of T-O and W-O coordination bonds. Both classes of distortions are driven by the redistribution of thermal energy and are bounded by the cohesive force of electronic bonding. Tetrahedral motion, however, did not directly oppose this force as did bond extension. Therefore, the scale of tetrahedral motion was much larger than that of bond extension.

The unique combination of distortion mechanisms observed in the pollucite end member were thought to be responsible for its exceptional dimensional stability. The moderate growth of W-O coordination polyhedra led to only small changes in the volume of the unit cell and the lattice across the temperature range.

Modelling Unit Cell Volume and CTE relationships

As noted previously, the synthetic conditions can have a significant effect on the temperature response of alkali aluminosilicate materials. While this work aimed to provide a complete solution to the synthesis and characterization of this system for EBC systems, there are fundamental insights to be gained by considering features of the system that are independent of the synthetic method chosen. Here, the method of tailorable thermal expansion was extended to allow targeted CTEs of any values in between any two fully-characterized systems.

Theoretical descriptions of the thermal expansion of solid solutions are typically based on a rule of mixtures approach. [89]–[95] The form of the equation governing rule of mixtures-type relationships for the volumetric CTE, β, is:

$$\beta = \sum_{i=1}^{2} h_i \beta_i = \sum_{i=1}^{2} \left(\frac{M_i}{\rho_i}\right) \beta_i = x\,\beta_1 + (1-x)\beta_2$$

where β_i's are the CTEs for the end members, h_i's are the volume fractions of the end members in solid solution, M_i's are the mass fractions of the end members in solid solution, ρ_i's are the densities of the end members. The coefficient x can be derived by recognizing that, in a two-component mixture, the volume fractions must sum to unity so that only one needs to be calculated explicitly.

It is also possible to calculate unit cell volumes of the target phases with a rule of mixtures equation and derive the CTE values with the procedure detailed in the previous section. The rule of mixtures for unit cell volume, V, is

$$V = \sum_{i=1}^{2} h_i V_i = \sum_{i=1}^{2} \left(\frac{M_i}{\rho_i}\right) V_i = xV_1 + (1-x)V_2$$

where V_i's are the volumes of the unit cells of the end members and the rest of the symbols have the same meaning as in the equation for β above.

Figure 37 shows the results for a rule of mixtures models for β and associated error. The input species used to make predictions were pollucite and $K_{0.6}Cs_{0.4}[AlSi_2O_6]$, the sample with the lowest cesium concentration that was found to be single-phase at room temperature, containing only the cubic polymorph. We assumed that the end members had equivalent elastic moduli. The two samples used for comparison with prediction were $K_{0.4}Cs_{0.6}[AlSi_2O_6]$ and $K_{0.2}Cs_{0.8}[AlSi_2O_6]$. The error in the model is relatively low, with a maximum of 0.132 10^{-5}/°C (9.13% at 1000°C) for the $K_{0.2}Cs_{0.8}[AlSi_2O_6]$ model and 0.030 10^{-5}/°C (6.1% at 400°C) for $K_{0.4}Cs_{0.6}[AlSi_2O_6]$.

Figure 38 shows the results for a rule of mixtures model for unit cell volume, V, and associated error. The error in the model did not exceed 4.83 $Å^3$ (0.19% at 200°C) in the model for the $K_{0.4}Cs_{0.6}[AlSi_2O_6]$ sample and did not exceed 4.98 $Å^3$ (0.19% at 1300°C) in the model for the $K_{0.2}Cs_{0.8}[AlSi_2O_6]$ sample.

The choice of end members for the rule of mixtures calculations is important to reduce error in the predictions. Preference should be given to end member compositions nearest to the desired unit cell volume or thermal expansion and where the stable phases are of similar crystal structure. More advanced rule of mixtures models may consider the effects of differing modulus values, but given the low error exhibited by the simple rule of mixtures models, the complications to the calculation of the CTEs and the additional expense and effort of determining modulus values, more advanced models are not justified here.

$Rb[AlSi_2O_6]$ System

Sample Preparation

$Rb[AlSi_2O_6]$ samples were prepared according to the geopolymer crystallization procedure described for the $K_xCs_{1-x}[AlSi_2O_6]$ system. The maximum temperature for the crystallizing heat treatment was 1200°C.

Phase Transition and Thermal Expansion

The $I4_1/a \rightarrow Ia3d$ structural phase transition occurred in $Rb[AlSi_2O_6]$ was complete by 506°C. This follows the trend of transition temperatures from $T_{K[AlSi2O6]} < T_{Rb[AlSi2O6]} < T_{Cs[AlSi2O6]}$. The lattice parameters for these three samples are plotted in Figure 39. The unit cell volume of cubic $Rb[AlSi_2O_6]$ versus temperature is overlaid onto the unit cell volumes of the leucite and pollucite series in Figure 40 and the thermal expansion curve is overlaid on that of the multiphase samples from the same series in Figure 41. Experimental data is presented in Table 23 in the Appendix.

The unit cell of t-$Rb[AlSi_2O_6]$ was larger than any of the other tetragonal phases in the leucite-pollucite series. It exhibited a greater rate of thermal expansion than the other tetragonal phases but followed the same trend of increasing until the phase transition, where it reached its maximum. The (001) lattice parameter was consistently larger than that of pollucite and contracts only slightly until convergence with the (100) lattice parameter and the completion of the phase transition.

The unit cell of c-$Rb[AlSi_2O_6]$ was larger than those of all of the materials in the leucite-pollucite series. It exhibited thermal expansion intermediate in magnitude to that of $K_{0.8}Cs_{0.2}[AlSi_2O_6]$ and $K_{0.6}Cs_{0.4}[AlSi_2O_6]$ and identical in overall curve shape to the rest of the series.

Modelling

The ionic radius of the Rb^+ cation in VIII-fold coordination is 161 pm.[96] Those for potassium and cesium are 151 and 174 pm, respectively. Thus, the comparable potassium-cesium composition of the same average cation size would give a sample of approximate stoichiometry of $K_{0.6}Cs_{0.4}[AlSi_2O_6]$ (average cation size = 160.2 pm, $\rho = 2.765\,\frac{g}{cc}$). A similar calculation by atomic mass using $\widetilde{M}_K = 39.098\frac{g}{mol}$, $\widetilde{M}_{Rb} = 85.468\frac{g}{mol}$, and $\widetilde{M}_{Cs} = 132.91\frac{g}{mol}$ predicts and equivalent composition of $K_{0.5}Cs_{0.5}[AlSi_2O_6]$ (average cation mass = 86.004, $\rho = 2.8475\,\frac{g}{cc}$). Matching thermal expansion behavior between $Rb[AlSi_2O_6]$ and either of these compounds would imply a generality to the rule of mixtures relationships derived for the leucite-pollucite series.

Qualitatively, the phase transition does exhibit intermediate behavior, with the transition temperature in between that of $K[AlSi_2O_6]$ and $Cs[AlSi_2O_6]$. Quantitatively, the unit cell volume and thermal expansion of the $Rb[AlSi_2O_6]$ sample did not match the rule of mixtures predictions. The much larger unit cell volume and CTE values imply that the rule of mixtures relationships derived for the leucite-pollucite series are not generalizable to other compounds based strictly on cation size or atomic mass. We discounted the effect of differing moduli in the previous section. This may not be appropriate for a generalized model.

Comments

A brief interlude for a note on the application of $Rb[AlSi_2O_6]$ as an EBC: Rubidium is an expensive reagent in any form. In the hydroxide form used here, it is more than 500 times more costly than potassium and 13 times more than cesium. Despite this, it offers one main advantage which may have value for the EBC application.

The melting point of the leucites increase with alkali cation radius. The melting point of leucite is 1686℃.[97] The melting point of pollucite is above 1900℃. Thus, rubidium leucite should have a melting point in between these. If a solid solution of rubidium leucite and pollucite follows a trend in thermal expansion and phase transition behavior similar to the leucite-pollucite solid solution, these materials could offer tailored thermal expansion over a useful range with higher melting points than the leucite-pollucite system.

K[AlSiO$_4$] System

The role of interframework cations thus understood, it is important to investigate the role of the framework units, themselves, on thermal expansion. To this end, we synthesized kalsilite, K[AlSiO$_4$], by the geopolymer crystallization method and studied them with *in situ* high temperature X-ray diffraction. Previous studies of kalsilite indicate a non-reversible phase transition that occurs at temperatures in excess of 950℃.[98], [99] The samples in this system were crystallized between 800℃ for sodium-rich species and 1000℃ for potassium-rich species. The material recovered from this procedure for the bulk composition K[AlSiO$_4$] was single phase hexagonal kalsilite (space group: P63).

In Figure 42, the volumetric thermal expansion of the potassium end member, kalsilite, K[AlSiO$_4$], is overlaid with those of select members of the $K_xCs_{1-x}[AlSi_2O_6]$ series. Experimental data is presented in Table 24 in the Appendix. Kalsilite exhibits low, monotonically increasing thermal expansion throughout the temperature range. Intensity of the diffraction peaks began to decrease at 1477℃, indicating melting of the sample. Previous studies of the material put the melting point as high as 1750℃.[100] The increasing thermal expansion behavior, contrasted with the decreasing thermal expansion of the leucite-pollucite series, could be a useful tool in manipulating the curve shape of a multiphase material if a suitable synthesis can be achieved.

This preliminary study into the thermal expansion behavior showed that changing the framework stoichiometry has a significant effect on the thermal expansion behavior of the tectosilicates that is qualitatively and quantitatively different from adjusting the size of the interframework cations.

Conclusions

In this chapter, we studied the atomic mechanisms underlying the thermal expansion and phase transformation in the $K_xCs_{1-x}[AlSi_2O_6]$ system. We established that the interframework cation can restrict distortions of the aluminosilicate framework structure. Increasing cation size suppressed the flexibility of the framework and therefore the thermal expansion and phase transformations that are largely driven by this flexibility.

We also introduced a preliminary study into changing the framework stoichiometry. The changes observed to the thermal expansion behavior from this change were starkly different from altering the interframework cation, inducing thermal expansion that increased, rather than decreased, with increasing temperature.

With regards to their potential as EBCs, the high melting points of these materials could offer improvements over the refractory capabilities of current generation EBC coatings, which have melting points near 1600°C. However, the successful candidate material must have thermal expansion compatibility with the underlying substrate, the SiC_f/SiC CMC.

This CMC system has been heavily studied. The thermal expansion across the operating temperature range is widely quoted at $4.5 \times 10^{-6}°C^{-1}$. [1], [2], [5], [101]–[103]. Figure 43 presents the CTE values of the most promising candidate materials overlaid with typical ranges of reported CTEs for SiC/SiC composites and rare earth disilicates.[104] For comparison with

literature values, which are widely reported in linear thermal expansion, the volumetric CTE values presented for the alkali aluminosilicates were converted to linear CTE values by the relationship

$$\beta = 3\alpha$$

which was derived in Chapter 1. The range of CTEs for SiC/SiC composites ranges from approximately 3-5 mm/mm-°C. From the graph, this represents a good match for materials with compositions between $K_{0.2}Cs_{0.8}[AlSi_2O_6]$ and $Cs[AlSi_2O_6]$. Given the implications of the rule-of-mixtures model also presented in this chapter and previous knowledge on the silica activity of the leucites, these materials could provide more closely matched CTE values with even higher melting points than the current state-of-the-art EBCs while matching the chemical resilience (by measure of silica activity).

Figures

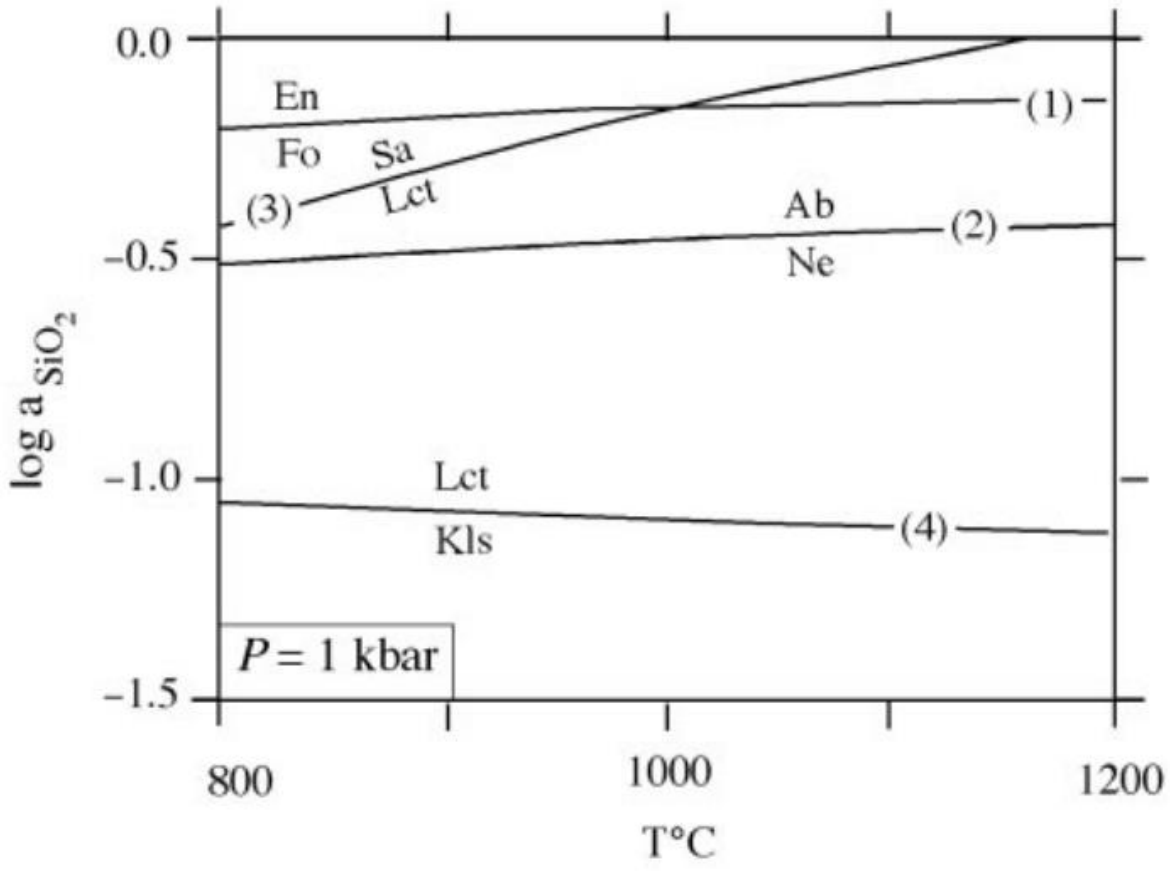

Figure 20 – T-log($a_{SiO2(aq)}$) diagram showing several common silica buffers in igneous rock at a pressure of 1kbar. The silica activity for the leucite-kalsilite equilibrium reaction is approximately log(-1.1) = 0.333 and decreases slightly with temperature.[61]

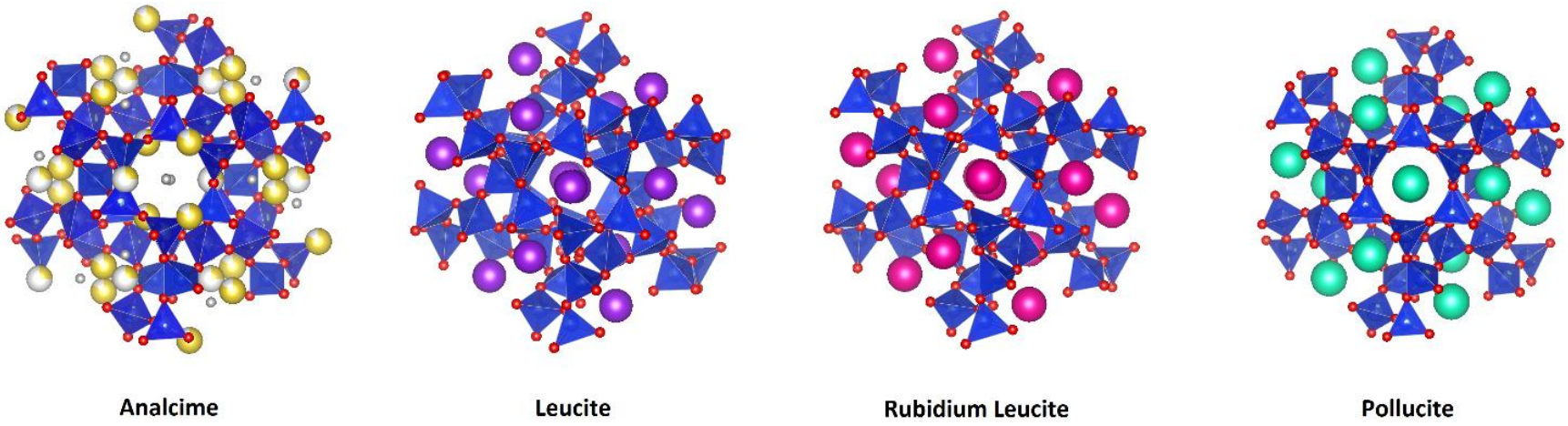

Figure 21 – The room temperature unit cells of the analcimes viewed down [111]-type directions. The arrangement of the alkali cations is different in analcime, where sodium atoms (yellow) occupy octahedral holes in the framework called "S-sites".

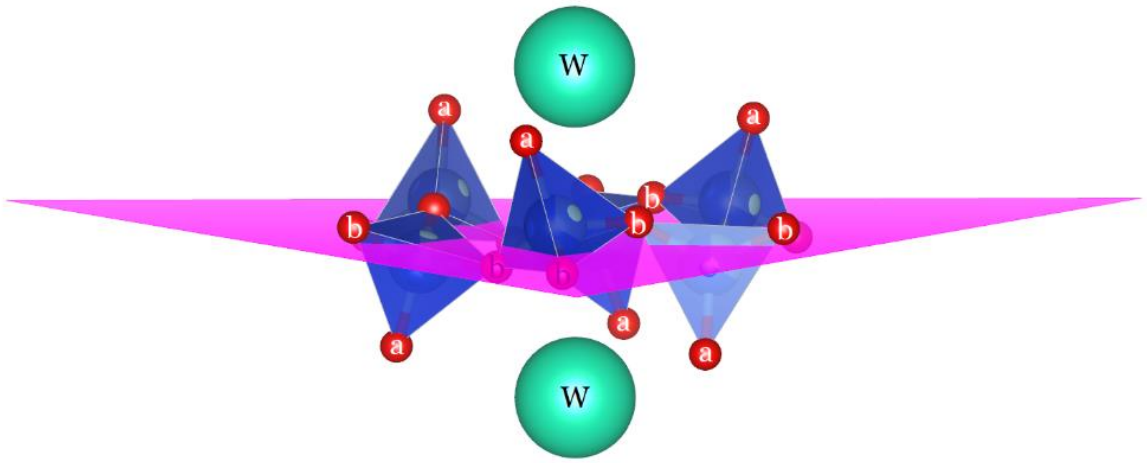

Figure 22 – An illustration of the first three framework distortion parameters: tetrahedral flattening, basal oxygen plane corrugation, and W-W spacing. An 'a' denotes an apical oxygen, a 'b' denotes a basal plane oxygen. The pink plane is a plane of best fit through the basal oxygen atoms. The W-sites between rings of the pore channel are occupied by alkali cations.

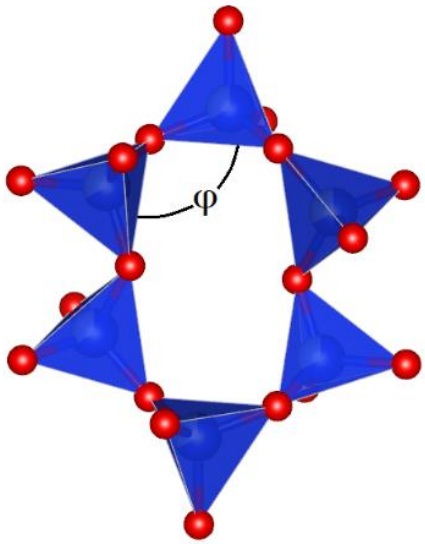

Figure 23 – An internal angle of the pore structure as defined for the measurement of tetrahedral rotation.

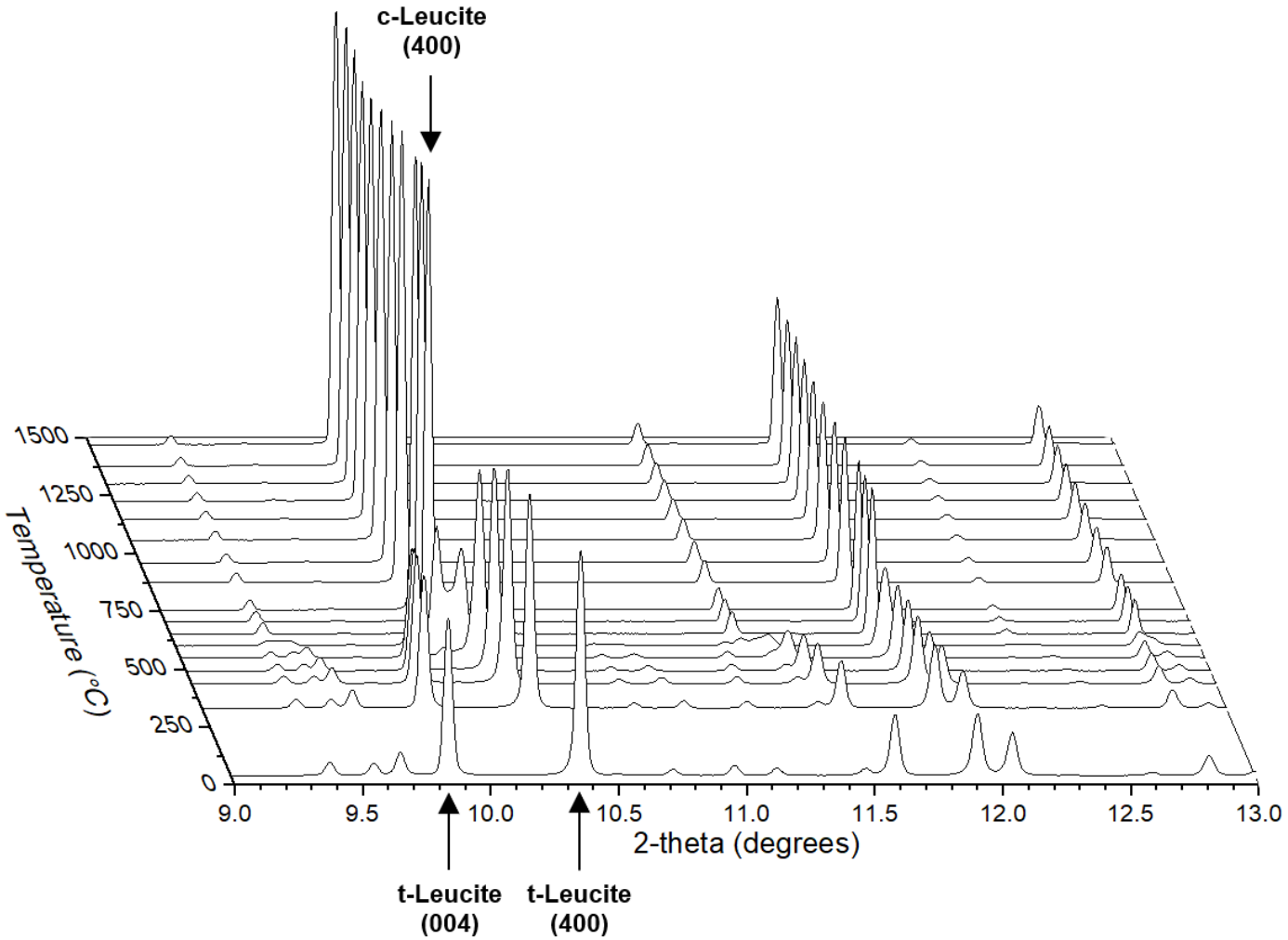

Figure 24 – A section of in situ HTXRD diffraction patterns illustrating the tetragonal-to-cubic phase transition in leucite

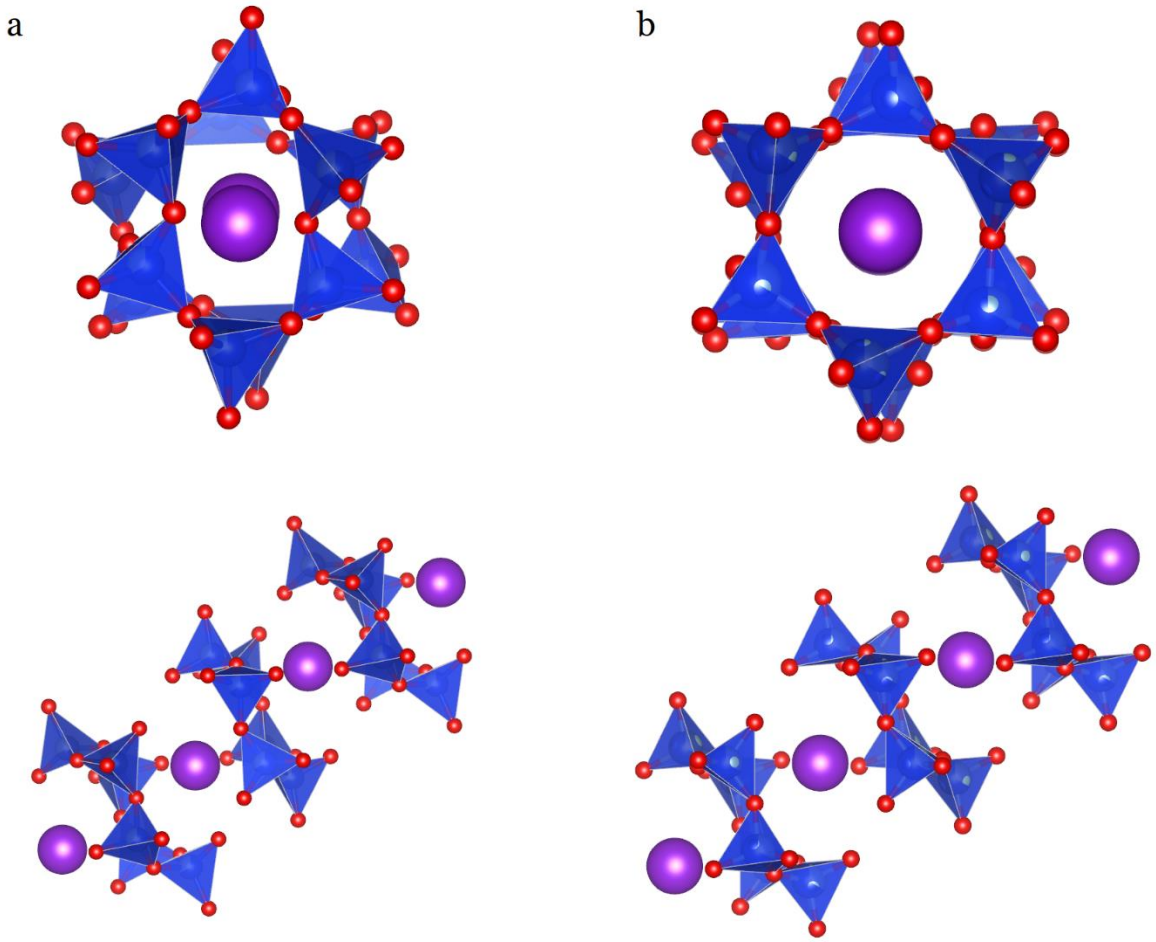

Figure 25 - The framework tetrahedral units that make up the pore channels in the leucite structure and the potassium cations that occupy the interstices. (a) Top, viewing down the axis of the pore channel in tetragonal leucite, the two non-equivalent rings can be identified. Bottom, a view across the pore channel showing the three pore channel rings in the unit cell. The top right and bottom left are equivalent by the symettry of the unit cell. (b) Top, viewing down the axis of the pore channel in cubic leucite, the symmetry-equivalent rings are overlapping. Bottom, a view across the pore channel shows all three symmetry-equivalent rings.

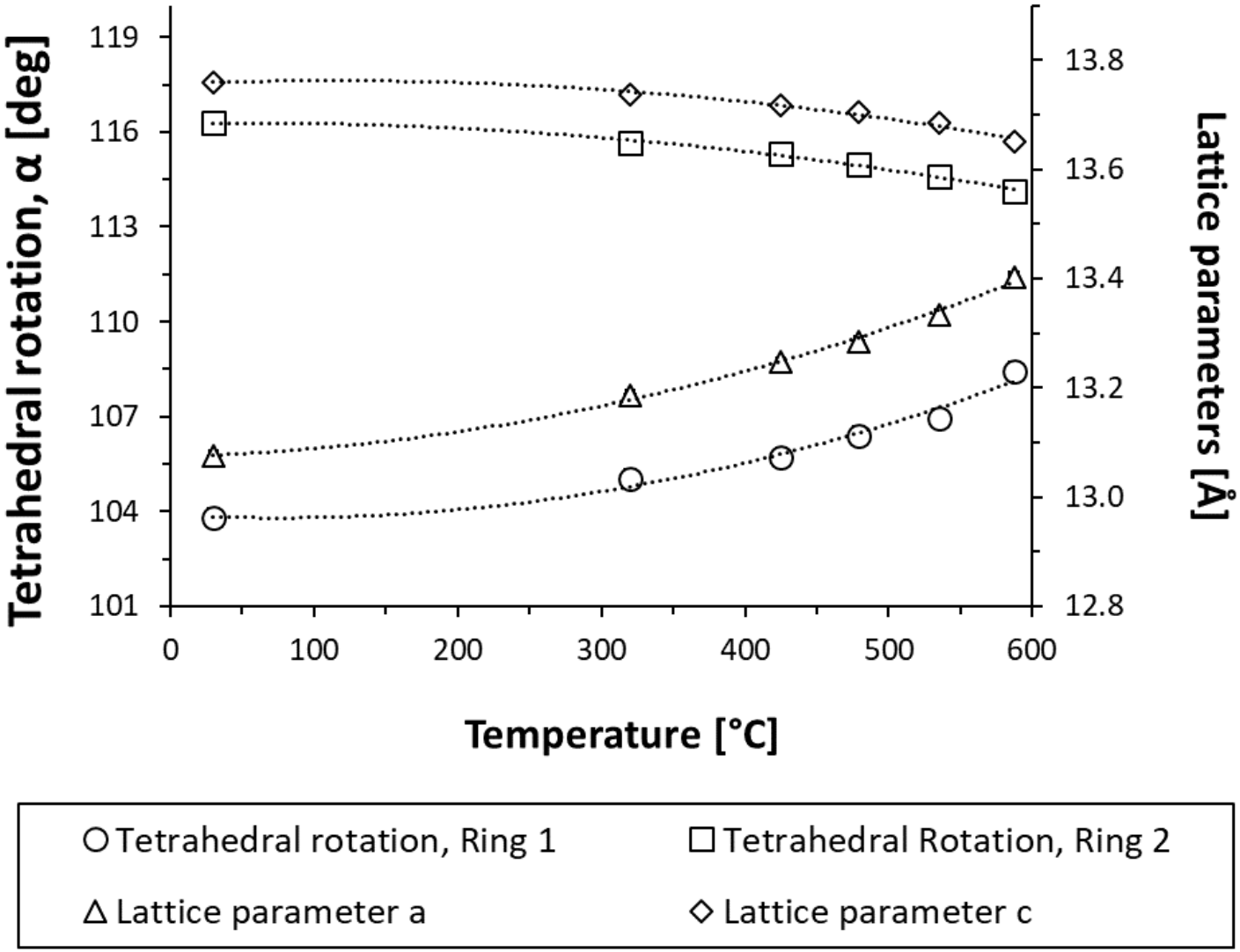

Figure 26 – The first dominant distortion mechanism in tetragonal leucite – tetrahedral rotation – overlaid with lattice parameters. Error bars are smaller than data points.

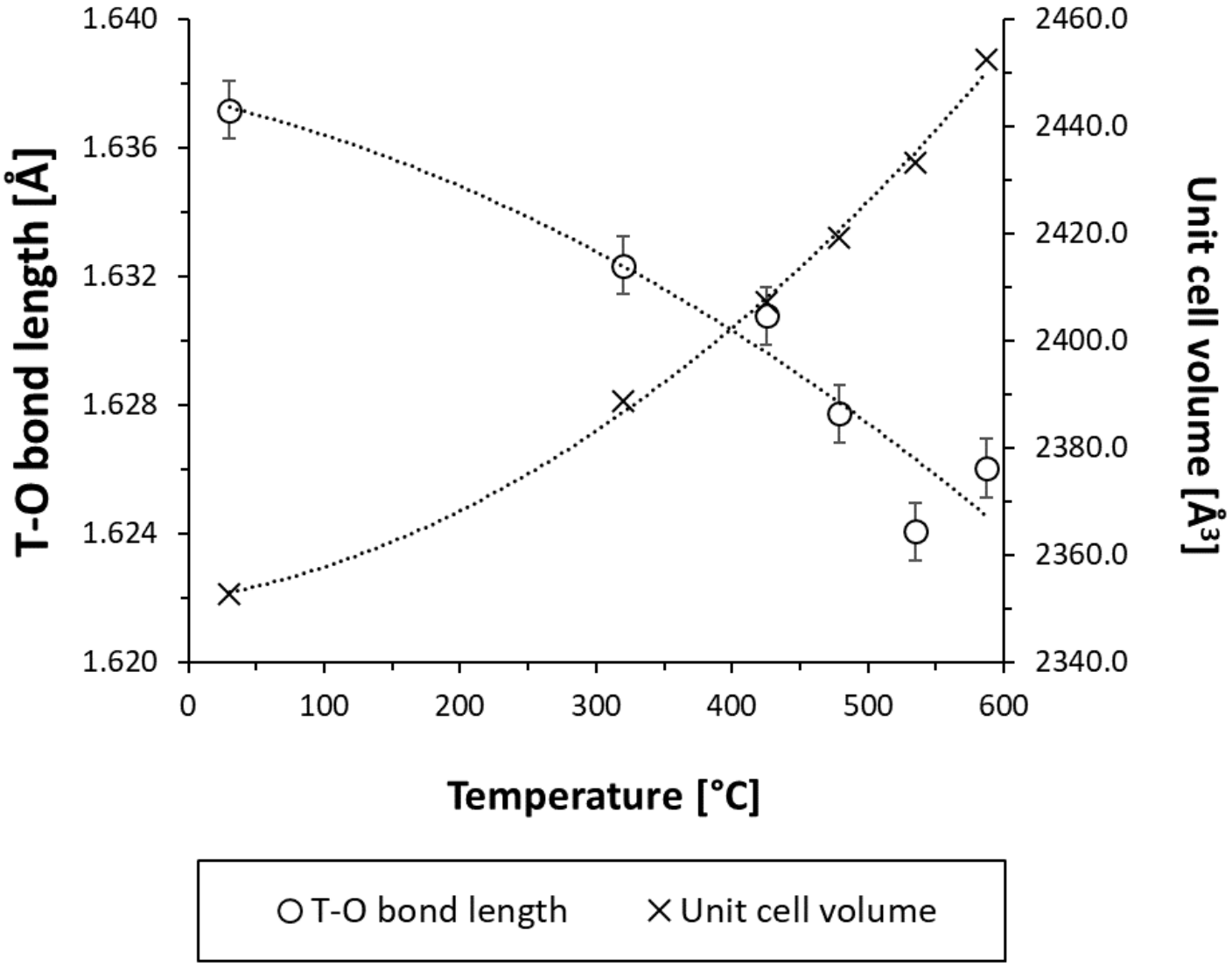

Figure 27 – The second dominant distortion mechanism in tetragonal leucite – T-O bond length – overlaid with unit cell volume.

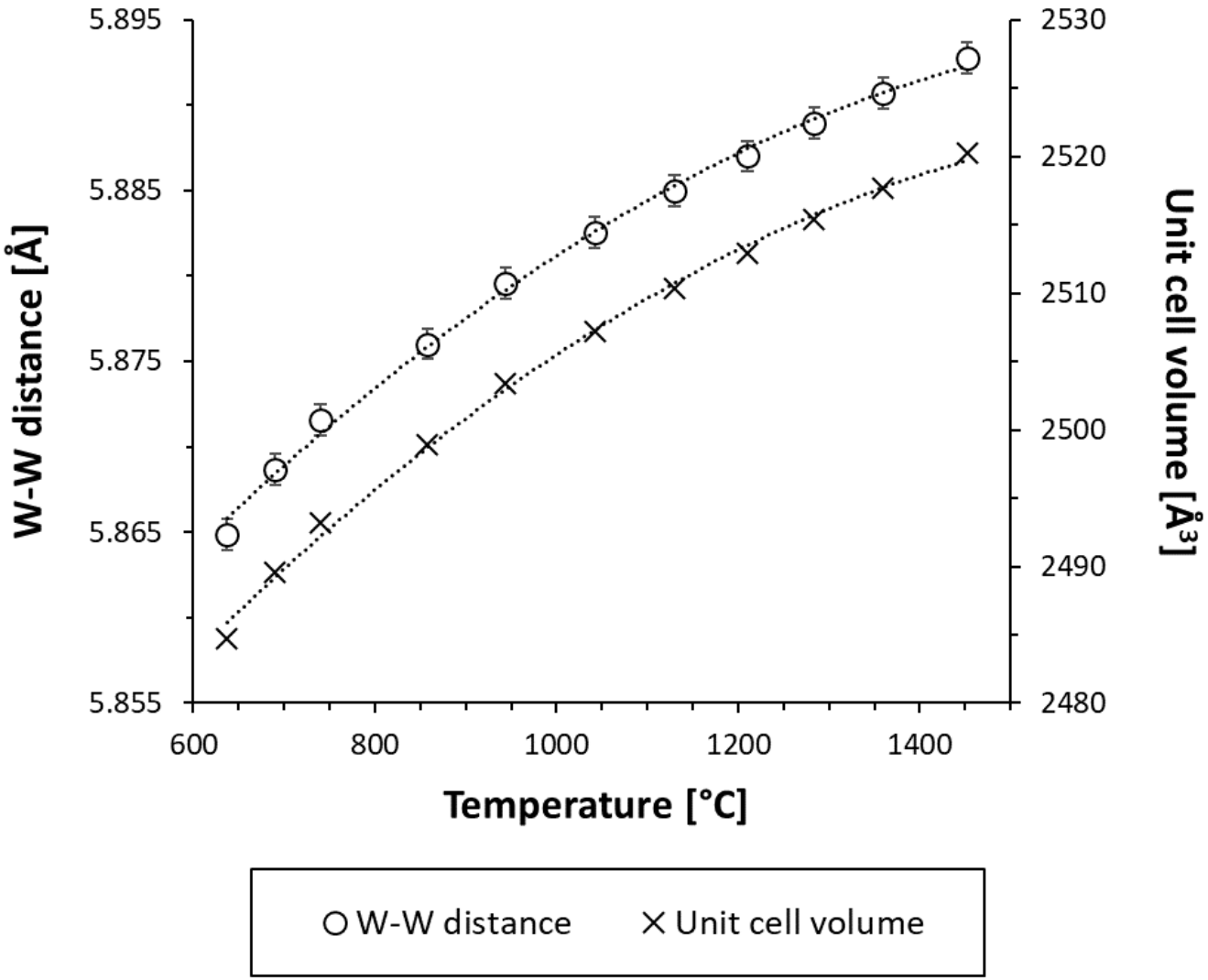

Figure 28 – The first dominant distortion mechanism in cubic leucite – W-W distance – overlaid with unit cell volume.

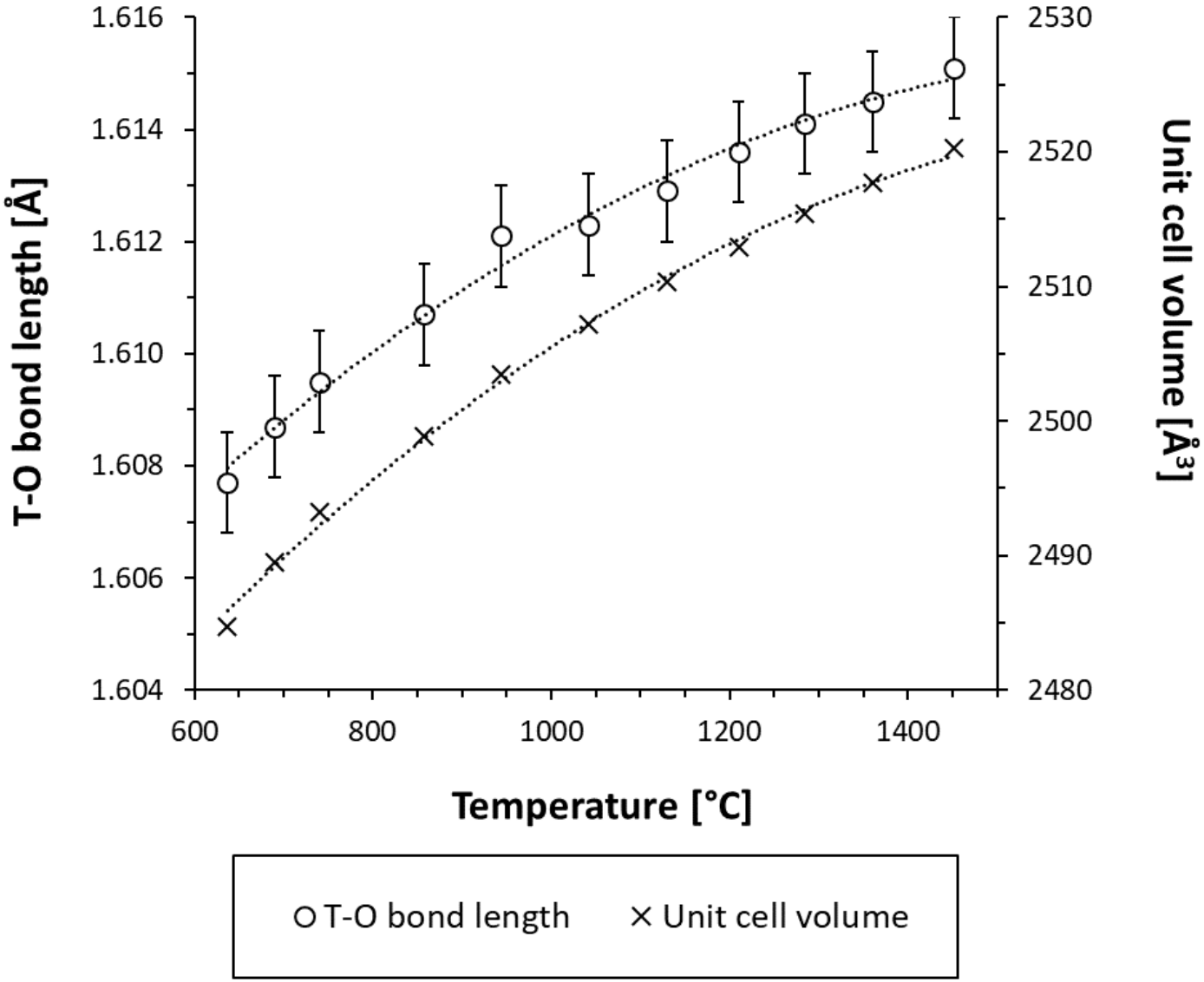

Figure 29 – The second dominant deformation mechanism in cubic leucite – T-O bond extension – overlaid with unit cell volume.

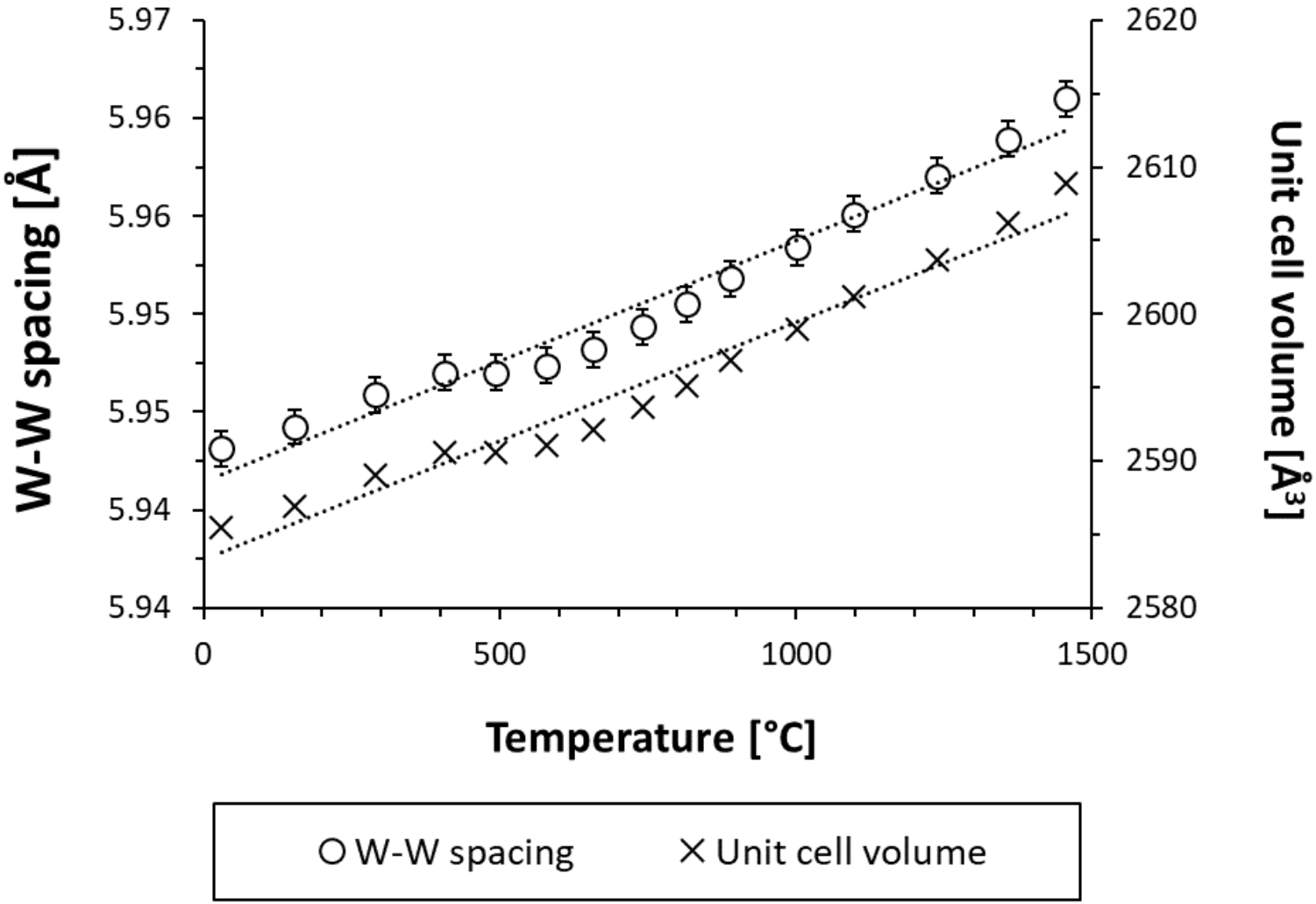

Figure 30 – The first dominant distortion mechanism in cubic pollucite – W-W distance – overlaid with unit cell volume.

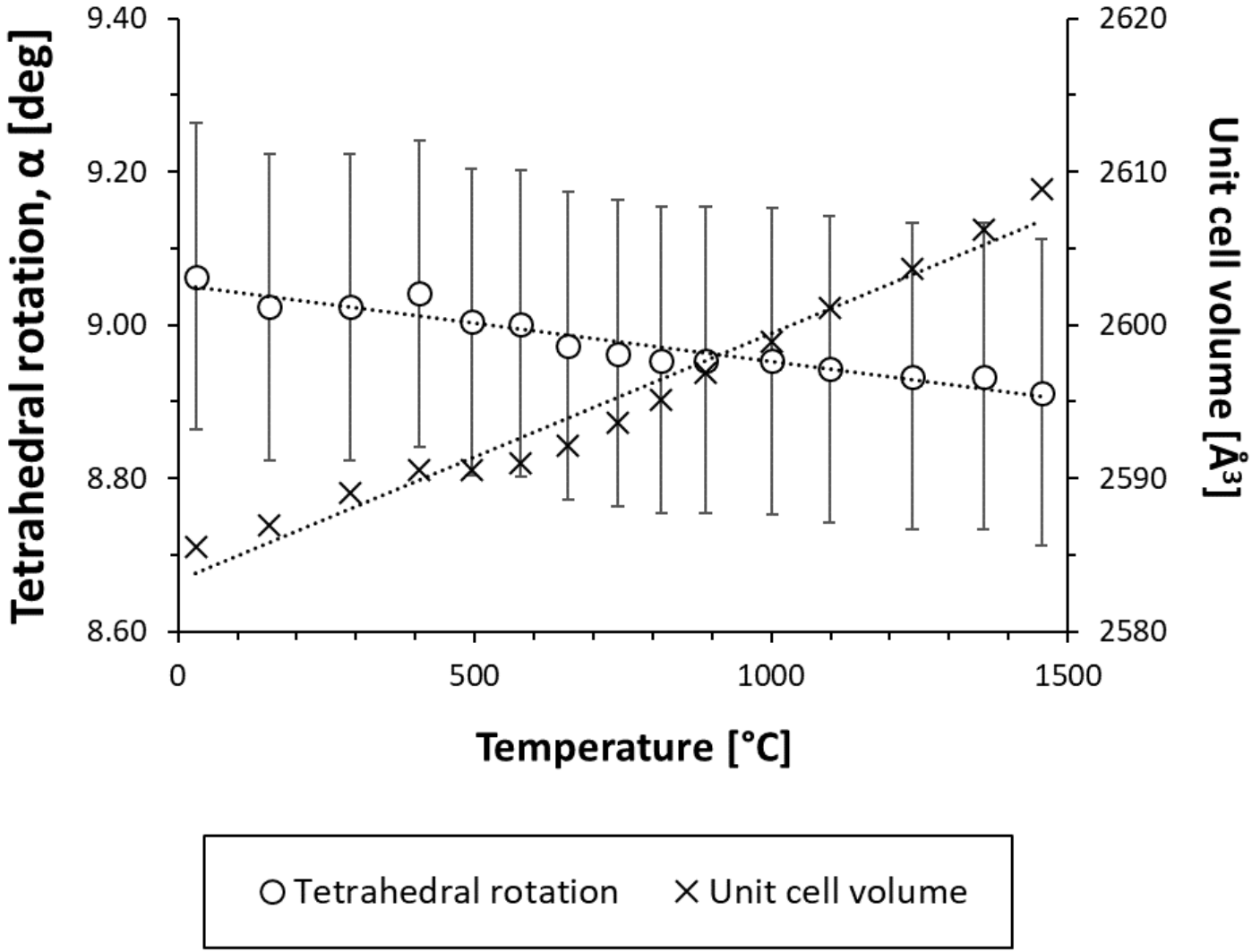

Figure 31 – The second dominant distortion mechanism in cubic pollucite – tetrahedral rotation – overlaid with unit cell volume.

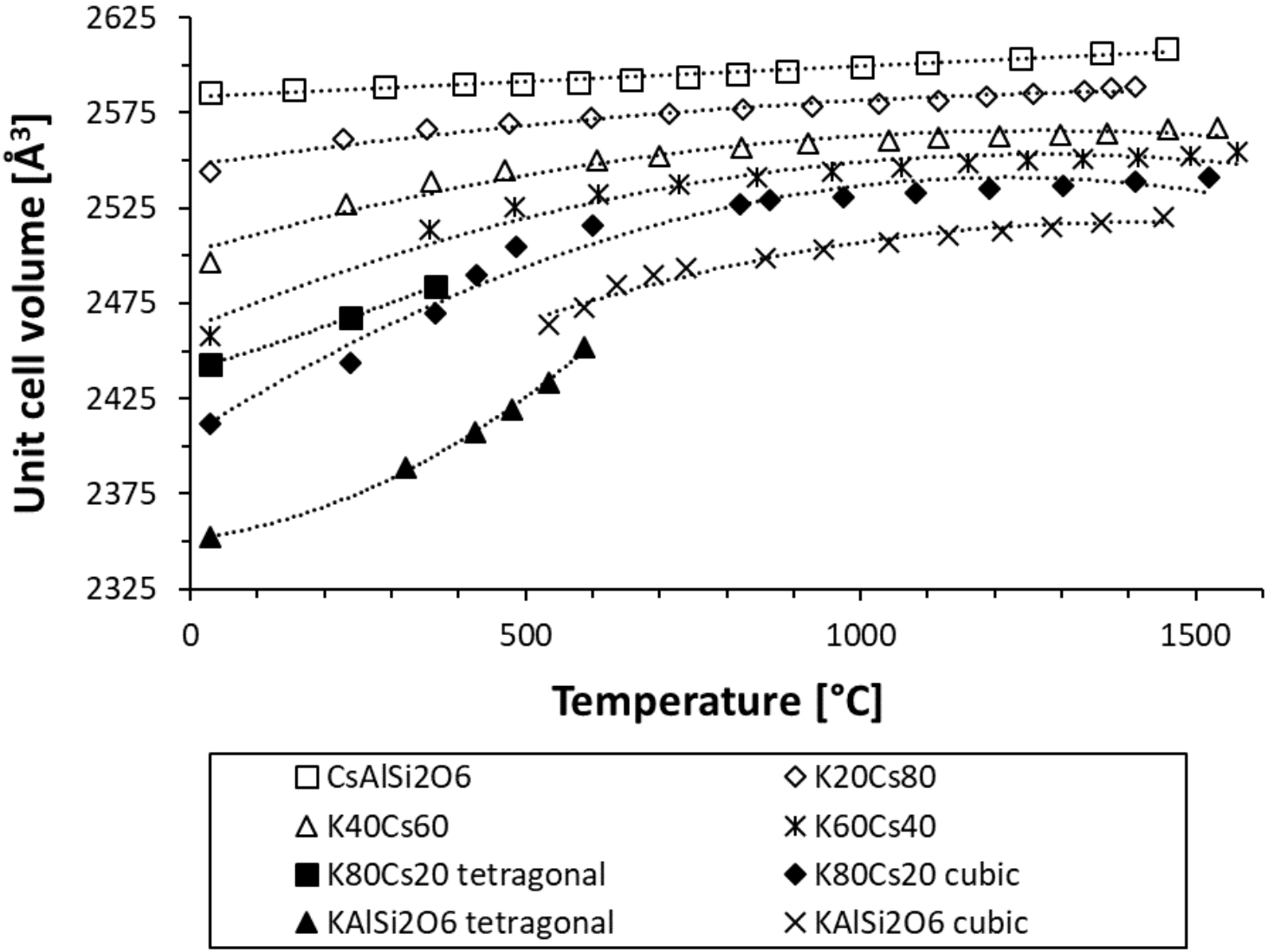

Figure 32 – Empirical unit cell volumes for the $K_xCs_{1-x}[AlSi_2O_6]$ series

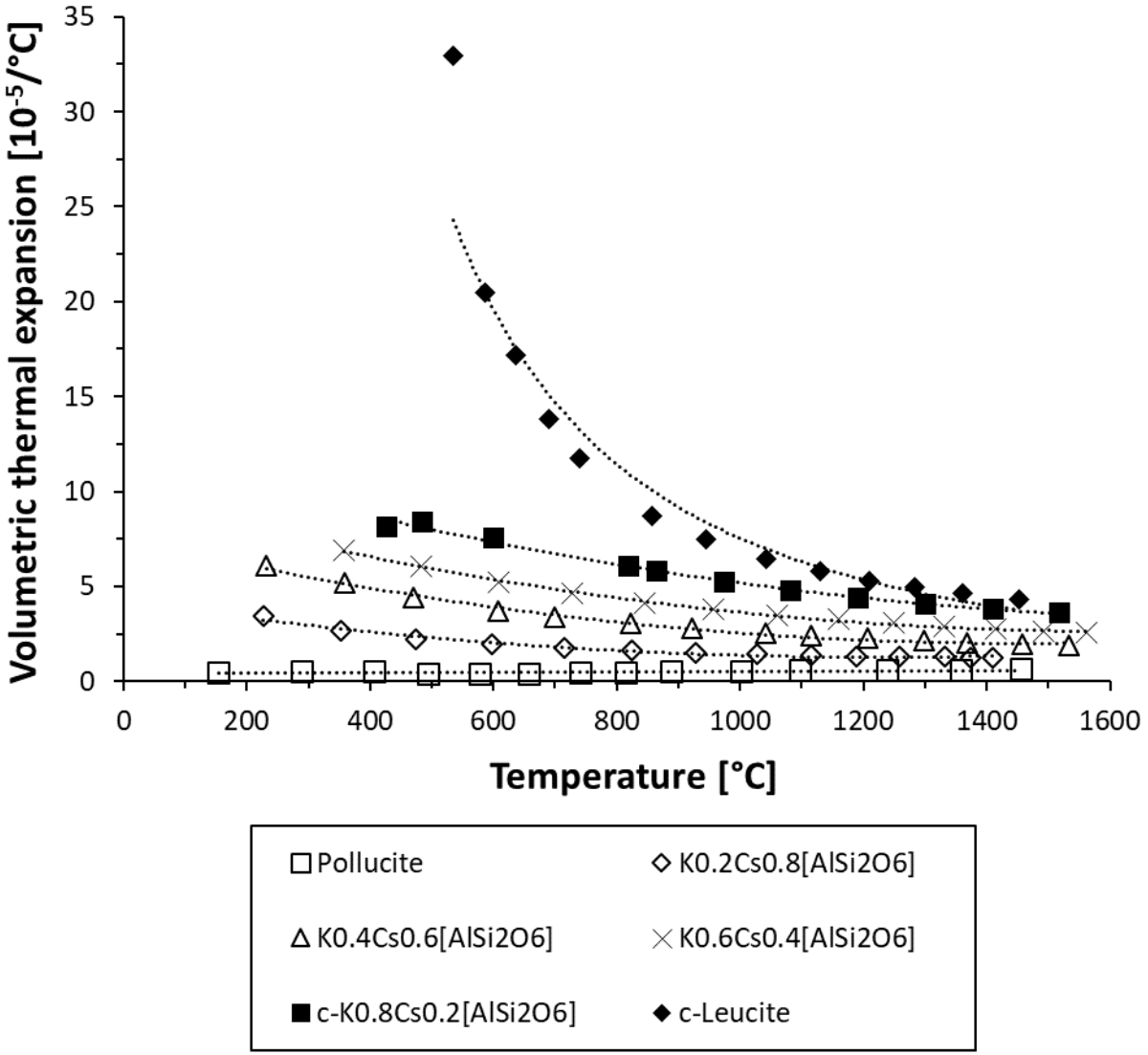

Figure 33 – Differential volumetric thermal expansion for cubic species in the leucite-pollucite series. Error bars are smaller than data points.

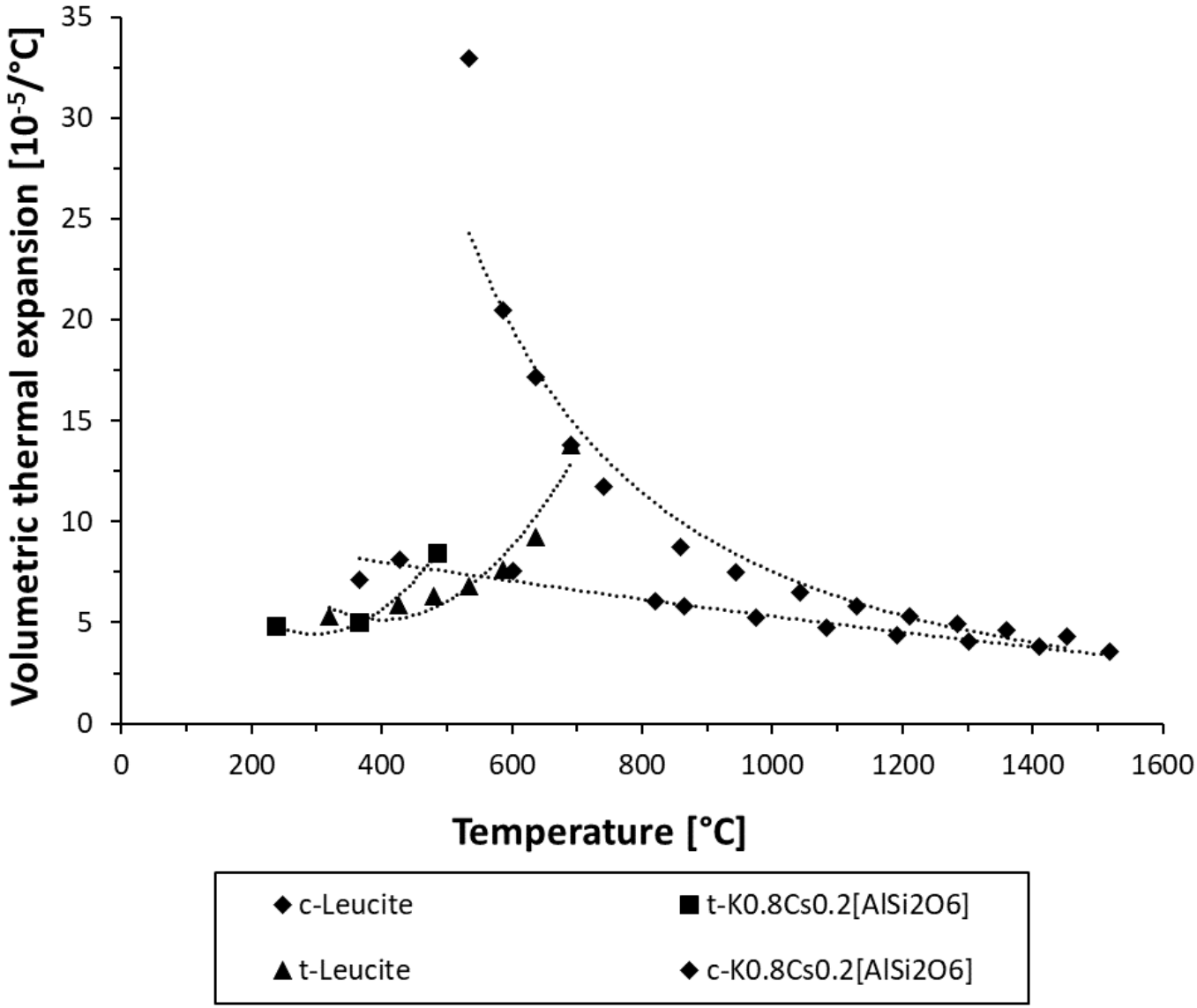

Figure 34 – Differential volumetric thermal expansion of samples exhibiting both tetragonal and cubic polymorphs.

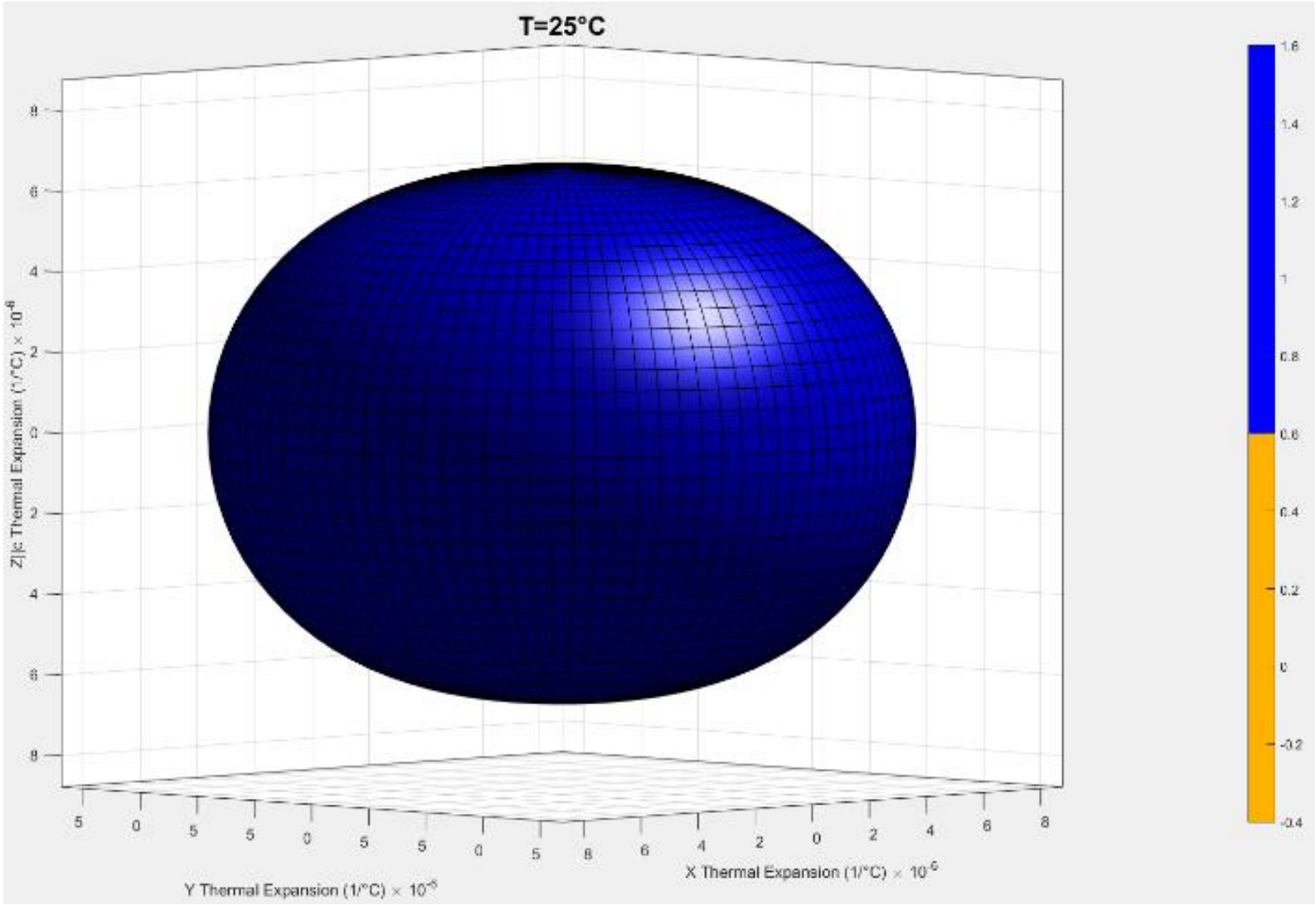

Figure 35 – Thermal expansion ellipsoid for tetragonal leucite at 25°C.

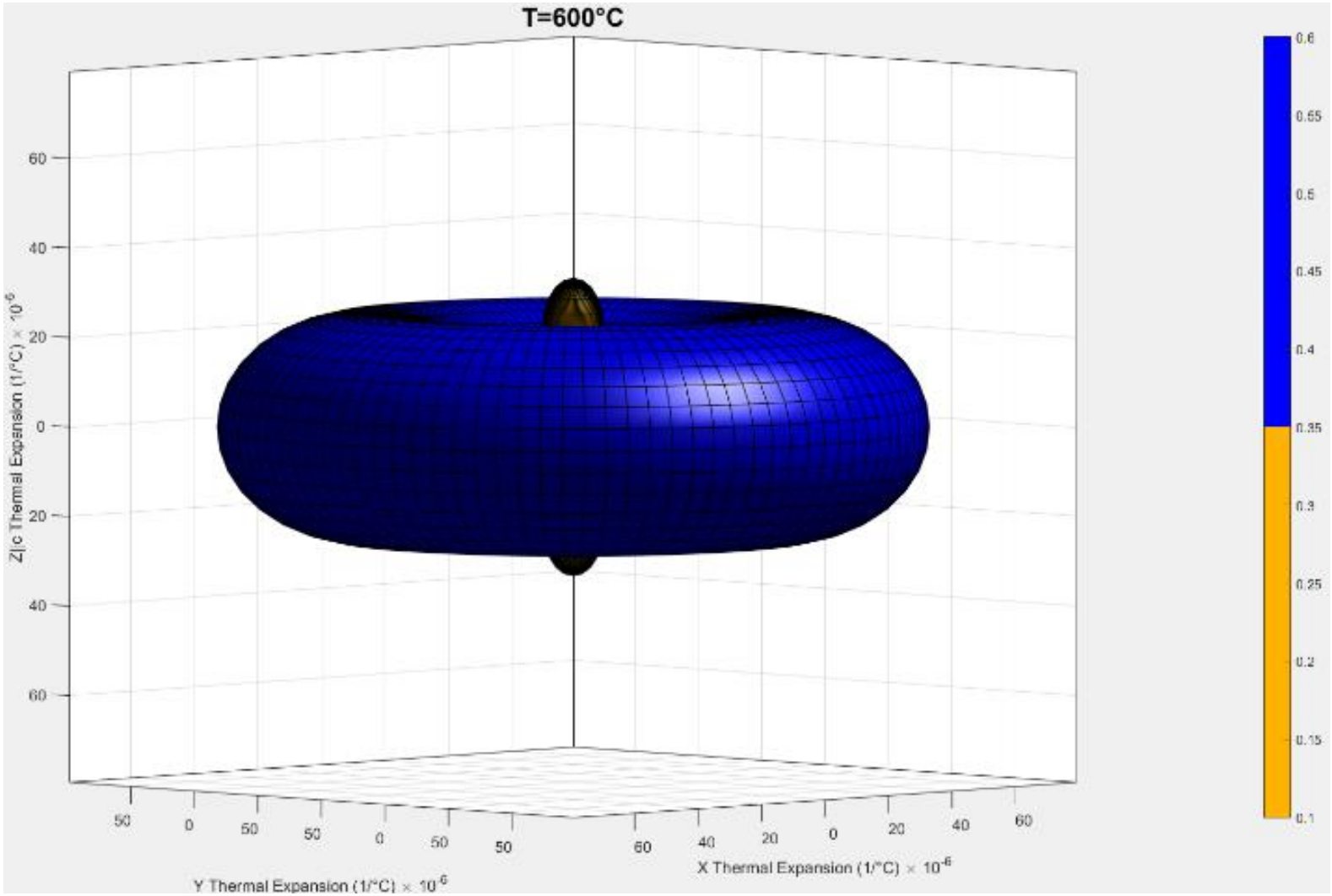

Figure 36 – Thermal expansion ellipsoid for tetragonal leucite at 600°C. The inner yellow peanut shape indicates directions of negative thermal expansion.

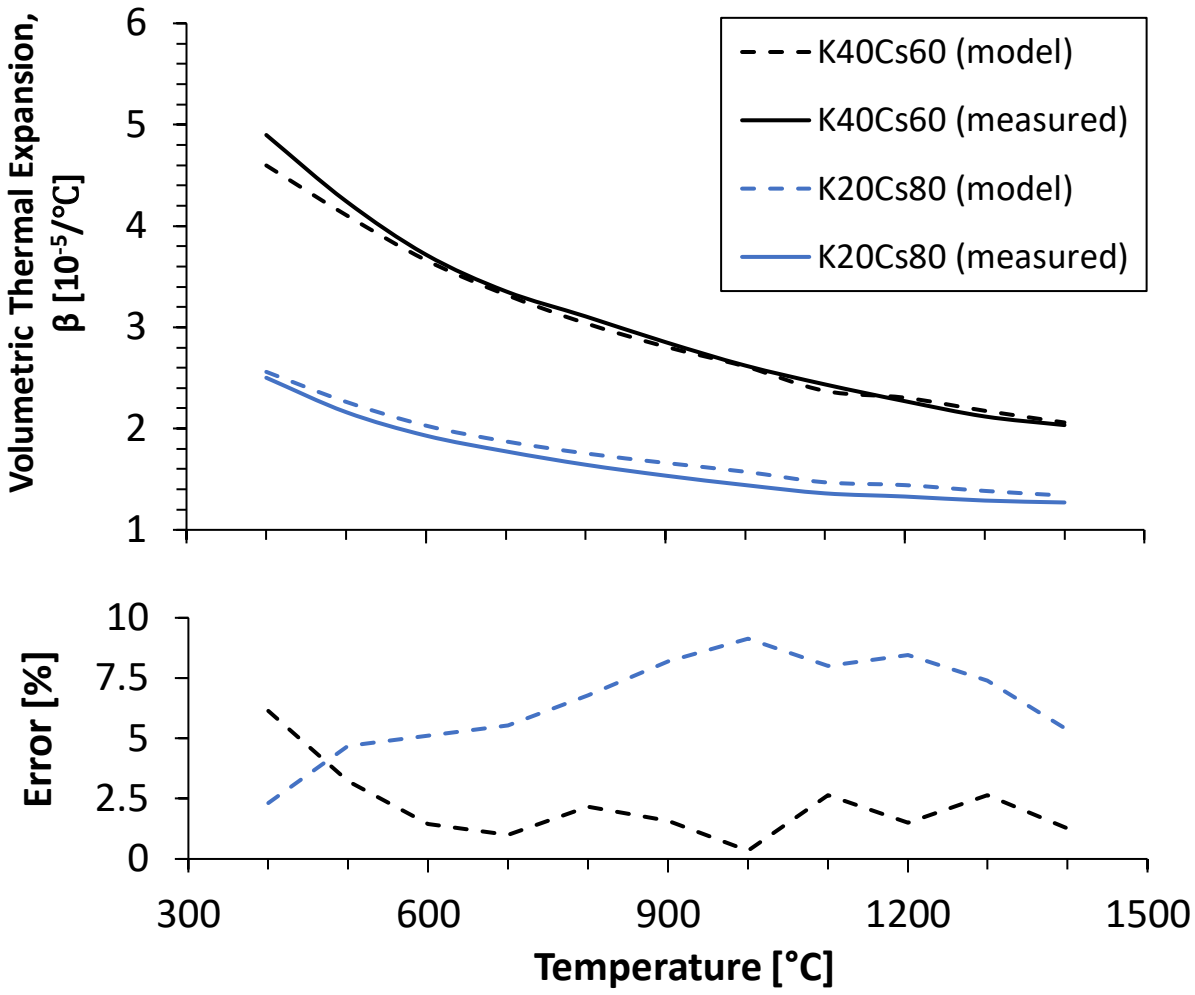

Figure 37 – (Top) Rule of mixtures models predictions of volumetric CTE compared with empirical data for K40Cs60 and K20Cs80 samples. (Bottom) The difference plots for both models.

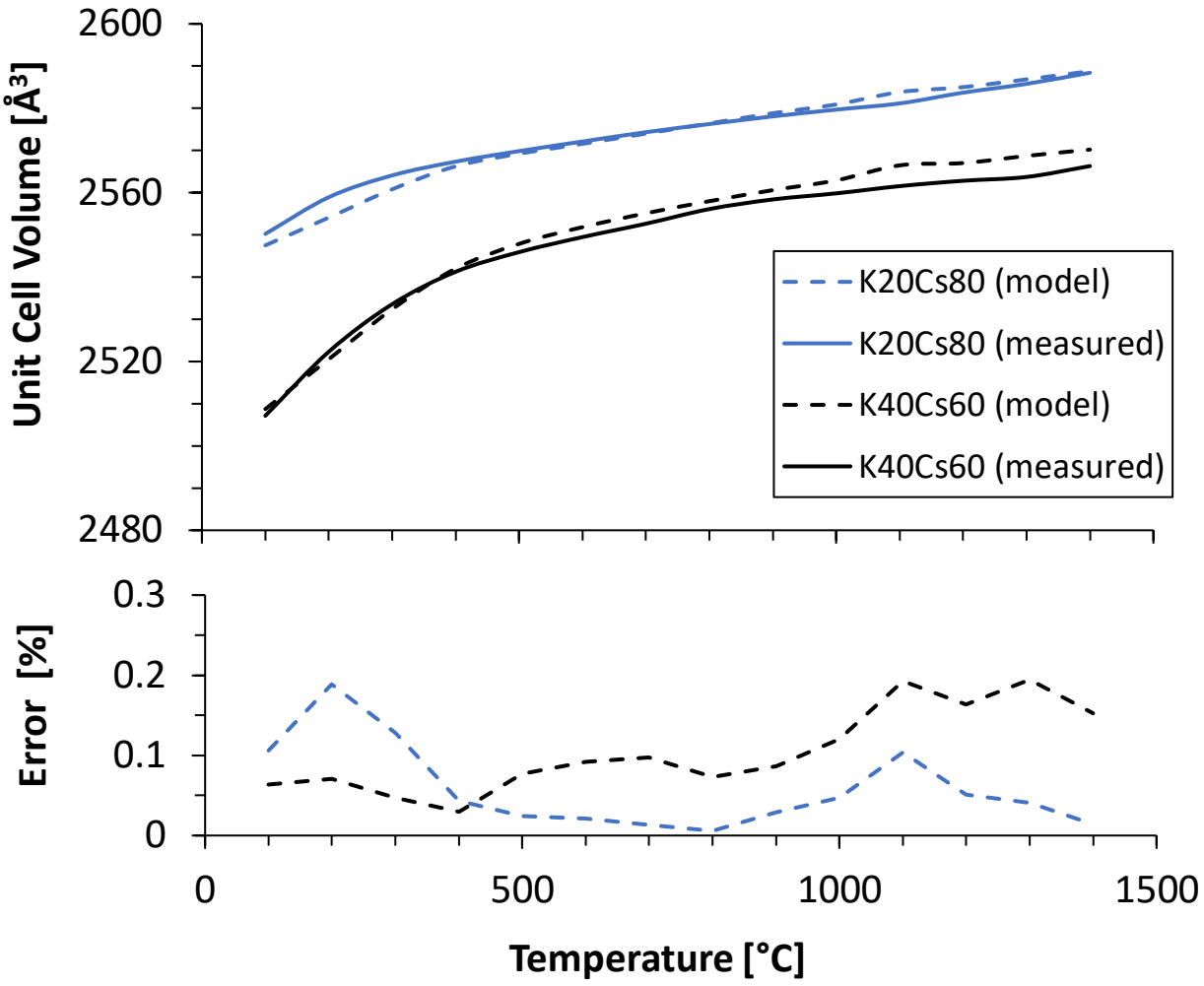

Figure 38 – (Top) Rule of mixtures models predictions of unit cell volume compared with empirical data for K40Cs60 and K20Cs80 samples. (Bottom) The difference plots for both models.

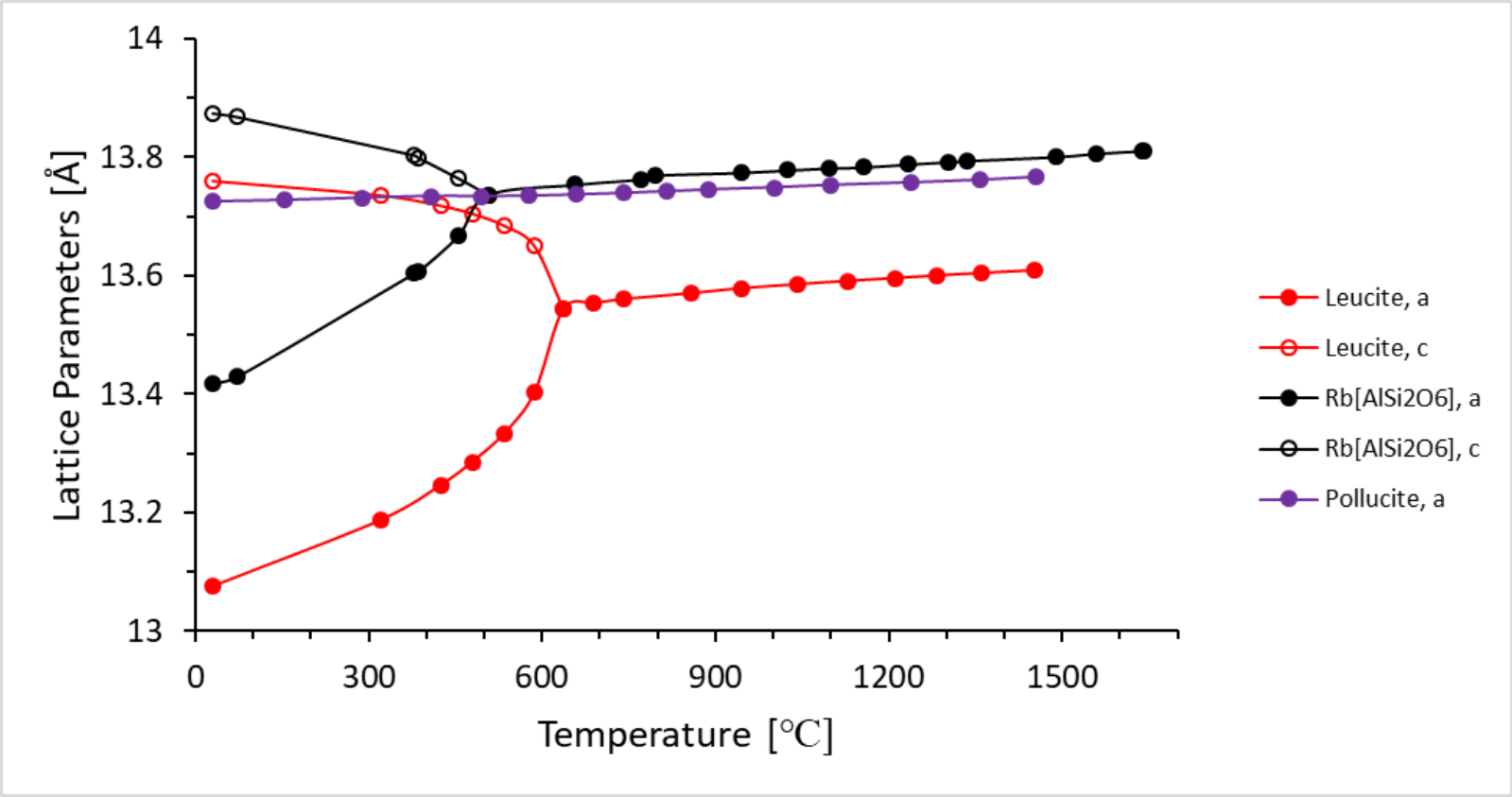

Figure 39 – Lattice parameters for $M[AlSi_2O_6]$, M=K, Rb, and Cs

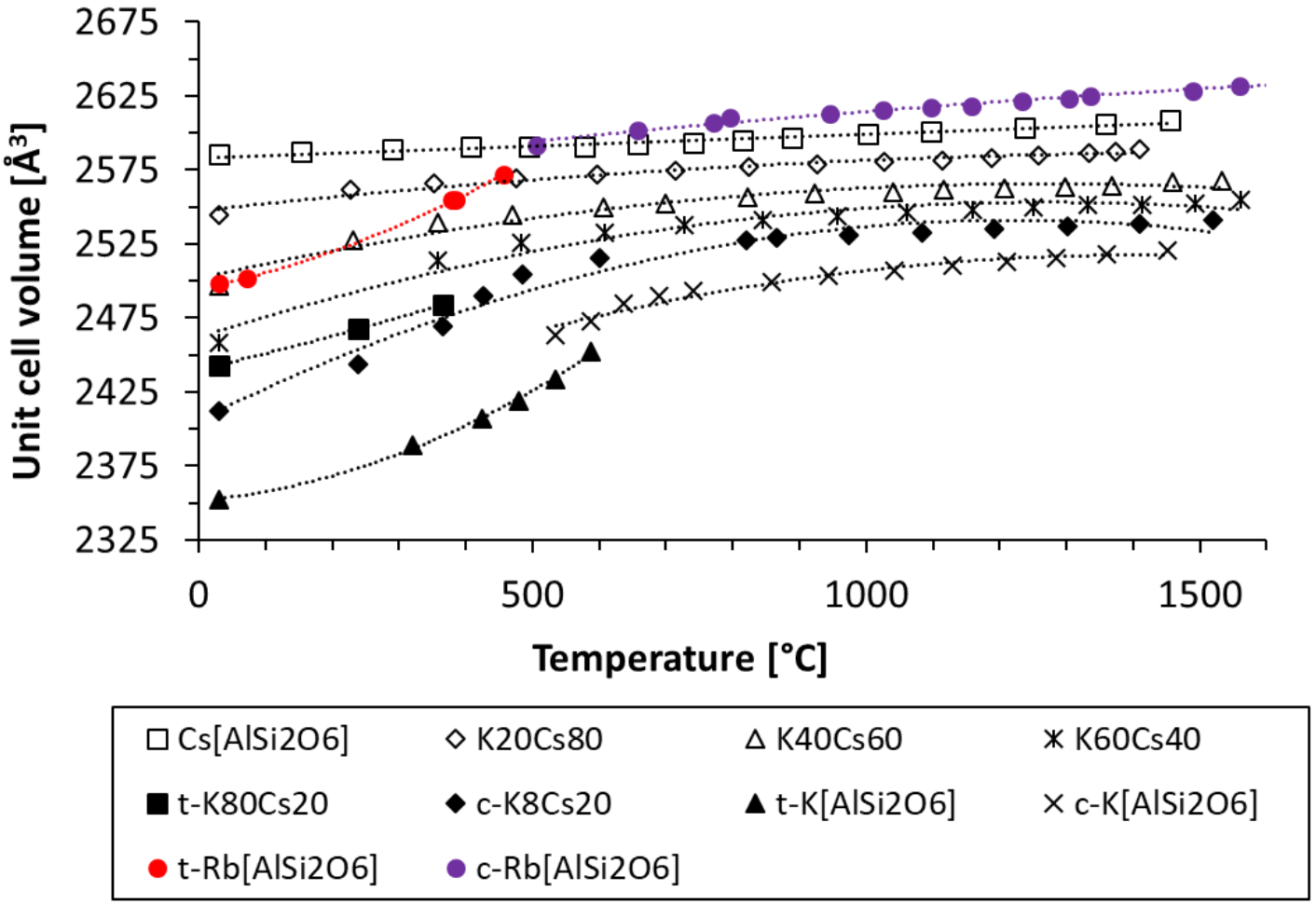

Figure 40 – Unit cell volume of $Rb[AlSi_2O_6]$ overlaid with that of the $K_xCs_{1-x}[AlSi_2O_6]$ series. The rubidium phase exhibited a large unit cell volume with respect to the other samples.

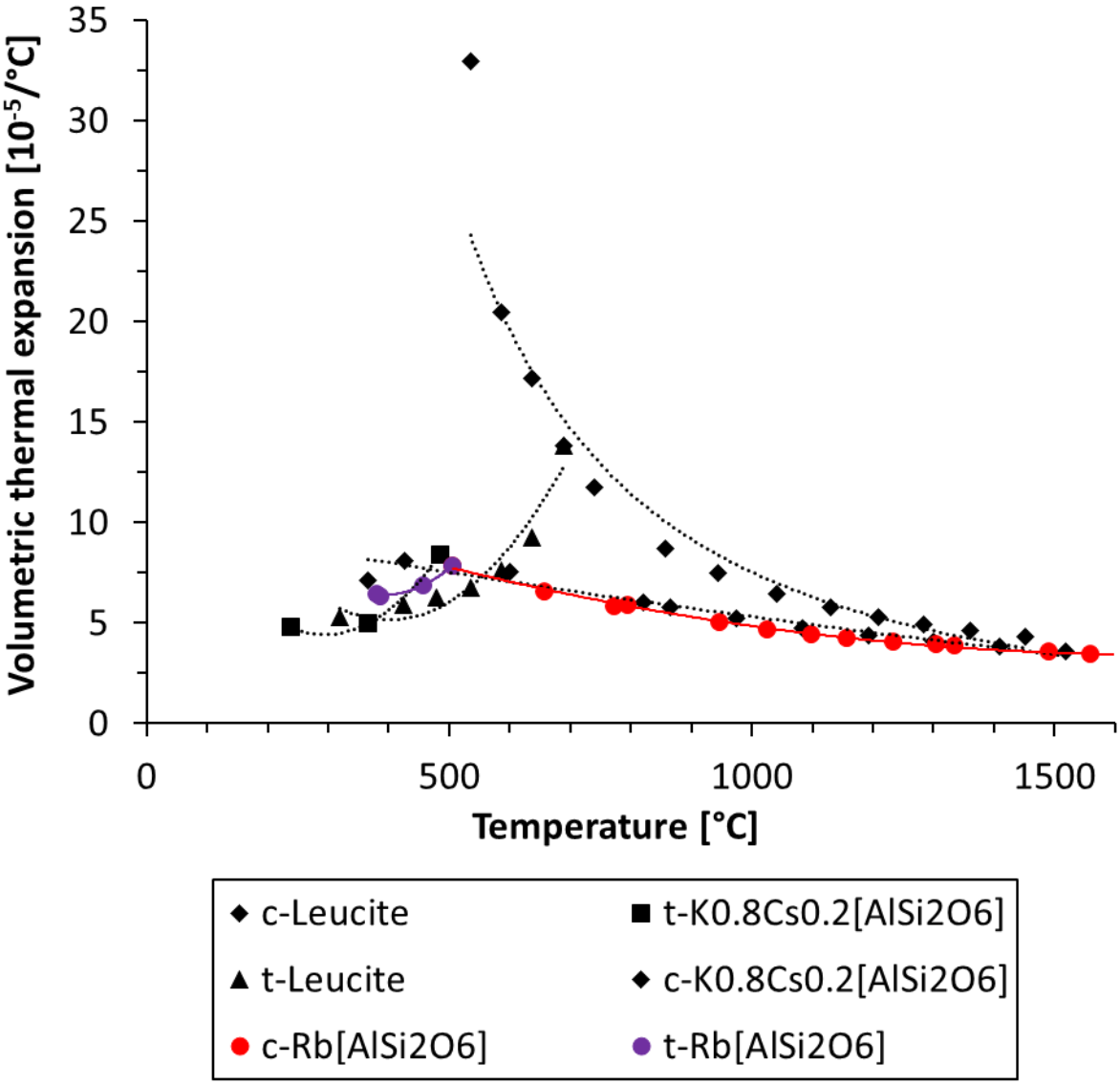

Figure 41 – Volumetric CTE of $Rb[AlSi_2O_6]$ overlaid with that of the $K_xCs_{1-x}[AlSi_2O_6]$ series. The CTE values fall in between those of the potassium and cesium end members and display similar curve shape trends. (Top) All cubic phases. (Bottom) Cubic and tetragonal phases.

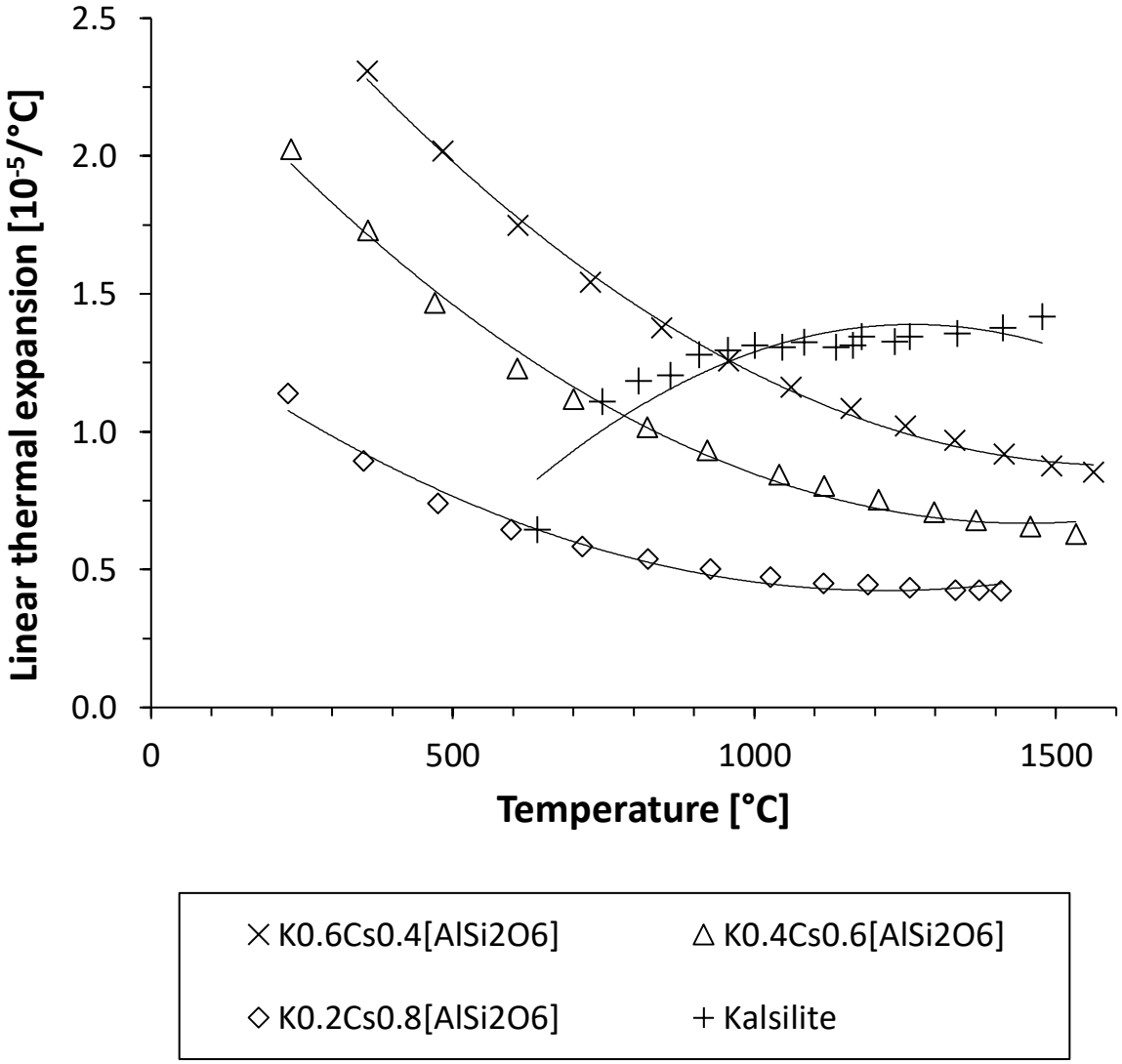

Figure 42 – Volumetric CTE of $K[AlSiO_4]$ overlaid with select members of the $K_xCs_{1-x}[AlSi_2O_6]$ series.

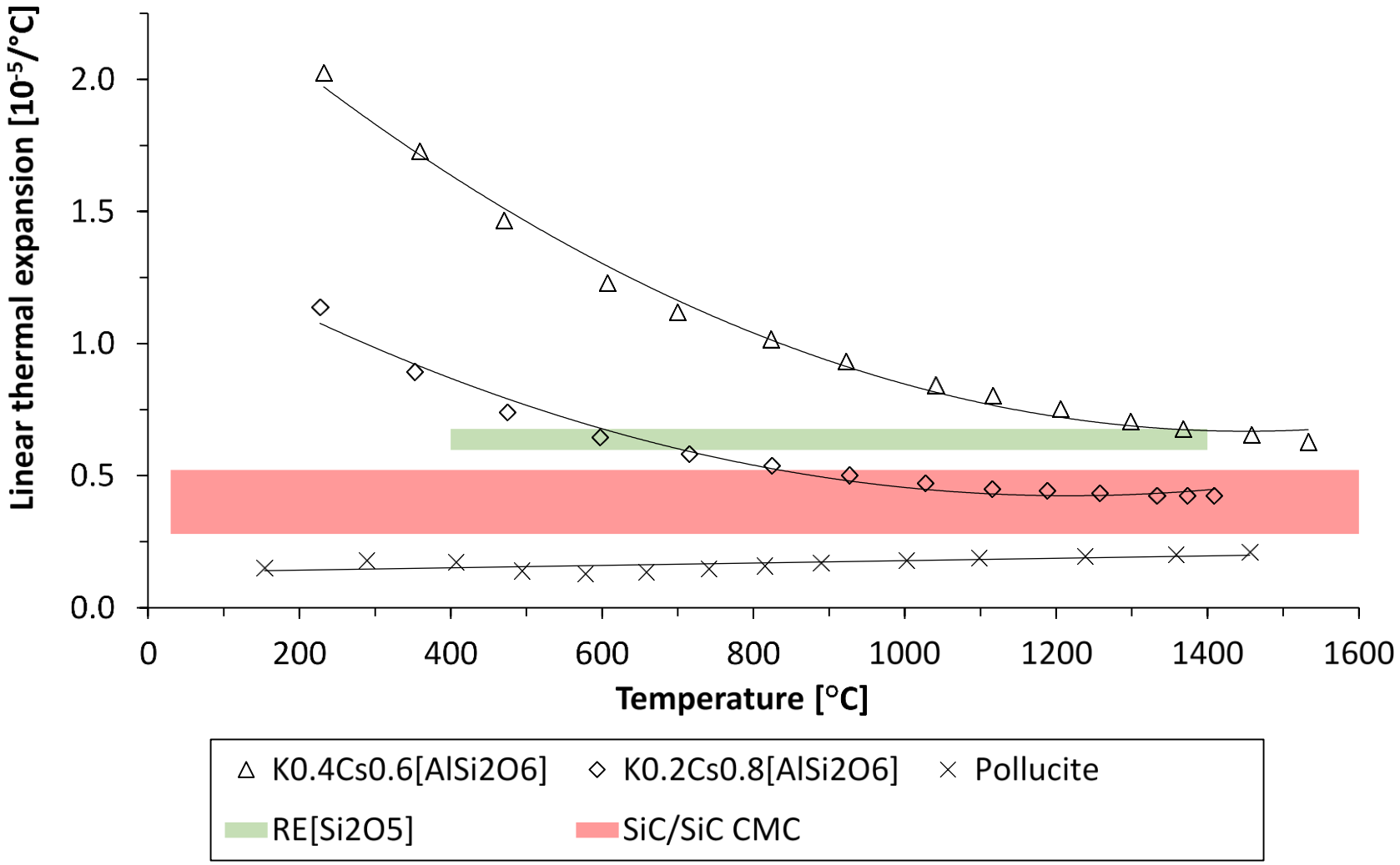

Figure 43 – Linear CTE values for promising candidates in the $K_xCs_{1-x}[AlSi_2O_6]$ series overlaid with reported ranges for rare earth disilicates ($RE[Si_2O_5]$) and SiC_f/SiC CMCs.

Table 1 – Correlation of distortion parameters with unit cell volume

	Tetrahedral flattening		Tetrahedral rotation		Basal oxygen-plane corrugation			Framework tetrahedral distortions			
Sample	Ring 1	Ring 2	Ring 1	Ring 2	Ring 1	Ring 2	W-W spacing	T-O bond length	Distortion index	Quadratic elongation	Bond angle variance
t-K[AlSi2O6]	-0.0864	0.8244	0.9844	-0.9938	0.6446	0.0834	-0.1697	-0.9503	0.4236	0.5300	-0.9656
c-K[AlSi2O6]	-0.3316	-0.3316	0.6056	0.6056	-0.4535	-0.4535	1.0000	0.9968	0.4408	0.2230	-0.5139
t-K0.8Cs0.2[AlSi2O6]	-	-	0.1216	-0.6475	-	-	0.0744	0.5536	0.9139	0.9187	0.1087
c-K0.8Cs0.2[AlSi2O6]	-	-	-0.7990	-0.7990	-	-	1.0000	0.9997	-0.8299	-0.8138	-0.1645
K0.6Cs0.4[AlSi2O6]	-	-	-0.0010	-0.0010	-	-	1.0000	0.9995	-0.6806	undef.	-0.7248
K0.4Cs0.6[AlSi2O6]	-	-	0.5477	0.5477	-	-	0.9856	0.9994	-0.4049	-0.7592	-0.8625
K0.2Cs0.8[AlSi2O6]	-	-	-0.3263	-0.3263	-	-	1.0000	0.9997	-0.1008	-0.2228	-0.7019
Cs[AlSi2O6]	0.2125	0.2125	-0.9135	-0.9135	-0.3857	-0.3857	1.0000	0.0767	0.7603	0.7538	-0.7137

Table 2 – CTE values in principal directions for the $K_xCs_{1-x}[AlSi_2O_6]$ series

Coefficient of Thermal Expansion (CTE) Tensor Values										
	$Cs[AlSi_2O_6]$	$K_{0.2}Cs_{0.8}[AlSi_2O_6]$	$K_{0.4}Cs_{0.6}[AlSi_2O_6]$	$K_{0.6}Cs_{0.4}[AlSi_2O_6]$	t- $K_{0.8}Cs_{0.2}[AlSi_2O_6]$		c- $K_{0.8}Cs_{0.2}[AlSi_2O_6]$	t-$K[AlSi_2O_6]$		c-$K[AlSi_2O_6]$
	α11	α11	α11	α11	α11	α33	α11	α11	α33	α11
T (°C)					(x 10^{-6})					
25	0.83	6.25	12.73	10.79	7.36	31.69	19.39	8.76	6.67	-
100	0.99	5.95	11.99	10.06	24.67	8.37	18.42	17.98	1.07	-
200	1.17	5.56	11.00	9.34	47.71	-22.13	17.14	29.67	-5.90	-
300	1.34	5.17	10.01	8.61	70.80	-51.21	15.85	41.57	-12.84	-
400	1.50	4.78	9.01	7.82	93.99	-77.94	14.57	53.75	-19.73	-
500	1.66	4.39	8.02	7.12	-	-	13.29	66.33	-26.56	15.40
600	1.81	4.00	7.03	6.42	-	-	12.00	79.31	-33.24	13.69
700	1.97	3.60	6.04	5.72	-	-	10.72	-	-	11.98
800	2.12	3.21	5.05	5.02	-	-	9.43	-	-	10.27
900	2.27	2.81	4.06	4.32	-	-	8.22	-	-	8.57
1000	2.42	2.42	3.06	3.62	-	-	6.96	-	-	6.86
1100	2.58	2.01	2.06	2.92	-	-	5.69	-	-	5.15
1200	2.72	1.60	1.04	2.21	-	-	4.43	-	-	3.44
1300	2.87	1.16	0.01	1.48	-	-	3.17	-	-	1.73
1400	3.02	0.48	-	0.24	-	-	1.90	-	-	0.02
1500	3.17	0.34	-	0.00	-	-	0.64	-	-	-

Table 3 – Coefficients of parametric fits of unit cell volume vs temperature in the form:

$$ax^3 + bx^2 + cx + d$$

Sample	a	b	c	d
Cs[AlSi2O6]	0.00E+00	6.00E-06	6.40E-03	2.59E+03
K20Cs80	3.00E-08	-9.00E-05	9.19E-02	2.54E+03
K40Cs60	4.00E-08	-1.00E-04	1.68E-01	2.49E+03
K60Cs40	5.00E-08	-2.00E-04	2.27E-01	2.45E+03
c-K80Cs20	5.00E-08	-2.00E-04	2.88E-01	2.40E+03
t-K80Cs21	0.00E+00	4.00E-05	1.07E-01	2.44E+03
c-K[AlSi2O6]	1.00E-07	-5.00E-04	5.86E-01	2.27E+03
t-K[AlSi2O6]	5.00E-07	-3.00E-04	1.75E-01	2.35E+03

CHAPTER 4 – MECHANICAL PROPERTIES OF BASALT-REINFORCED GEOPOLYMER COMPOSITES

The mechanical performance of both basalt fiber-reinforced and basalt minibar-reinforced potassium geopolymers was shown to be as good as or better than structural concrete across all metrics tested – compression, flexure, shear, and fracture toughness. The minibars impart exceptional load-bearing capability to the material even after failure.

Properties of comparable geopolymers, concretes, and/or structural ceramics are included where available. Every effort has been made to cite sources of high quality. However, the exact values of the mechanical properties of ceramic materials depend not only on the quality of experimental design and statistical rigor, but also on the specimen and loading geometry. This is the impetus behind the development of testing standards, upon which all the tests in this work are based, but even the most rigorous of these leave room for interpretation in their application. In the study of the mechanical properties of geopolymers, for example, there is ambiguity whether one should consult standards intended for concretes or structural ceramics, why there is a difference, or if the choice should be driven by application.

Motivation

An increase in the number of wildfire outbreaks in recent years has spawned interest in developing fast-setting, refractory structural materials for protective emergency shelters. Geopolymers have excellent refractory characteristics but exhibit brittle failure. Reinforcement phases are typically added to a matrix material to improve the toughness.

This investigation focused on the comparison of mechanical properties of geopolymer matrix composites reinforced with chopped fibers and with a novel reinforcement geometry, minibars. Both were made of basalt for its refractory compatibility with geopolymers. Where

available, comparisons are drawn to the properties of pure geopolymers and basalt-reinforced composites available in the literature.

Basalt Reinforcements

Basalt is the most common igneous rock on Earth, accounting for more than 90% of all volcanic rock. A basalt is defined by its compositional range, with at least 65% plagioclase ($Na[AlSi_3O_8]$-$Ca[Al_2Si_2O_8]$) by volume, less than 50% silica by volume, and less than 10% feldspathoid by volume. Basalt is highly resistant to chemical attack by acid, alkali, moisture and solvents. It is immune to nuclear and ultraviolet radiation and biological and fungal contamination.

The first patent was filed for the production of basalt fibers in 1923.[105] Basalt fiber technology was in development for classified military projects until 1995. It has since found use in numerous applications from construction and manufacturing.

Basalt fibers are produced for commercial use by extrusion of molten basalt. High acidity, low iron content basalt sources are selected and mined. The rock is then crushed, washed, melted, and extruded, requiring virtually no additives to give the properties which make it so desirable.

Typical commercial basalt fibers, including the ones used in this study, are typically between 10-20 μm in diameter. They exhibit higher tensile strengths and elastic moduli than commercial glass fibers and are significantly cheaper than carbon fibers.

In this work, the properties of geopolymers reinforced with either chopped basalt fibers or basalt minibars were investigated. The fibers were obtained from Sudaglass in Houston, Texas. The nominal size of the fibers was 15 μm in diameter and 25 mm in length.

The basalt minibars were a limited production item from Reforce Tech of Norway, which is now owned by Owens-Corning in Toledo, Ohio. The minibars consisted of bundles of fibers joined with an epoxy resin and were nominally 0.65 mm in diameter and 20 mm in length. The manufacturer claimed that the bundles were twisted along the length of the fiber with paddled ends formed by pressing. Optical examination revealed an average 180° twist between the ends, with a range from 0-540°, and a moderate flattening at the ends (Figure 44).

Weibull Statistics

Named for the Swedish mathematician and engineer Waloddi Weibull, who developed the rigorous mathematical description in 1951, the Weibull distribution is a continuous probability distribution that is parameterized by two or three parameters, depending upon the application.[106]

Due to the inherent random distribution of flaws in ceramics which result from processing and are believed to dictate their mechanical properties, the Weibull parameterization has been widely adopted to estimate the true value of their intrinsic properties. The Weibull probability cumulative distribution function is given as

$$f(x) = 1 - e^{-\left(\frac{x}{k}\right)^{\lambda}}$$

where x is the value of the independent variable (such as a material property determined from an individual test specimen), k is the "shape factor" of the Weibull distribution, and λ the "size factor". In the description of material properties, the estimation of material properties, the shape and size factors are analogues to the average and standard deviation of normal distributions.

The practical application of Weibull distribution to the description of mechanical properties requires a large number of samples, typically 10 or more, for statistical validity.[107]

The procedure for determining the parameters of the Weibull function is to linearize the CDF equation:

$$\ln[1 - f(x)] = \ln\left[e^{-\left(\frac{x}{k}\right)^{\lambda}}\right] = -\left(\frac{x}{k}\right)^{\lambda}$$

$$\ln\{-\ln[1 - f(x)]\} = \lambda \ln\left(\frac{x}{k}\right)$$

$$\ln\left\{\ln\left[\frac{1}{1 - f(x)}\right]\right\} = \lambda \ln(x) - \lambda \ln(k)$$

The value of the left-hand side is the "unreliability" of the sample. Unreliability values are typically approximated by Median Ranks methods, one of which is Benard's Approximation.[108] In this procedure, the test property values, x's, are arranged in ascending order of value and assigned a corresponding integer number, beginning with 1. The rank, y, is calculated as:

$$y = \frac{1}{1 - f(x)} = \frac{i - 0.3}{n + 0.4}$$

where i is the integer sample number assigned above and n is the total number of samples. The sets of $(x, y) = (material\ property, rank)$ coordinates are plotted on a log-log plot and the values of λ and k can be determined by linear regression. In the description of mechanical properties, these have special names: $\lambda = m$ is called the "Weibull modulus" and $k = \sigma$ is the "characteristic strength".

Sample Preparation

The geopolymer matrix material was synthesized by the reaction of potassium silicate solution with metakaolin, as described in Chapter 2. Reinforcement phases were added to the

matrix to a total of 10 volume percent of the matrix material. This was determined to be the maximum amount that could practically be added to the matrix without sacrificing workability.

All mixing was performed using a 100 liter, IKA stand mixer with a high-shear attachment (Figure 45). The matrix was synthesized under 10 minutes of mixing at 2000 rpm. Chamotte powder additive and minibar reinforcements were added under 1 minute of mixing at 250 rpm, fiber reinforcements were added under 45 minutes of mixing at 250 rpm. This extended mixing period was required to fully disperse the fibers. In this report, fiber-reinforced samples are referred to as KGPF and minibar-reinforced samples as KGPMB.

Preliminary investigation showed that the minibars would sink in the matrix material before it was fully set. This was not observed with the fibers, which were much lighter. To address this problem, 50-micron-particle size chamotte powder was added to the geopolymer matrix immediately after synthesis. The chamotte particles acted to directly increase the solids content of the gel without waiting for solidification of the geopolymer to occur and thus offer a much faster route to increase the viscosity of the matrix to support better distribution of the minibars. It was found that 70 weight percent addition of the chamotte powder was the optimal addition. Figure 46 shows compressive samples with and without chamotte added, illustrating the drastic improvement in distribution of the minibars in the sample.

Results

Compressive Strength

Cube samples 50.8mm (2in) on each side were prepared and tested according to ASTM C109.[109] The loading configuration is presented in Figure 47. Empirical data is presented in Table 25 in the Appendix. Representative compression loading curves for potassium-based, basalt fiber reinforced composites (KGPF) and potassium-based, basalt minibar reinforced

composites (KGPMB) in uniaxial compression are shown as Figure 48. The fracture surface characteristics of the two compositions were very different (Figure 49). The fiber-reinforced samples broke off in plate-like sections. The plates were similar in width to the size of the samples, indicating strong adhesion within the plates. This was likely due to clumping and bundling of the fibers such that failure occurred along the weakest interfaces between the bundles. The surface roughness of the plates suggested that there was a significant interaction between the matrix and the fibers on a local scale that increased the strength.

In minibar-reinforced samples, we observed smaller particles of almost no surface roughness, indicative of brittle failure of the matrix material. However, a minibar was typically embedded in several of the small particles and held them together after failure of the matrix material. This crack bridging behavior was the main strengthening mechanism of the minibars.

Finally, recalling that KGPMB samples contained an addition of 70 weight percent chamotte powder, we tested a small set of compressive samples of geopolymer with only chamotte added in order to determine the effect of this additive on the compressive behavior separate from the effects of the minibars. The fracture surfaces were similar to that of pure geopolymer and the maximum strength of three samples was 32.23 MPa, whereas the average strength for the KGPMB samples was 65.38 MPa (Figure 49). Thus, we concluded that the addition of chamotte alone did not have a significant impact on the properties of the samples.

A Weibull parameterization is shown in Figure 50 and summary statistics are tabulated with reference values in Table 4. The R-squared value for the linear fit against the KGPF results is low, suggesting the possibility of multiple flaw populations which may have caused distinct failure modes at different stress levels.

The ultimate compressive strengths of KGPF and KGPMB composite systems were 41% and 36% lower than that of the pure potassium geopolymer, respectively. Weibull moduli were 200% and 42% higher than the unreinforced geopolymer phase for KGPF and KGPMB, respectively. This suggests that the reinforcements are acting as flaws greater in size and number than in the pure geopolymer and creating stress concentrations from which critical failure initiated. The greater number of individual fibers in the KGPF samples led to the larger spread in measured properties.

Flexure Strength

Two sets of flexure specimens were tested in 4-point bending to identify specimen size effects on mechanical properties. One set of four samples of 76.2 mm x 76.2 mm x 279.4 mm (3 in x 3 in x 11 in) geometry (specified by ASTM C78) was tested to represent the materials with "discontinuous" reinforcement phases, defined as having a reinforcement size less than one third of the smallest cross-sectional dimension.[110] A second set of twenty samples of 27.9mm x 27.9 mm x 152.4 mm (1 in x 1 in x 6 in) (compatible with ASTM C1161) was tested to represent the materials with "continuous" reinforcement phases.[111] The loading configuration is shown in Figure 51. Empirical data is presented in Table 26 in the Appendix.

Representative flexure loading curves for KGPF and KGPMB in four-point bending are shown as Figure 52. Ultimate flexural strengths and flexural toughness were much higher in KGPMB samples. Slow fiber pullout due to the twisted surfaces of the minibars also result in the graceful failure of KGPMB samples, rather than the sudden, brittle failure observed in KGPF samples.

The larger specimens were useful in discriminating between matrix-reinforcement interactions. The results of slow fiber pullout can be seen in Figure 53, where the KGPMB

sample sections were not completely separated after failure of the specimen. Images of the fracture surfaces are shown in Figure 54. These images show the increased surface roughness of KGPMB samples that resulted from the crack deflection caused by the minibars. The comparatively smooth surface of the KGPF samples shows that the fibers were less effective barriers to crack propagation throughout the sample.

The smaller specimens were useful in determining statistically accurate properties and for comparison of specimen size effects. A Weibull parameterization of the flexure performance of 27.9 mm x 27.9 mm x 152.4 mm specimens is presented as Figure 55 with summary statistics tabulated with reference values in Table 5. The linear fit against KGPF results again exhibited a low R-squared value, giving further evidence of multiple-flaw populations.

The ultimate flexure strengths of KGPF and KGPMB composite systems were 20% and 59% higher than that of the pure potassium geopolymer, respectively. The Weibull modulus was 16% lower than the unreinforced geopolymer phase for KGPF. This suggests that both reinforcement options improved the distribution of flexural stresses relative to the unreinforced geopolymer.

Ribero reported flexural strengths several times what were achieved here using woven basalt and chopped basalt strand mat.[112] However, the results are not directly comparable because their reinforcements were included at much greater volume fractions, 30% and 21% for woven basalt and chopped strand mat, respectively. Additionally, the layup procedure required to incorporate mat reinforcements limits the specimen geometry and applications.

Shear strength

Shear testing was performed on 76 mm (w) x 56 mm (h) x 6 mm (t) V-notched samples according to ASTM D7078.[113] The loading configuration is shown in Figure 56. Empirical data is presented in Table 27 in the Appendix.

Stress profiles for KGPF samples (Figure 57) reached the ultimate shear stress without showing any signs of damage and then failing in a brittle fashion. The failure surface (Figure 58) confirms that samples were dominated by a single crack. Unobstructed cracks are typically either perfectly straight or at a 45-degree angle to the V-notch in these specimens, thus the curvature of the crack indicated that the fibers presented an obstacle to crack propagation.

The stress-strain profiles of minibar-reinforced samples were very jagged, indicating unsteady loading (tests were displacement-controlled), where stresses may have been redistributed between the matrix and reinforcement phases, and occasional drops in load, where flaws were opened or grew. This suggested a tolerance for multiple flaws before reaching the ultimate shear stress, which was confirmed by inspection of the failed specimen. Large strain values were achieved before ultimate failure and samples retained some load-bearing ability after failure.

Summary statistics are tabulated with reference values in Table 6. Gaussian statistics were used due to the availability of reference data. The two basalt-reinforced systems showed similar average ultimate shear strength and standard deviations. Reference values for the shear strength for pure geopolymer was not available. Both samples exhibited higher mean strengths and greater variance than concrete and a much lower strength and smaller variance than hot-pressed silicon carbide samples.

Fracture toughness

Bar specimens of 27.9 mm x 27.9 mm x 152.4 mm (1 in x 1 in x 6 in) were prepared according to ASTM C1421.[114] After casting and drying the specimens, a 3 mm-thick, diamond-tipped circular saw blade was used to cut a notch approximately 4 mm deep straight across the short dimension, in the middle of one of the rectangular sides of each specimen. These notches were used as stress concentrators from which cracks were opened. The samples were loaded in three-point bending to open a pre-crack from the notch.

Once a suitable pre-crack had been formed and it was confirmed that no other damage was done to the sample, the load was removed, and the sample was treated with a dye penetrant from Magnaflux in Glenview, IL to facilitate identification and measurement of the pre-crack face. After allowing the dye penetrant to dry, samples were again subjected to 3-point bending to determine the force required to propagate the pre-crack further, the fracture toughness, K_I. Samples that met validation criteria set forth in the ASTM standard were then used to determine the critical fracture toughness, K_{IC}. The loading configuration is shown in Figure 59. Empirical data is presented in Table 28 in the Appendix.

Stress-strain profiles for fracture toughness tests of KGPF (Figure 60) exhibited qualitatively different behavior than in flexure tests. Namely, the retention of load-bearing ability after ultimate stress was uncharacteristic of KGPF samples in all the other tests we performed. Since the actual stress level was much lower than what was reached in flexural stress due to the presence of the pre-crack, this phenomenon can be reasonably explained by weak, short range matrix-fiber interactions. These interactions have been noted in the previous tests and the rough fracture surfaces in these tests confirmed this conclusion (Figure 61).

The results from the KGPMB samples confirmed that there were strong, long-range matrix-reinforcement interactions governing the strength and crack growth resistance in these samples. The jagged loading curves showed multiple crack propagation events. These consisted of propagation of the pre-crack as well as formation of several other cracks. While these did not contribute to the fracture toughness calculation, they did emphasize the obstacle that minibars continued to present to crack growth even after the initiation of a critical flaw.

A Weibull parameterization of the results is presented in Figure 62 and summary statistics with reference values are tabulated in Table 7. Given the intended purpose of the minibars, viz., a reinforcement added to toughen brittle materials, they have objectively been shown to accomplish this purpose.

The fracture toughness of KGPF and KGPMB composite systems were 936% and 4243% higher than that of the pure potassium geopolymer, respectively. The Weibull moduli were acceptably low, as compared to concrete and technical ceramics, though a direct comparison for pure geopolymer was unavailable. This suggests that both reinforcement options greatly improved the resistance to crack propagation in the samples relative to the unreinforced geopolymer.

The KGPF fracture toughness samples highlighted a recurrent theme in the other tests – the effect of multiple-flaw populations. Rigorously, this is understood as having a multimodal distribution of internal flaws that alternately drive mechanical properties at different stress levels. From the Weibull analysis, the point near 1 $MPa*m^{1/2}$ seems to be a critical point where the failure mechanism changed to being driven by one flaw population to another. This could be related to the plate-like failure sections seen in compression testing.

If the plates were formed by the bundling of fibers during synthesis, then there would be an inherent weakness along the plate boundaries. If the specimen were somehow restricted from failing at the plate boundaries, e.g. through size constraints or the load orientation, then failure would only occur once the stress was high enough to cause failure through the plate. Further testing is required to probe the cause of this anomaly in the strength.

Comparison of Reinforcement Performance

The minibar-reinforced geopolymer samples outperformed the fiber-reinforced samples in every test we performed. The geometry of the minibars appears to substantially improve mechanical properties of composites over the chopped fibers. To discern between the active mechanisms responsible for this increase, we examined post-failure samples under scanning electron microscopy.

Magnified failure surfaces of KPGF and KGPMB samples are shown in Figure 63 and Figure 64, respectively. Both systems exhibit both fiber pullout and failure of the reinforcement phase, so it is difficult to discern whether one of these is responsible for the generally higher values of the mechanical properties of KGPMB samples. Given this, we searched for an additional explanation in the processing methods.

Figure 65 shows the chopped basalt fibers before processing. The size distribution was unimodal with a tight distribution around the manufacturer's specified length of 25mm. A second set of fibers were processed as described in the Sample Preparation section of this chapter and then washed to remove the geopolymer matrix phase. An image of these fibers is shown in Figure 66 with a size distribution histogram. The image shows that the average fiber length was drastically reduced, and the variance was heavily increased after processing. This could help

explain the difference in the mechanical properties observed between the KGPF and KGPMB samples.

For future extension of this work, it would be desirable to find a different mixing technique to incorporate the fibers since the damage suffered by high shear mixing could be detrimental to the mechanical properties of the composite systems.

Conclusions

In this chapter, we examined the mechanical performance of reinforced geopolymer samples. We demonstrated that a novel geometry of reinforcement, the minibar, is superior to chopped fiber reinforcements in compression, flexure, shear, and fracture toughness.

We presented evidence that both reinforcement geometries induce fiber pullout interactions with the matrix and generally outperformed unreinforced geopolymer specimens. Minibar-reinforced samples also exhibited extensive toughening compared to both the fiber-reinforced samples and the classically brittle pure geopolymer. Therefore, the minibar should find a breadth of practical application in the industrial implementation of geopolymers.

Figures

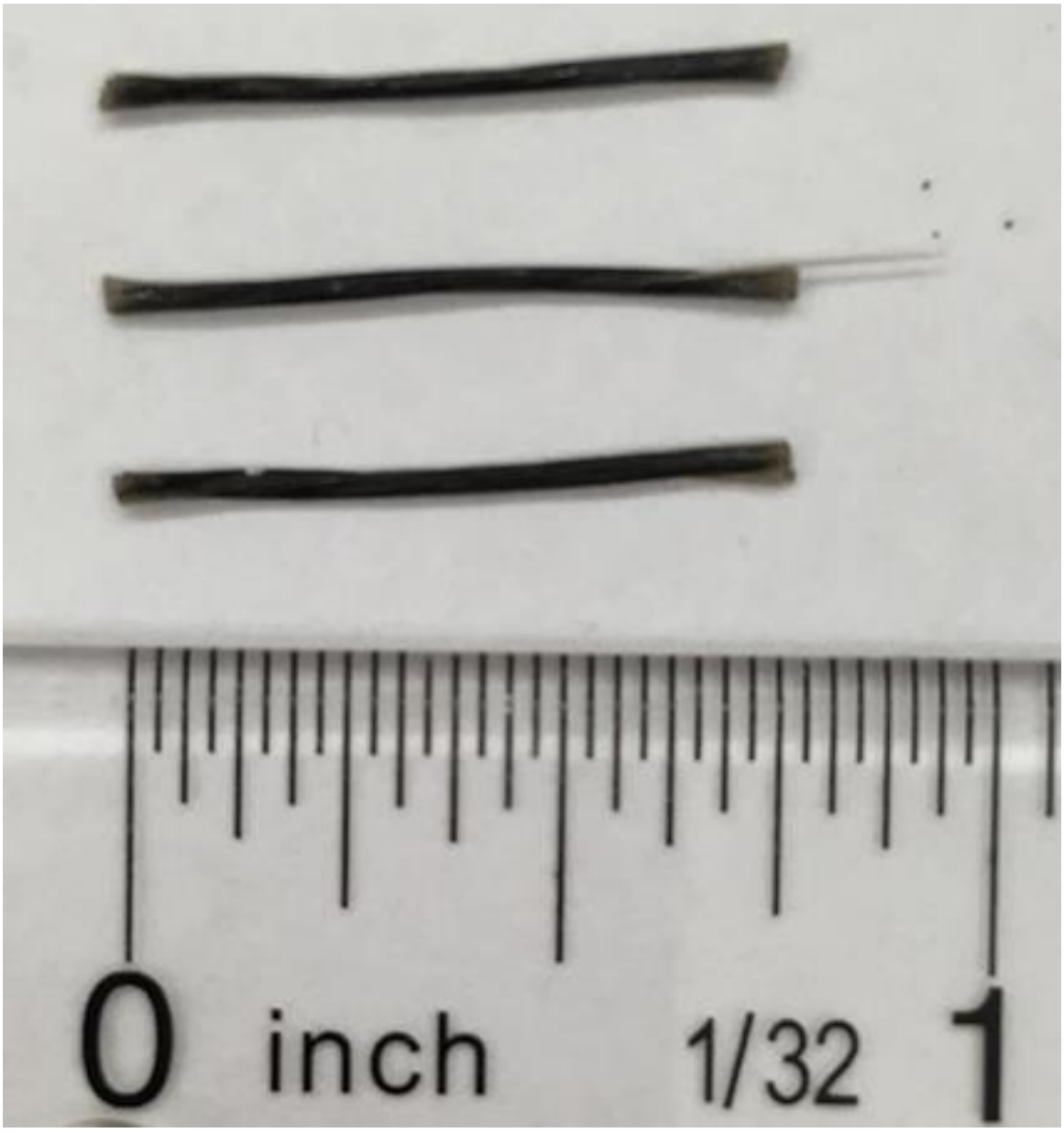

Figure 44 – Image of basalt minibars showing twist along the length and paddled ends.

Figure 45 – 100 Liter IKA stand mixer with high-shear attachment and dual mixing modes (high speed and high torque).

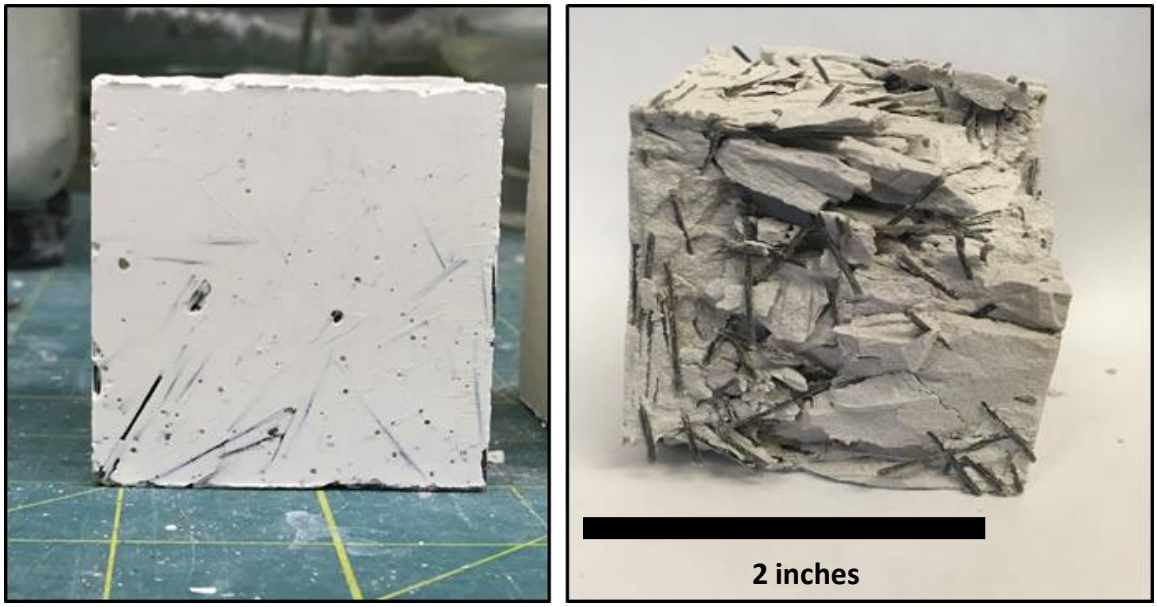

Figure 46 - Geopolymer viscosity test samples. (Left) pure geopolymer with 10 weight percent minibars added and (right) geopolymers with 70 weight percent 50-micron chamotte particles and 10 weight percent minibars after compressive testing. The improvement in the vertical homogeneity and variety of minibar orientation in the sample with chamotte added is due to the increased viscosity of the geopolymer with higher solids content.

Figure 47 – Testing configuration for compressive loading tests

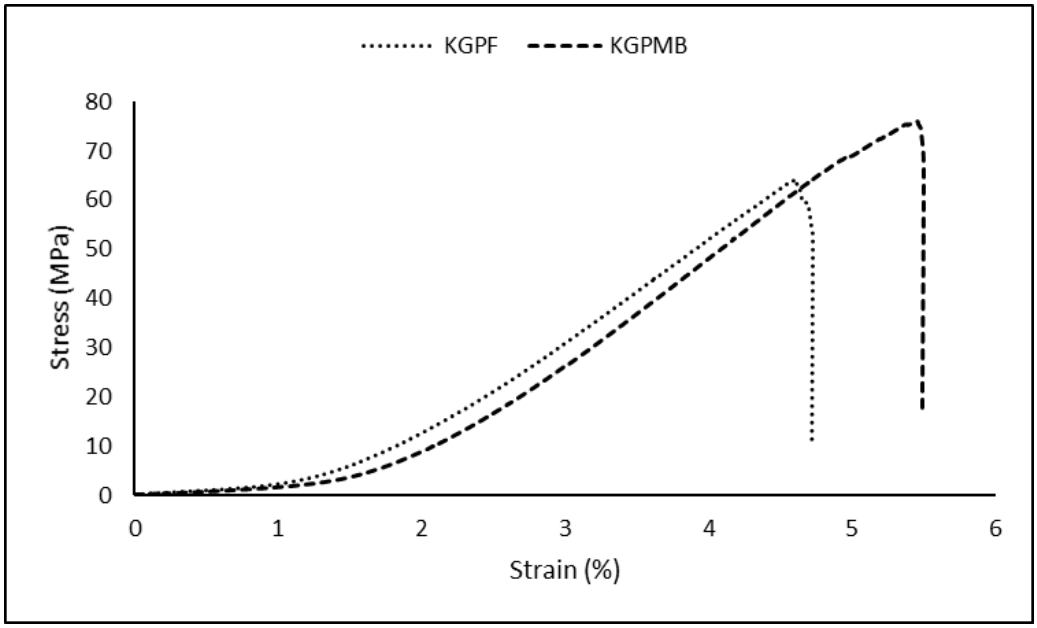

Figure 48 - Representative compressive strength characterization results for KGPF and KGPMB samples

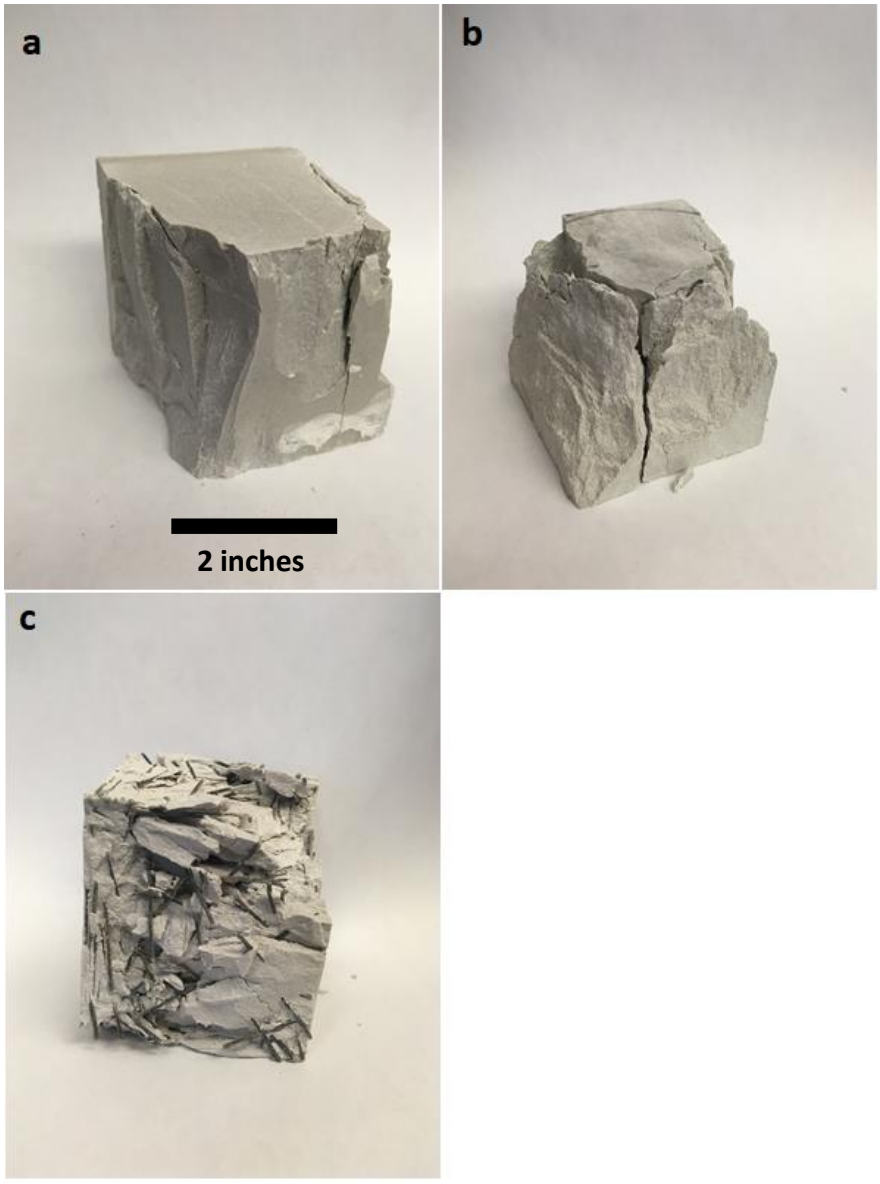

Figure 49 - Compressive fracture surfaces of geopolymer with (a) 70 wt% chamotte, (b) 10 wt% basalt fibers, and (c) 70 wt% chamotte and 10 wt% minibars.

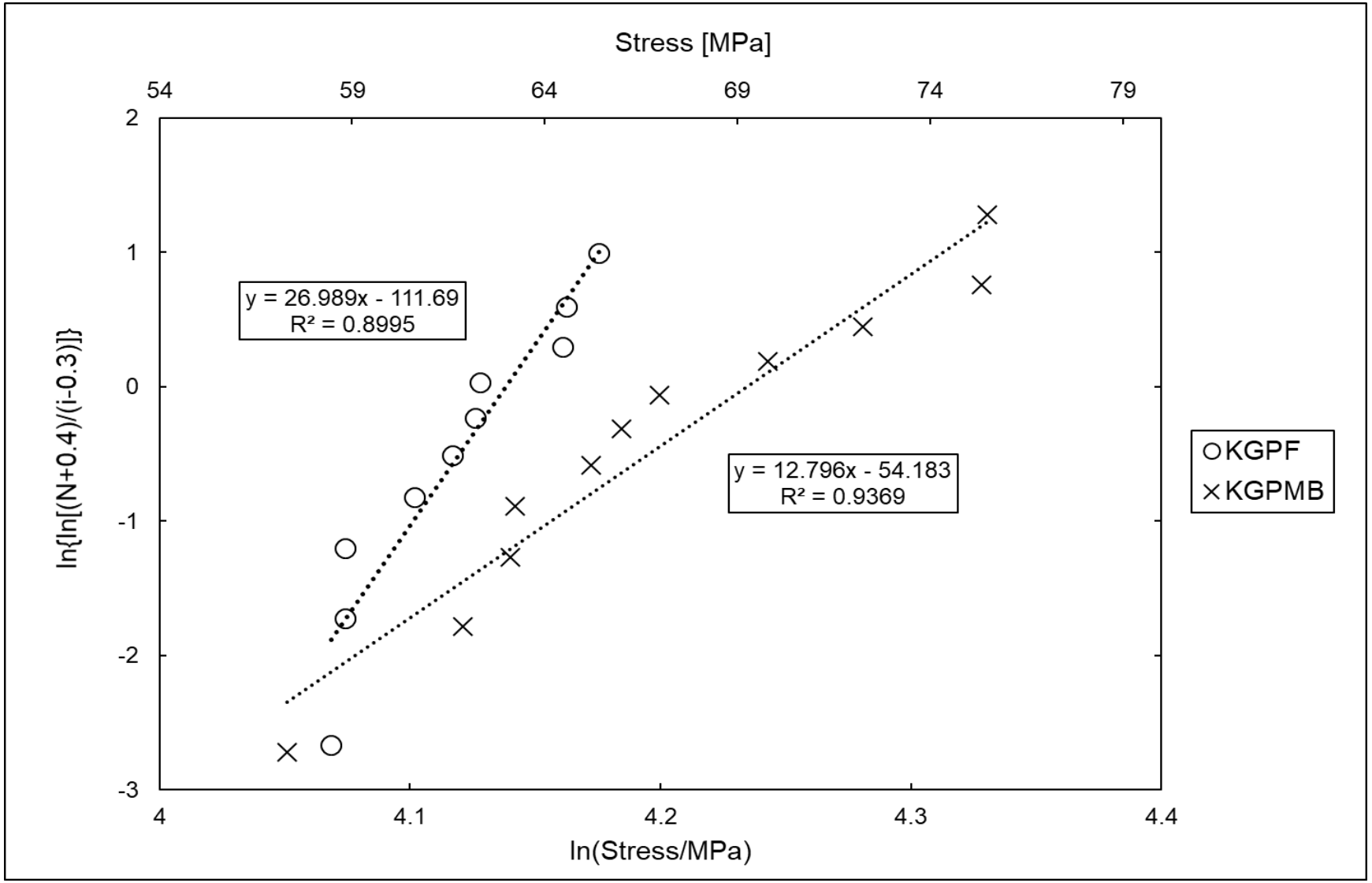

Figure 50 - Weibull analysis of compressive strength characterization testing.

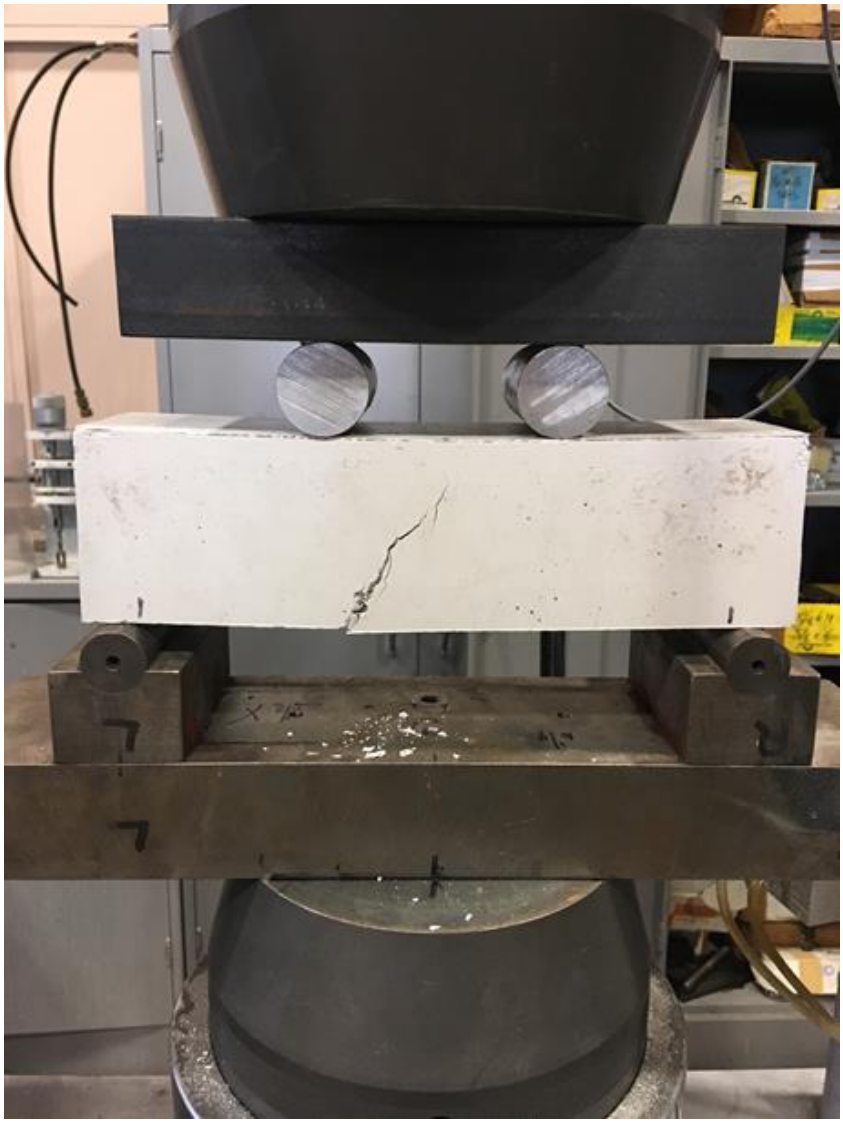

Figure 51 – Testing configuration for 4-point bending tests

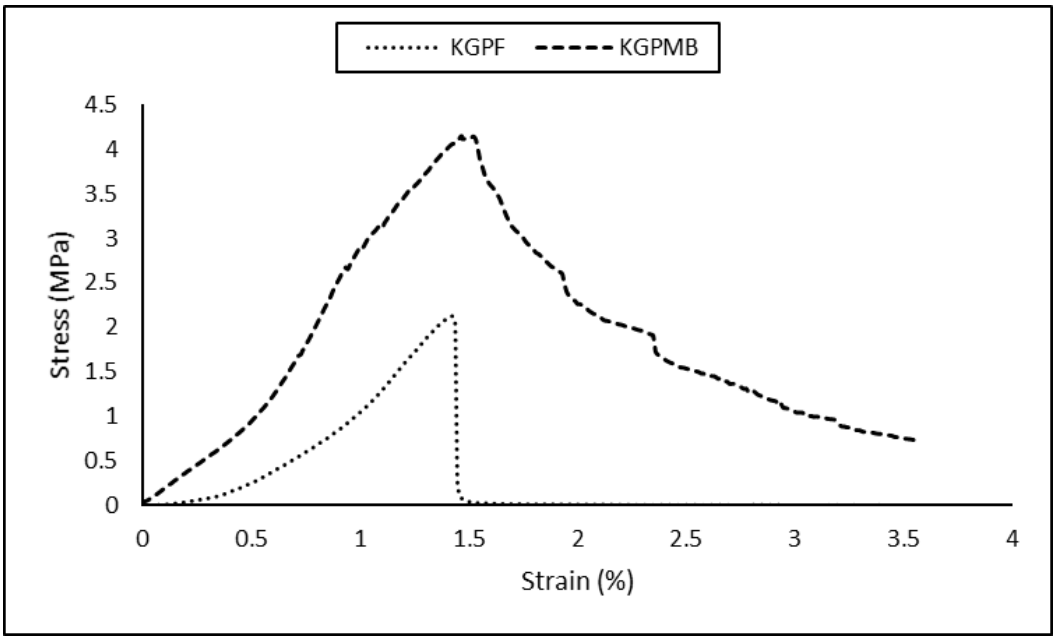

Figure 52 - Representative flexure strength characterization results for KGPF and KGMB samples

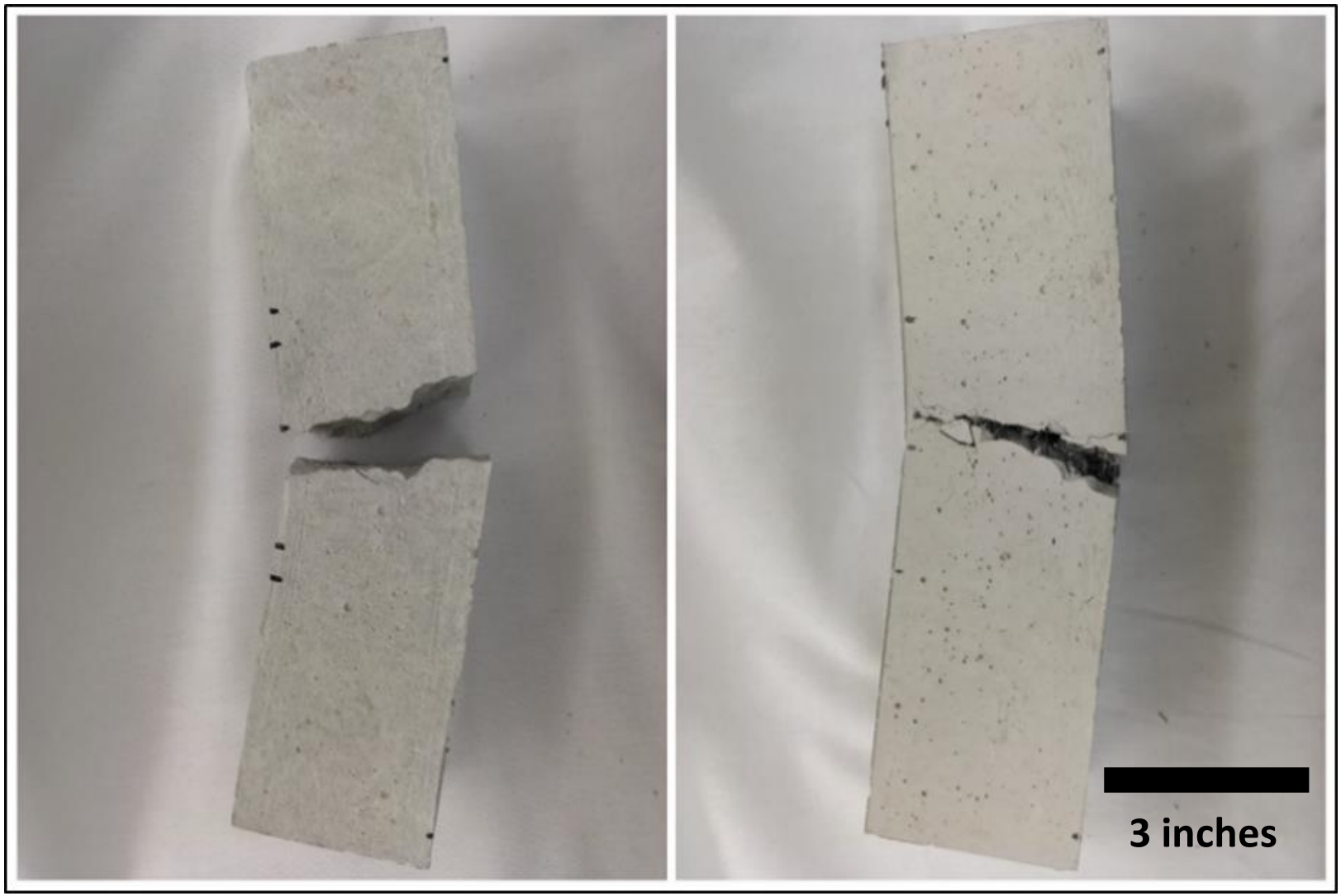

Figure 53 - (Left) KGPF and (right) KGPMB flexural samples after being subjected to 4-point bending

Figure 54 - Fracture surfaces for (top) KGPF and (bottom) KGPMB. Tension surfaces are centered in the images, while compressive surfaces are on the edges.

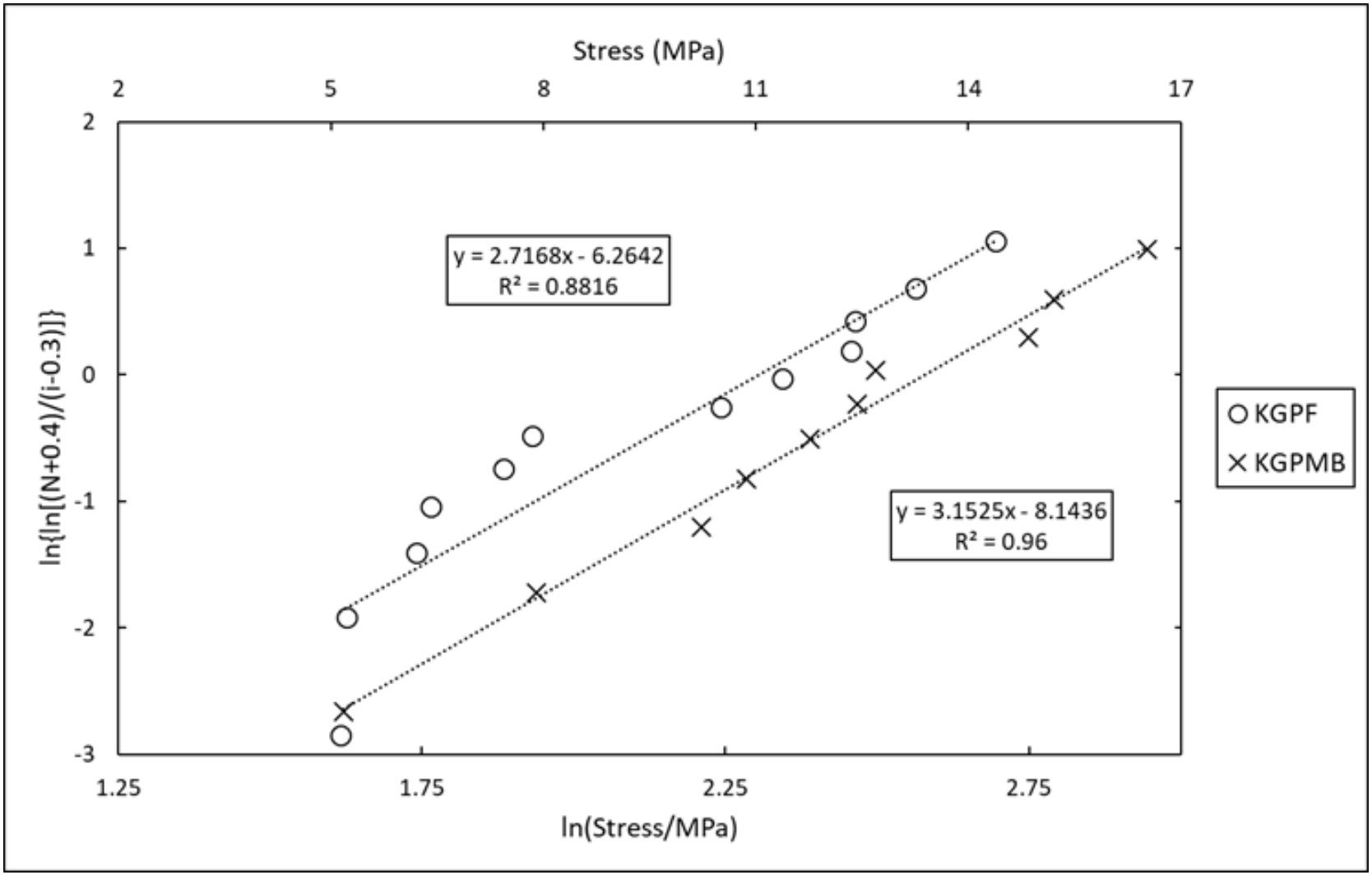

Figure 55 - Weibull analysis of flexural strength characterization testing

Figure 56 – Testing configuration for shear loading tests

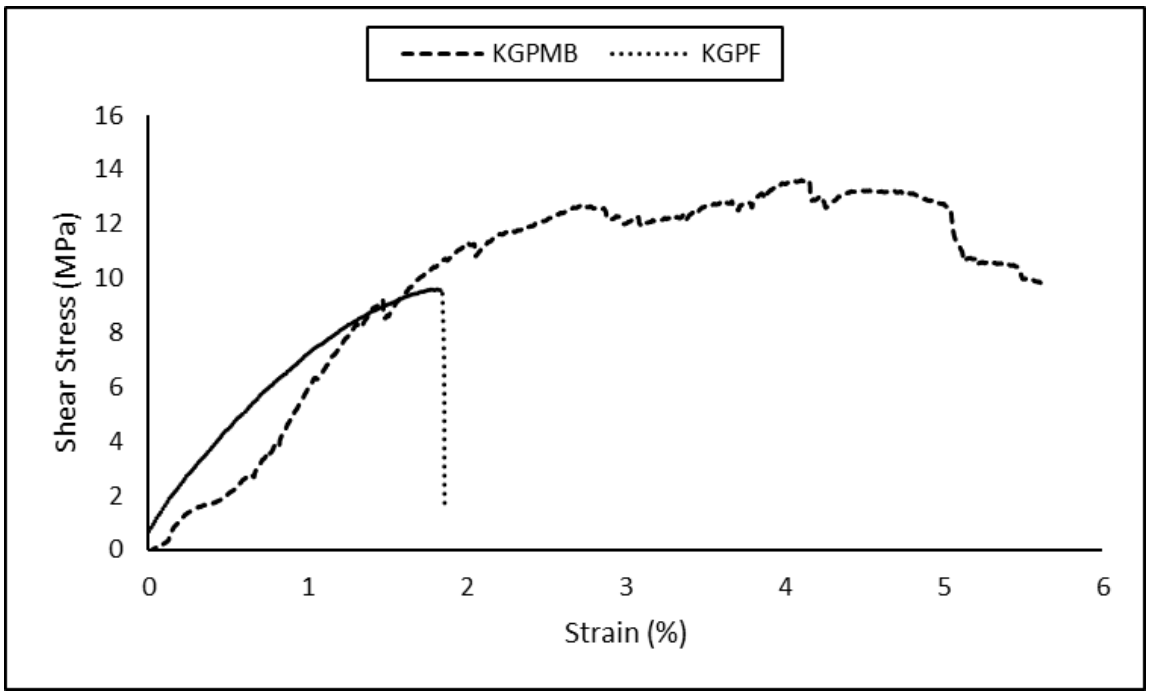

Figure 57 - Representative shear strength characterization results for KGPF and KGPMB samples

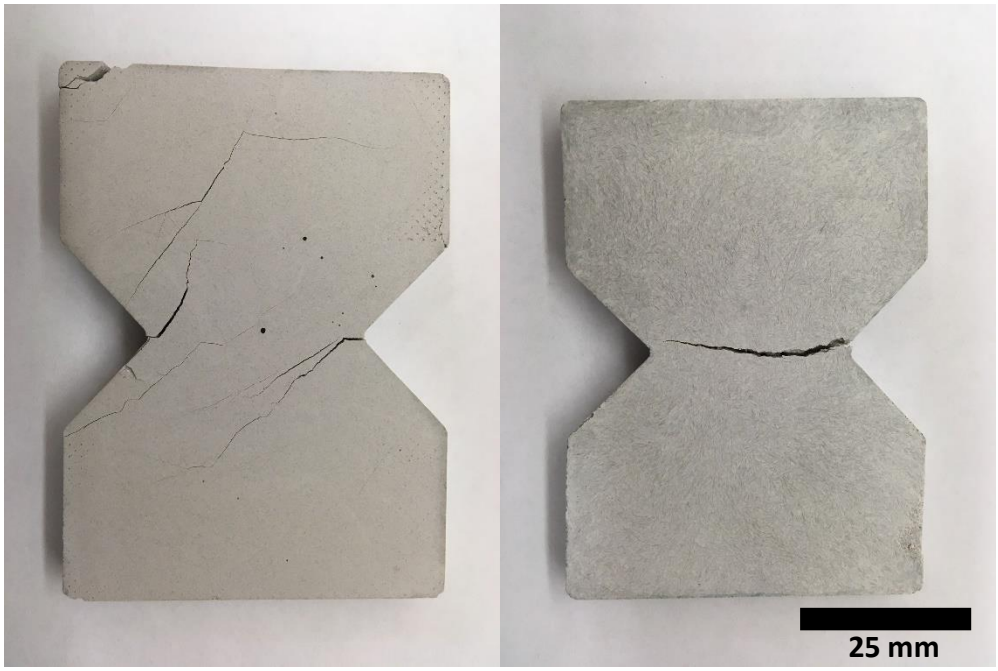

Figure 58 - Shear specimens after failure (left) KGPMB and (right) KGPF

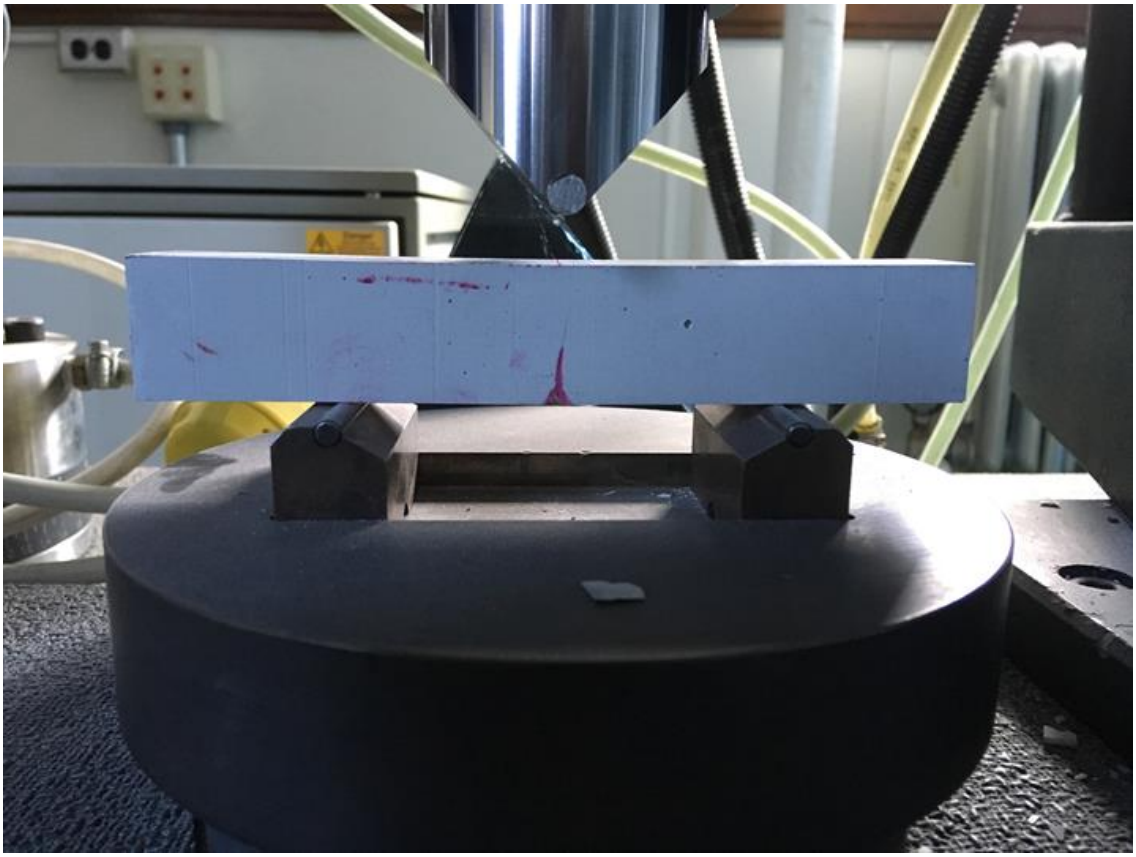

Figure 59 – Testing configuration for fracture toughness tests

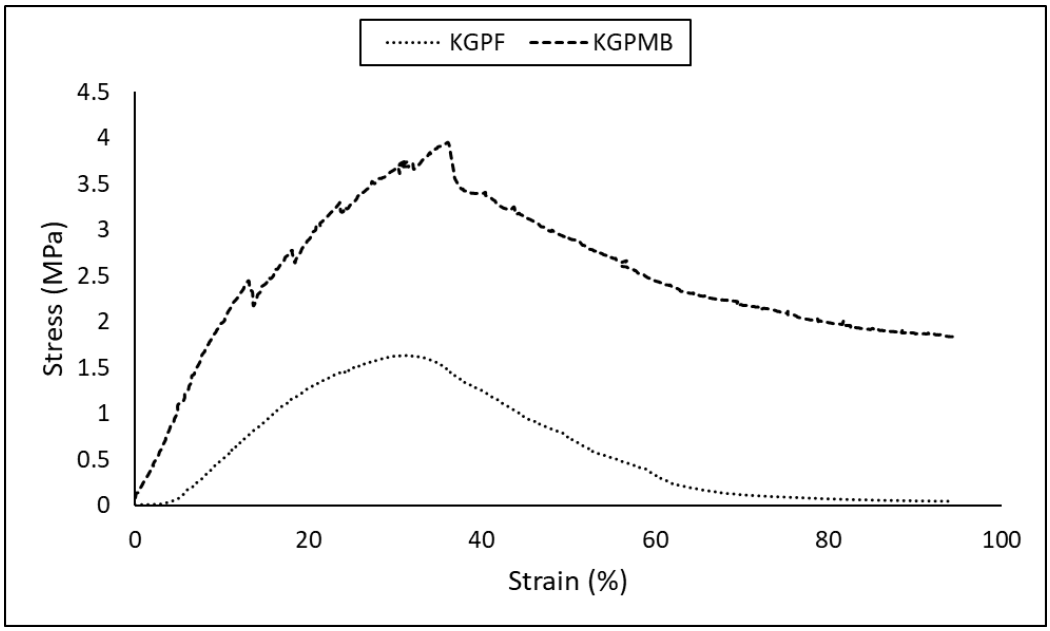

Figure 60 – Representative fracture toughness characterization results of KGPF and KGPMB samples

Figure 61 – Fracture surfaces from samples after fracture toughness testing (left) KGPF and (right) KGPMB

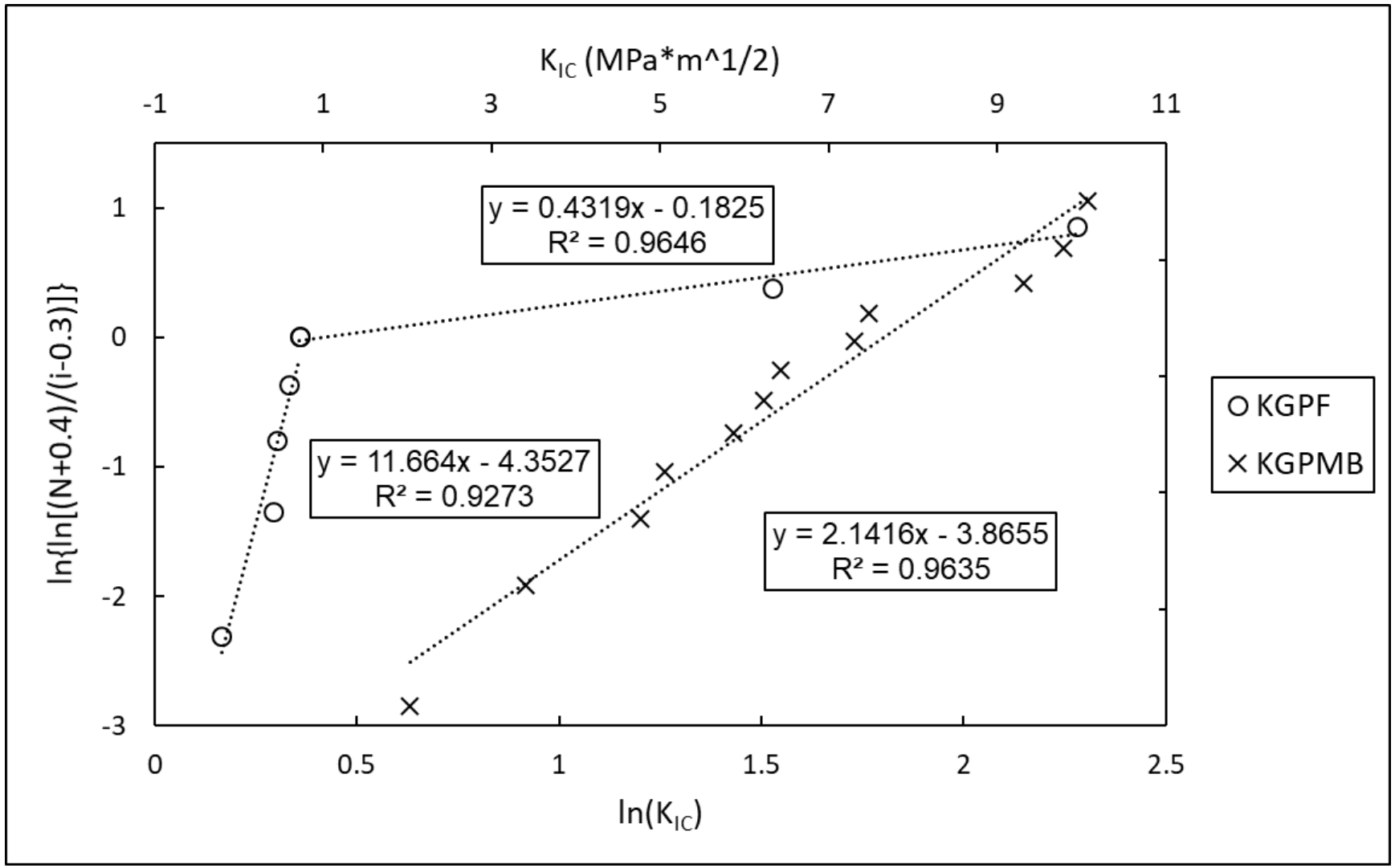

Figure 62 – Weibull parameterization analysis of fracture toughness results in KGPF and KGPMB samples

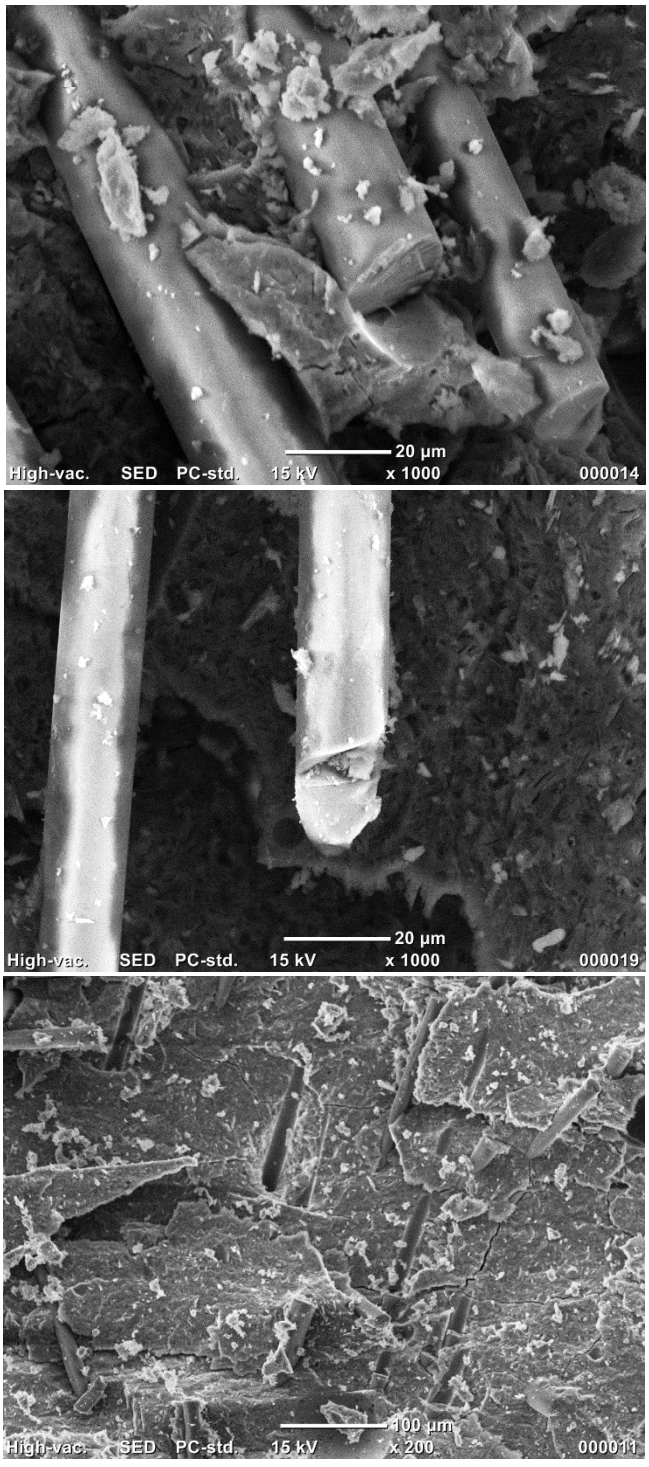

Figure 63 – SEM micrographs of fracture surfaces from KGPF samples exhibiting symptoms of multiple failure mechanisms. (Top) Mixed-mode fiber cleavage and fiber pullout. (Middle) Fiber failure. (Bottom) Fiber pullout.

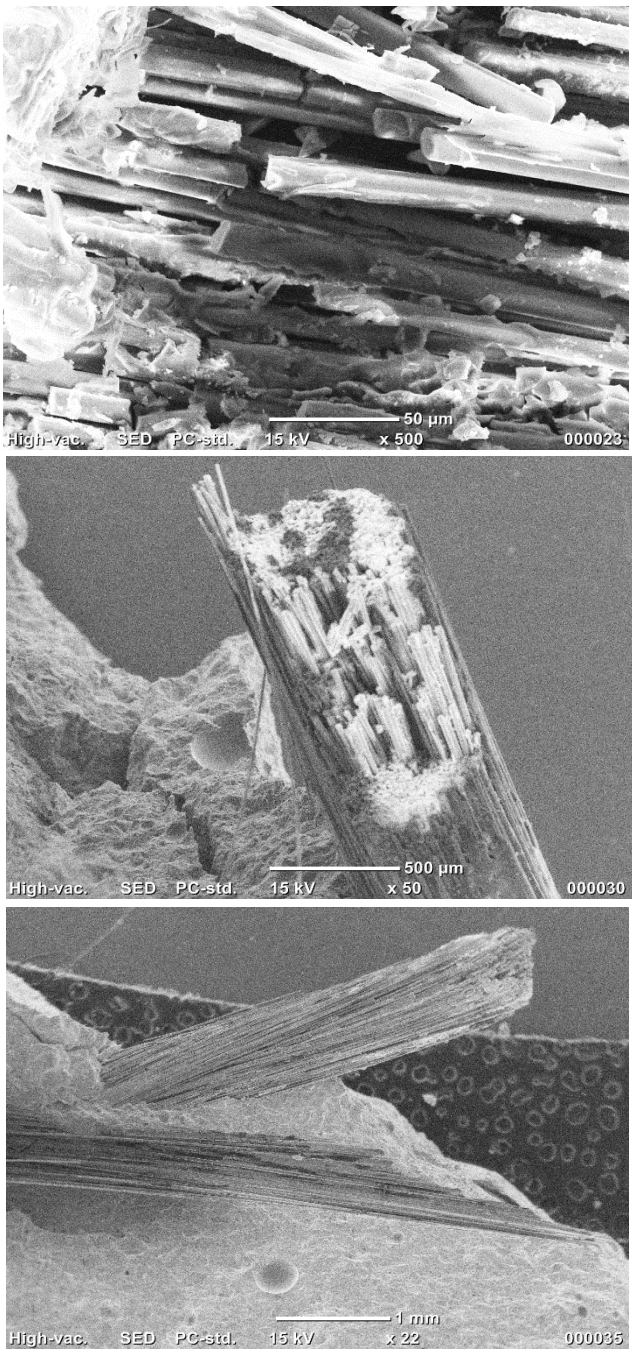

Figure 64 – SEM micrographs of KGPMB samples exhibiting symptoms of multiple failure mechanisms. (Top) A single minibar bundle with a mixture of intact and cleaved fibers. (Middle) Another partially cleaved minibar. (Bottom) Pullout traces in the matrix phase.

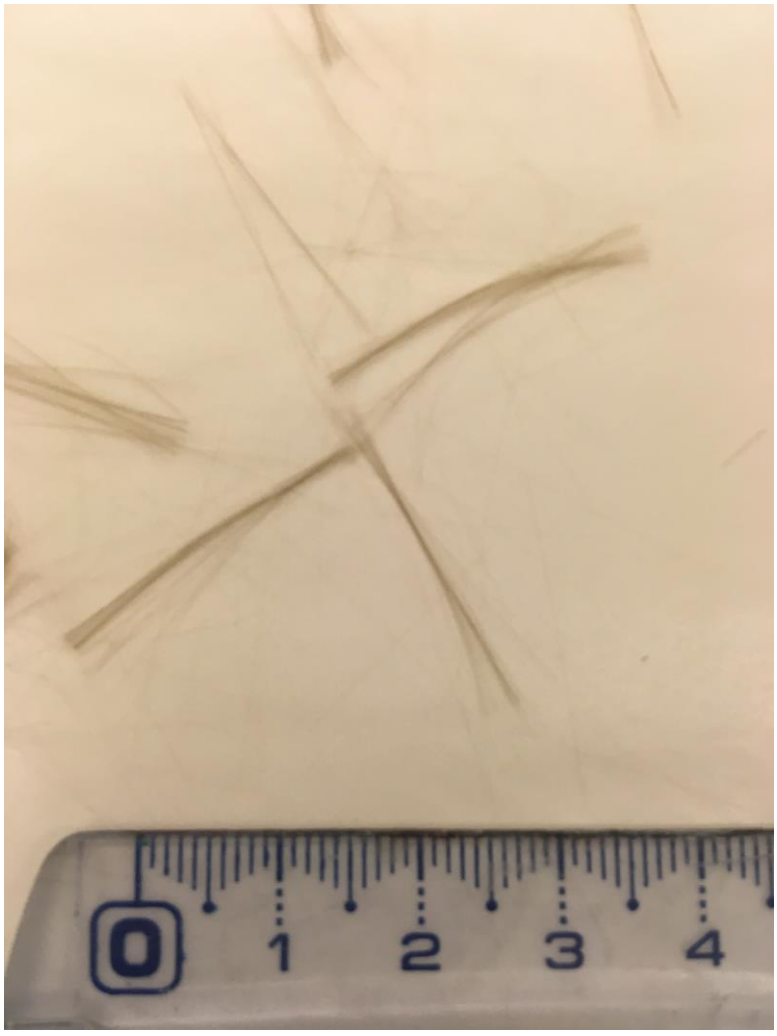

Figure 65 – Image of multiple basalt fibers as-received. All observed fibers were approximately 25mm in length.

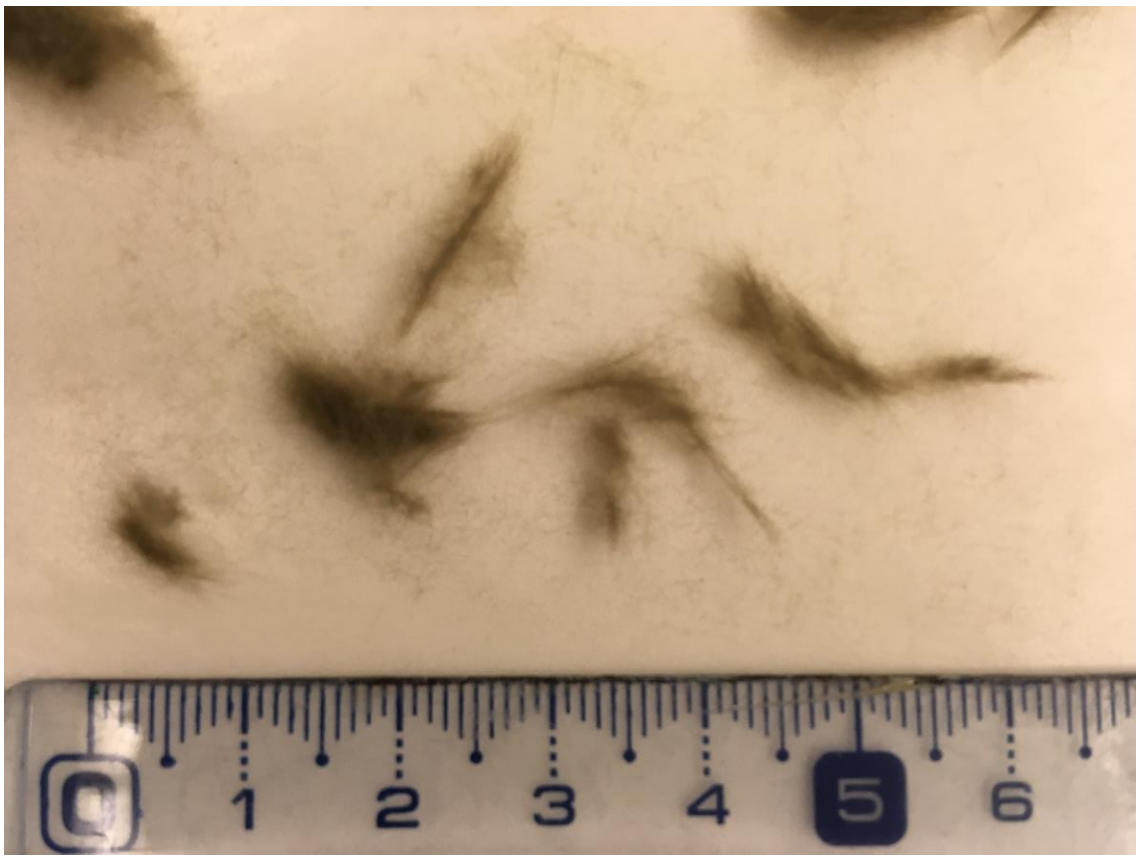

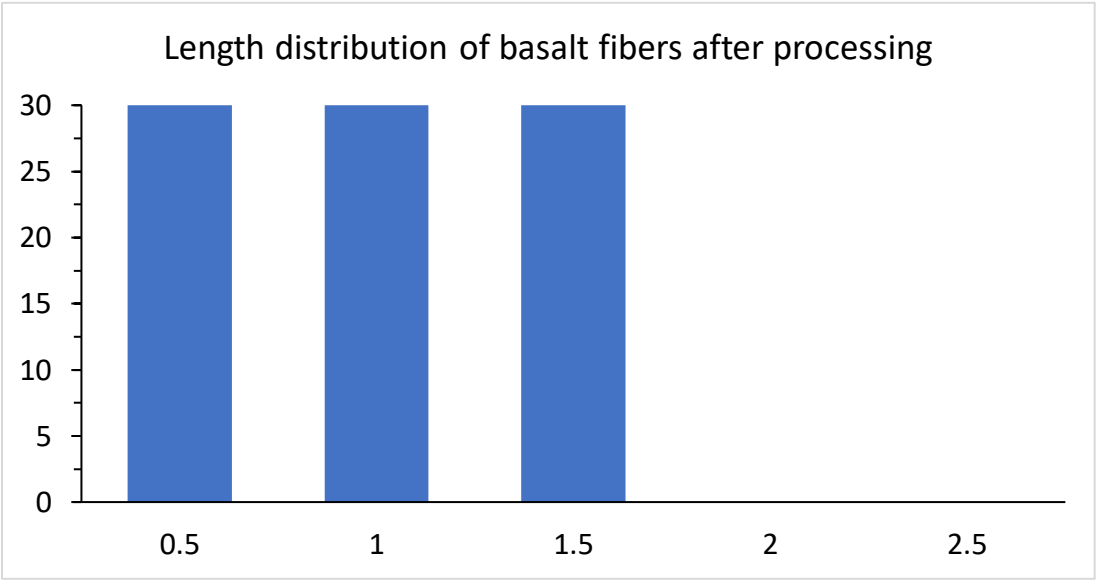

Figure 66 – (Top) Image of basalt fibers after processing and washing. Almost no fibers were detected of the length near the as-received specification. Many were too small to measure. (Bottom) Measured length distribution of fibers after processing. 30 was the maximum number counted.

Tables

Table 4 – Summary statistics for compression strength measured according to ASTM C109

	Characteristic strength (σ_c, MPa)	**Weibull Modulus**
KGPF	62.7	27.0
KGPMB	69.0	12.8
Pure KGP[115]	107.0	9.0
Concrete[116]	51.4	9.1
Yttria-stabilized zirconia[117]	110.7	1.6

Table 5 – Summary statistics for flexural strength measured according to ASTM C1161

	Characteristic strength (σ_f, MPa)	**Modulus (m)**
KGPF	10.0	2.7
KGPMB	13.2	3.2
Pure KGP[115]	8.3	3.2
Woven Basalt-reinforced GP[112]	45.2	5.1
Chopped Basalt Strand-reinforced GP[112]	31.7	8
Concrete[118]	19.5	5.0
Alumina[119]	316	1.5

Table 6 – Summary statistics for shear strength measured according to ASTM D7078

	Mean strength (τ_0, MPa)	**Standard deviation (MPa)**
KGPF	7.54	1.66
KGPMB	8.19	2.20
Concrete[120]	3.10	0.30
Hot-pressed SiC[121]	74	20

Table 7 – Summary statistics for fracture toughness measured according to ASTM C1421

	Characteristic value (K_{IC}, MPa $*\sqrt{m}$)	**Modulus (m)**
KGPF	1.45	0.01
KGPMB	6.08	1.15
Pure KGP[115]	0.14	N/A
Concrete[122]	1.06	0.11
Silicon nitride[123]	5.60	0.50

CHAPTER 5 – SUGGESTIONS FOR FUTURE WORK

To quote Professor Kriven, “A good thesis answers one question and raises several more.” The work described in this thesis to identify, synthesize, and characterize a new class of candidate materials for EBC applications implies the potential utility of several related compounds.

As mentioned previously, the $Rb_xCs_{1-x}[AlSi_2O_6]$ system holds great potential for improving the high temperature capabilities of the $K_xCs_{1-x}[AlSi_2O_6]$ system and taking advantage of the geopolymer synthesis and tailorable thermal expansion

There is also significant potential in adjusting the ratios of the other components of the system. Related to the work presented in Chapter 3, we performed preliminary work to characterize the $Na_xK_{1-x}[AlSi_2O_6]$ and $Na_xK_{1-x}[AlSiO_4]$ systems. The $Na_xK_{1-x}[AlSi_2O_6]$ system was investigated as an extension of the 1:1:4 alkali aluminosilicates family.

As mentioned in Chapter 3, the sodium end member, analcime, $Na[AlSi_2O_6]\cdot H_2O$, is a hydrated phase. The evaporation of water on heating causes the framework to collapse and the analcime structure is lost. Heating to at least 800°C has been found necessary to crystallize these materials from the geopolymer phase. Candidate materials for EBC applications routinely face exposure to temperatures far in excess of this. Such heat treatments applied to samples of bulk composition $Na[AlSi_2O_6]$ instead produced $Na[AlSiO_4]$ + glassy phase SiO_2. These samples were not pursued for thermal expansion analysis due to uncertainties in chemistry arising from the presence of the glassy phase. This led to our preliminary investigation into the 1:1:2 system, $Na_xK_{1-x}[AlSiO_4]$, presented in Chapter 3.

Samples containing sodium exhibited multiple phases. Figure 67 shows results from the phase identification routine in Jade for both 1:1:4 and 1:1:2 bulk compositions. The diffraction pattern for the 1:1:4 system exhibits a large diffuse background peak associated with amorphous, glassy phase material. The pattern for the 1:1:2 system exhibits multiple phases.

We believe the issue with this system lies in the geopolymer chemistry of low-silica compounds. Studies on the reactivity of alkali silicate solutions with metakaolin indicate dependence of the reaction on silica content in the solution.[27] In 1:1:2 systems synthesized by reaction with metakaolin (Al_2O_3:SiO_2), no silica is added to the alkali hydroxide solution. This could influence the geopolymer formation in these systems and, therefore, the crystalline product recovered after heat treatment. The cation identity clearly plays a role in these reactions, as well, since kalsilite was successfully produced (as discussed in Chapter 3), but nepheline was an elusive target.

Examination of the nepheline-kalsilite-silica ($Na[AlSiO_4]$-$K[AlSiO_4]$-SiO_2) phase diagram (Figure 68) indicates a solid solution forming in the albite-orthoclase ($Na[AlSi_3O_8]$-$K[AlSi_3O_8]$).[124] These should be accessible through an appropriate geopolymer crystallization synthesis, though our attempts failed due to seizing of the alkali silicate solution before enough silica could be incorporated. The melting points of albite and orthoclase are between 1100-1200°C.[125]

Finally, it is of great importance for the potential of any of these materials as EBCs to undergo further investigations into their performance *in situ*. Candidate materials for EBC applications are thoroughly studied for their chemical activity with respect to silica and calcium-magnesium aluminosilicates (CMAS) at high temperatures since these are critical to their performance. It is also important to understand the microstructure development in the plasma

spray deposition process and during operation, where environmental demands are some of the most extreme for any contemporary material system.

Figures

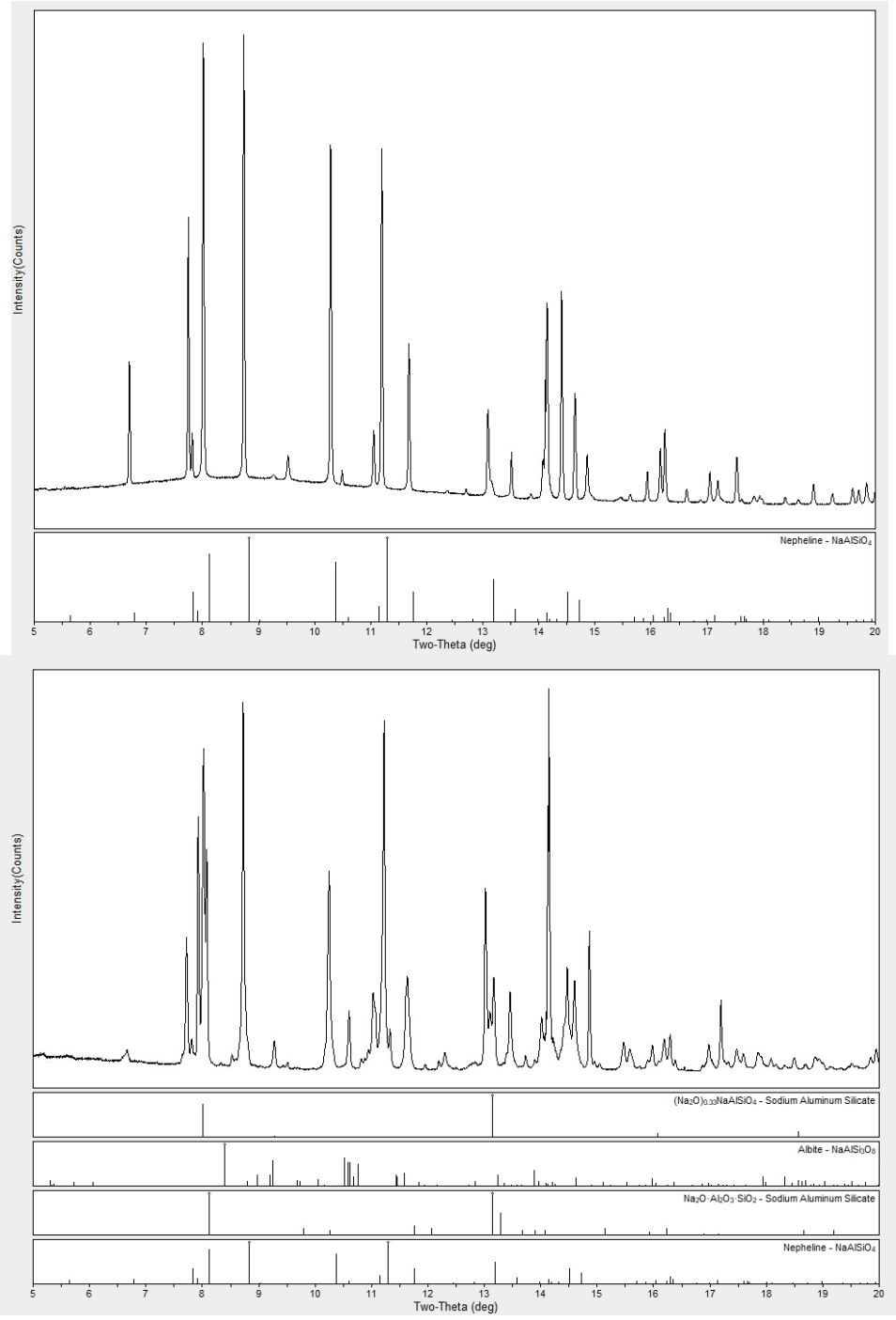

Figure 67 – Phase identification for the sodium-based phases of bulk composition 1:1:4, $Na[AlSi_2O_6]$ (top) and 1:1:2, $Na[AlSiO_4]$ (bottom).

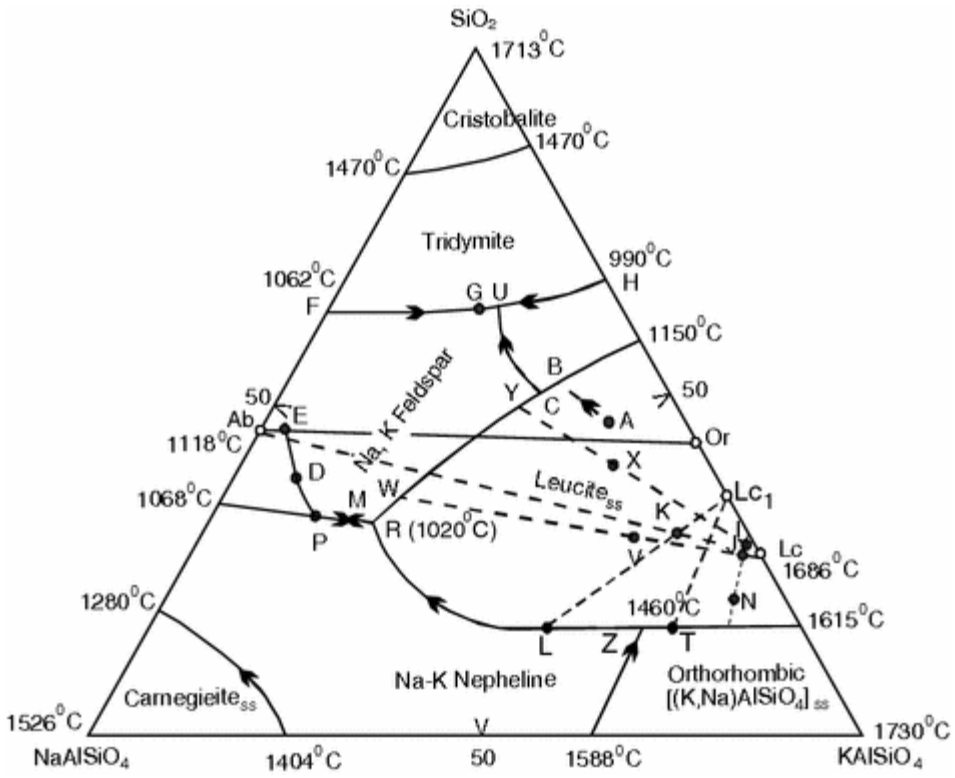

Figure 68 – The phase diagram of the nepheline-kalsilite-silica system.[124]

REFERENCES

[1] N. P. Padture, "Environmental degradation of high-temperature protective coatings for ceramic-matrix composites in gas-turbine engines," *Mater. Degrad.*, vol. 3, no. 1, 2019.

[2] N. P. Padture, "Advanced structural ceramics in aerospace propulsion," *Nat. Mater.*, vol. 15, no. 8, pp. 804–809, 2016.

[3] R. C. Robinson and J. L. Smialek, "SiC recession caused by SiO2 scale volatility under combustion conditions: I. Experimental results and empirical model," *J. Am. Ceram. Soc.*, vol. 82, no. 7, pp. 1817–1825, 1999.

[4] K. L. More, P. F. Tortorelli, M. K. Ferber, and J. R. Keiser, "Observations of accelerated silicon carbide recession by oxidation at high water-vapor pressures," *J. Am. Ceram. Soc.*, vol. 83, no. 1, pp. 211–13, Jan. 2000.

[5] E. J. Opila and R. E. Hann, "Paralinear oxidation of CVD SiC in water vapor," *J. Am. Ceram. Soc.*, vol. 80, no. 1, pp. 197–205, 1997.

[6] N. S. Jacobson, "Corrosion of silicon-based ceramics in combustion environments," *J. Am. Ceram. Soc.*, vol. 76, no. 1, pp. 3–28, 1993.

[7] G. C. C. Costa and N. S. Jacobson, "Mass spectrometric measurements of the silica activity in the Yb2O3-SiO2 system and implications to assess the degradation of silicate-based coatings in combustion environments," *J. Eur. Ceram. Soc.*, vol. 35, no. 15, pp. 4259–4267, 2015.

[8] K. Von Niessen and M. Gindrat, "Plasma spray-PVD: A new thermal spray process to deposit out of the vapor phase," *Journal of Thermal Spray Technology*, vol. 20, no. 4. pp. 736–743, 2011.

[9] W. M. Kriven, J. L. Bell, and M. Gordon, "Microstructure and microchemistry of fully-reacted geopolymers and geopolymer matrix composites," *Ceram. Trans.*, vol. 153, pp. 227–250, Apr. 2004.

[10] V. F. F. Barbosa, K. J. D. MacKenzie, and C. Thaumaturgo, "Synthesis and characterisation of materials based on inorganic polymers of alumina and silica: Sodium polysialate polymers," *Int. J. Inorg. Mater.*, vol. 2, no. 4, pp. 309–317, 2000.

[11] V. F. F. Barbosa and K. J. D. Mackenzie, "Synthesis and thermal behavior of potassium sialate geopolymers," *Mater. Lett.*, vol. 57, pp. 1477–1482, 2003.

[12] V. F. F. Barbosa and K. J. D. MacKenzie, "Thermal behaviour of inorganic geopolymers and composites derived from sodium polysialate," *Mater. Res. Bull.*, vol. 38, no. 2, pp. 319–331, 2003.

[13] J. Davidovits, *Geopolymer Chemistry and Applications*, 4th ed. Saint-Quentin, France: Institut Géopolymère, 2015.

[14] H. Rahier, W. Simons, B. Van Mele, and M. Biesemans, "Low-temperature synthesized aluminosilicate glasses: Part III Influence of the composition of the silicate solution on production, structure and properties," *J. Mater. Sci.*, vol. 32, no. 9, pp. 2237–2247, 1997.

[15] P. Duxson, G. C. Lukey, and J. S. J. van Deventer, “The thermal evolution of metakaolin geopolymers: Part 2 - Phase stability and structural development,” *J. Non. Cryst. Solids*, vol. 353, no. 22–23, pp. 2186–2200, 2007.

[16] B. O. Mysen and P. Richet, *Developments in Geochemistry Volume 10*. Elsevier, 2005.

[17] H. Rahier, J. Wastiels, M. Biesemans, R. Willlem, G. Van Assche, and B. Van Mele, “Reaction mechanism, kinetics and high temperature transformations of geopolymers,” *J. Mater. Sci.*, vol. 42, no. 9, pp. 2982–2996, 2007.

[18] J. Yuan *et al.*, “Thermal evolution of lithium ion substituted cesium-based geopolymer under high temperature treatment, Part I: Effects of holding temperature,” *Ceram. Int.*, vol. 44, no. 9, pp. 10047–10054, Jun. 2018.

[19] B. Zhang, K. J. D. MacKenzie, and I. W. M. Brown, “Crystalline phase formation in metakaolinite geopolymers activated with NaOH and sodium silicate,” *J. Mater. Sci.*, vol. 44, no. 17, pp. 4668–4676, 2009.

[20] P. E. Driemeyer, W. M. Kriven, J. L. Bell, R. P. Haggerty, P. Sarin, and P. J. Chupas, “X-Ray pair distribution function analysis of a metakaolin-based, KAlSi2O6·5.5H2O inorganic polymer (geopolymer),” *J. Mater. Chem.*, vol. 18, no. 48, p. 5974, 2008.

[21] J. L. Bell *et al.*, “Atomic structure of a cesium aluminosilicate geopolymer: A pair distribution function study,” *Chem. Mater.*, vol. 20, no. 14, pp. 4768–4776, 2008.

[22] C. E. White, J. L. Provis, T. Proffen, and J. S. J. Van Deventerz, “The effects of temperature on the local structure of metakaolin-based geopolymer binder: A neutron pair distribution function investigation,” *J. Am. Ceram. Soc.*, vol. 93, no. 10, pp. 3486–3492, 2010.

[23] P. S. Singh, T. Bastow, and M. Trigg, “Structural studies of geopolymers by 29Si and 27Al MAS-NMR,” *J. Mater. Sci.*, vol. 40, no. 15, pp. 3951–3961, 2005.

[24] P. Duxson, J. L. Provis, G. C. Lukey, F. Separovic, and J. S. J. Van Deventer, “29Si NMR study of structural ordering in aluminosilicate geopolymer gels,” *Langmuir*, vol. 21, no. 7, pp. 3028–3036, 2005.

[25] P. S. Singh, M. Trigg, I. Burgar, and T. Bastow, “Geopolymer formation processes at room temperature studied by 29Si and 27Al MAS-NMR,” *Mater. Sci. Eng. A*, vol. 396, no. 1–2, pp. 392–402, 2005.

[26] W. Loewenstein, “The distribution of aluminum in the tetrahedra of silicates and aluminates.,” *Am. Mineral.*, vol. 39, no. 1–2, pp. 92–96, 1954.

[27] P. Duxson, G. C. Lukey, and J. S. J. Van Deventer, “Physical evolution of Na-geopolymer derived from metakaolin up to 1000°C,” *J. Mater. Sci.*, vol. 42, no. 9, pp. 3044–3054, 2007.

[28] J. L. Bell, P. E. Driemeyer, and W. M. Kriven, “Formation of ceramics from metakaolin-based geopolymers. Part II: K-based geopolymer,” *J. Am. Ceram. Soc.*, vol. 92, no. 3, pp. 607–615, 2009.

[29] J. L. Bell, P. E. Driemeyer, and W. M. Kriven, “Formation of ceramics from metakaolin-based geopolymers. Part I: Cs-based geopolymer,” *J. Am. Ceram. Soc.*, vol. 92, no. 3, pp. 1–8, 2009.

[30] P. He, D. Jia, M. Wang, and Y. Zhou, “Effect of cesium substitution on the thermal evolution and ceramics formation of potassium-based geopolymer,” *Ceram. Int.*, vol. 36, pp. 2395–2400, 2010.

[31] D. C. Palmer, M. T. Dove, R. M. Ibberson, and B. M. Powell, “Structural behavior, crystal chemistry, and phase transitions in substituted leucite: High-resolution neutron powder diffraction studies,” *Am. Mineral.*, vol. 82, no. 1–2, pp. 16–29, 1997.

[32] A. Kloužková, M. Mrázová, and M. Kohoutková, “Synthesis of partially stabilized leucite,” *J. Phys. Chem. Solids*, vol. 68, no. 5–6, pp. 1207–1210, May 2007.

[33] M. H. Nguyen, S. J. Lee, and W. M. Kriven, “Synthesis of oxide powders by way of a polymeric steric entrapment precursor route,” *J. Mater. Res.*, vol. 14, no. 8, pp. 3417–3426, 1999.

[34] J. Weitkamp, “Zeolites and catalysis,” *Solid State Ionics*, vol. 131, no. 1, pp. 175–188, 2000.

[35] W. H. Taylor, “The nature and properties of aluminosilicate framework structures,” *Proc. R. Soc. London. Ser. A*, vol. 145, no. 854, pp. 80–103, 1934.

[36] R. J. Angel, N. L. Ross, and J. Zhao, “The compression of framework minerals: Beyond rigid polyhedra,” *Eur. J. Mineral.*, vol. 17, no. 2, pp. 193–199, 2005.

[37] S. A. Wells, K. Ming Leung, P. P. Edwards, M. G. Tucker, and A. Sartbaeva, “Defining the flexibility window in ordered aluminosilicate zeolites,” *R. Soc. Open Sci.*, vol. 4, no. 9, 2017.

[38] J. Als-Nielsen and D. McMorrow, *Elements of Modern X-ray Physics: Second Edition*. John Wiley and Sons, 2011.

[39] J. K. Cockcroft, “Generation of X-rays,” 2006. [Online]. Available: http://pd.chem.ucl.ac.uk/pdnn/inst1/xrays.htm.

[40] F. R. Elder, A. M. Gurewitsch, R. V. Langmuir, and H. C. Pollock, “Radiation from electrons in a synchrotron,” *Physical Review*, vol. 71, no. 11. pp. 829–830, 1947.

[41] S. R. Aubuchon, “Dilatometer Technology,” *Ceramic Industry*, 2012. [Online]. Available: https://www.ceramicindustry.com/articles/92598-dilatometer-technology.

[42] J. S. O. Evans and I. R. Evans, “Beyond classical applications of powder diffraction,” *Chem. Soc. Rev.*, vol. 33, no. 8, pp. 539–547, 2004.

[43] J. L. Provis, P. Duxson, G. C. Lukey, F. Separovic, W. M. Kriven, and J. S. J. Van Deventer, “Modeling speciation in highly concentrated alkaline silicate solutions,” *Industrial and Engineering Chemistry Research*, vol. 44, no. 23. pp. 8899–8908, 2005.

[44] R. E. Edsinger, M. L. Reilly, and J. F. Schooley, “Thermal expansion of platinum and platinum-rhodium alloys (Journal of Research of the National Institute of Standards and

Technology (1986) 91:6 (333) DOI: 10.6028/jres.091.037)," *Journal of Research of the National Institute of Standards and Technology*, vol. 91, no. 6. p. 1, 1986.

[45] A. Filipponi *et al.*, "Multichannel detector-collimator for powder diffraction measurements at energy scanning x-ray absorption spectroscopy synchrotron radiation beamlines for high-pressure and high-temperature applications," *Rev. Sci. Instrum.*, vol. 74, no. 5, pp. 2654–2663, 2003.

[46] N. E. Brown, S. M. Swapp, C. L. Bennett, and A. Navrotsky, "High-temperature X-ray diffraction: Solutions to uncertainties in temperature and sample position," *J. Appl. Crystallogr.*, vol. 26, no. pt 1, pp. 77–81, 1993.

[47] S. Seltzer, "Tables of X-Ray Mass Attenuation Coefficients and Mass Energy-Absorption Coefficients, NIST Standard Reference Database 126," *NIST Standard Reference Database 126*. 1996.

[48] S. Stecura, "Evaluation of an imaging furnace as a heat source for x-ray diffractometry," *Rev. Sci. Instrum.*, vol. 39, no. 5, pp. 760–765, 1968.

[49] A. Watanabe and M. Shimazu, "High-temperature X-ray diffraction furnace using a thermal-image technique," *J. Appl. Crystallogr.*, vol. 9, no. 6, pp. 466–469, Dec. 1976.

[50] J. Schneider, "Mirror Heaters for High Temperature X-ray Diffraction," *Adv. X-ray Anal.*, vol. 36, pp. 397–402, 1993.

[51] L. F. Siah, W. M. Kriven, and J. Schneider, "In situ, high-temperature, synchrotron, powder diffraction studies of oxide systems in air, using a thermal-image furnace," *Meas. Sci. Technol.*, vol. 16, no. 6, pp. 1291–1298, 2005.

[52] P. Sarin, W. Yoon, K. Jurkschat, P. Zschack, and W. M. Kriven, "Quadrupole lamp furnace for high temperature (up to 2050 K) synchrotron powder x-ray diffraction studies in air in reflection geometry," *Rev. Sci. Instrum.*, vol. 77, no. 9, p. 093906, Sep. 2006.

[53] Y. S. Touloukian, R. K. Kirby, R. E. Taylor, and T. Y. R. Lee, *Thermal expansion - nonmetallic solids*. 1977.

[54] S. W. Freiman and N. M. Trahey, "National Institute of Standards & Technology Standard Reference Material 660a Lanthanum Hexaboride Powder Line Position and Line Shape Standard for Powder Diffraction," 2000.

[55] H. M. Rietveld, "Line profiles of neutron powder-diffraction peaks for structure refinement," *Acta Crystallogr.*, vol. 22, no. 1, pp. 151–152, 1967.

[56] H. M. Rietveld, "A profile refinement method for nuclear and magnetic structures," *J. Appl. Crystallogr.*, vol. 2, no. 2, pp. 65–71, 1969.

[57] B. O. Loopstra and H. M. Rietveld, "Further refinement of the structure of WO3," *Acta Crystallogr. Sect. B*, vol. 25, pp. 1420–1421, 1969.

[58] G. Malmros and J. O. Thomas, "Least-squares structure refinement based on profile analysis of powder film intensity data measured on an automatic microdensitometer," *J. Appl. Crystallogr.*, vol. 10, no. 1, pp. 7–11, 1977.

[59] B. H. Toby and R. B. Von Dreele, “GSAS-II: the genesis of a modern open-source all purpose crystallography software package,” *J. Appl. Cryst*, vol. 46, pp. 544–549, 2013.

[60] K. Momma and F. Izumi, “VESTA 3 for three-dimensional visualization of crystal, volumetric and morphology data,” *J. Appl. Cryst*, vol. 44, pp. 1272–1276, 2011.

[61] R. B. Frost and J. S. Beard, “On silica activity and serpentinization,” *J. Petrol.*, vol. 48, no. 7, pp. 1351–1368, 2007.

[62] A. Navrotsky, “Repeating patterns in mineral energetics,” *Am. Mineral.*, vol. 79, no. 7–8, pp. 589–605, 1994.

[63] W. H. Taylor, “The structure of analcite (NaAlSi2O6·H2O),” *Zeitschrift für Krist. - Cryst. Mater.*, vol. 74, no. 1–6, pp. 1–19, Jan. 2014.

[64] W. H. Taylor, “Note on the structures of analcite and pollucite,” *Zeitschrift für Krist. - Cryst. Mater.*, vol. 99, no. 1–6, Jan. 2014.

[65] S. Náray-Szabó, “Note on the structure of analcite,” *Zeitschrift für Krist. - Cryst. Mater.*, vol. 99, no. 1–6, Jan. 2014.

[66] S. Náray-Szabó, “Die struktur des pollucits CsAlSi2O6 · xH2O,” *Zeitschrift für Krist. - Cryst. Mater.*, vol. 99, no. 1–6, Jan. 2014.

[67] D. L. R. Peacor, “A high temperature single crystal diffractometer study of leucite, (K,Na)AlSi2O6,” *Zeitschrift fur Krist. - New Cryst. Struct.*, vol. 127, no. 1–4, pp. 213–224, 1968.

[68] F. Mazzi, “Is each analcime different?,” *Am. Mineral.*, vol. 63, no. 5–6, pp. 448–460, 1978.

[69] F. Mazzi, E. Galli, and G. Gottardi, “The crystal structure of tetragonal leucite,” *Am. Mineral.*, vol. 61, pp. 108–115, 1976.

[70] J. Wyart, “Etude cristallographique d’une leucite artificielle. Structure atomique et symétrie du minéral,” *Bull. la Société française Minéralogie*, vol. 63, no. 1, pp. 5–17, 1940.

[71] K. Hirao, M. Kunugi, K. Hirao, N. Soga, and M. Kunugi, “Thermal expansion and structure of leucite-type compounds,” *J. Phys. Chem.*, vol. 80, no. 14, pp. 1612–1616, 1976.

[72] R. A. Lange and I. S. E. Carmichael, “Phase transitions in leucite (KAlSi2O6), orthorhombic KAlSiO4, and their iron analogues (KFeSi2O6, KFeSiO4),” *Am. Mineral.*, vol. 71, pp. 937–945, 1986.

[73] D. Taylor, “The structural behaviour of tetrahedral framework compounds a review. Part I. Structural behaviour,” *Mineral. Mag.*, vol. 47, pp. 319–345, 1983.

[74] D. Taylor, “The structural behaviour of tetrahedral framework compounds — a review Part II. Framework structures,” *Mineral. Mag.*, vol. 48, no. 346, pp. 65–79, 1984.

[75] R. M. Hazen, “Sanidine: Predicted and observed monoclinic-to-triclinic reversible

transformations at high pressure," *Science (80-.).*, vol. 194, no. 4260, pp. 105–107, 1976.

[76] R. M. Hazen, "Temperature, pressure and composition: Structurally analogous variables," *Phys. Chem. Miner.*, vol. 1, no. 1, pp. 83–94, 1977.

[77] R. M. Hazen and L. W. Finger, "Polyhedral tilting: A common type of pure displacive phase transition and its relationship to analcite at high pressure," *Phase Transitions*, vol. 1, no. 1, pp. 1–22, Sep. 1979.

[78] G. Ferraris, D. W. Jones, and J. Yerkess, "A neutron-diffraction study of the crystal structure of analcime, NaAlSi2O6 · H2O," *Zeitschrift fur Krist. - New Cryst. Struct.*, vol. 135, no. 3–4, pp. 240–252, Jan. 1972.

[79] D. C. Palmer, E. K. H. Salje, and W. W. Schmahl, "Phase transitions in leucite: X-ray diffraction studies," *Phys. Chem. Miner.*, vol. 16, no. 7, pp. 714–719, 1989.

[80] P. J. Heaney and D. R. Veblen, "A high-temperature study of the low-high leucite phase transition using the transmission electron microscope," *Am. Mineral.*, vol. 75, no. 5–6, pp. 464–476, 1990.

[81] A. El-Maghraby, K. F. Khaled, and K. M. Elsabawy, "Formation of leucite crystals from metakaolin-based geopolymer using kaolin and bentonite," *Int. J. Chem. Sci.*, vol. 11, no. 2, pp. 740–750, 2013.

[82] R. Sadanaga and T. Ozawa, "Thermal transition of leucite," *Mineral. J.*, vol. 5, no. 5, pp. 321–333, 1968.

[83] P. He and D. Jia, "Low-temperature sintered pollucite ceramic from geopolymer precursor using synthetic metakaolin," *J. Mater. Sci.*, vol. 48, no. 4, pp. 1812–1818, 2013.

[84] M. F. Brigatti and S. Guggenheim, "Mica crystal chemistry and the influence of pressure, temperature, and solid solution on atomistic models," *Rev. Mineral. Geochemistry*, vol. 46, no. 1, pp. 1–97, 2010.

[85] M. F. Brigatti, E. Galán, and B. K. G. Theng, "Structure and mineralogy of clay minerals," *Dev. Clay Sci.*, vol. 5, pp. 21–81, 2013.

[86] R. M. Hazen, R. T. Downs, and C. T. Prewitt, "Principles of comparative crystal chemistry," *Rev. Mineral. Geochemistry*, vol. 41, no. 1, pp. 1–33, 2012.

[87] W. H. Baur, "The geometry of polyhedral distortions. Predictive relationships for the phosphate group," *Acta Crystallogr.*, vol. 16, p. 1195, 1974.

[88] K. Robinson, G. V Gibbs, and P. H. Ribbe, "Quadratic elongation: A quantitative measure of distortion in coordination polyhedra," *Science (80-.).*, vol. 172, no. 3983, pp. 567–570, 1971.

[89] A. R. Boccaccini, "A new equation for the determination of the thermal expansion coefficient of particulate composites," *Adv. Compos. Lett.*, vol. 5, no. 1, pp. 15–19, 1996.

[90] K. Makarian, S. Santhanam, and Z. N. Wing, "Coefficient of thermal expansion of particulate composites with ceramic inclusions," *Ceram. Int.*, vol. 42, no. 15, pp. 17659–17665, Nov. 2016.

[91] C. Dellacorte and J. A. Fellenstein, “The effect of compositional tailoring on the thermal expansion and tribological properties of ps300: A solid lubricant composite coating,” *Tribol. Trans.*, vol. 40, no. 4, pp. 639–642, 1997.

[92] S. Naqash, M. T. Gerhards, F. Tietz, and O. Guillon, “Coefficients of thermal expansion of Al-and Y-substituted NaSiCON solid solution Na3+2x Alx Yx Zr2−2x Si2 PO12,” *Batteries*, vol. 4, no. 3, 2018.

[93] M. S. A. Karunaratne, S. Kyaw, A. Jones, R. Morrell, and R. C. Thomson, “Modelling the coefficient of thermal expansion in Ni-based superalloys and bond coatings,” *J. Mater. Sci.*, vol. 51, no. 9, pp. 4213–4226, 2016.

[94] G. Laplanche *et al.*, “Elastic moduli and thermal expansion coefficients of medium-entropy subsystems of the CrMnFeCoNi high-entropy alloy,” *J. Alloys Compd.*, vol. 746, pp. 244–255, May 2018.

[95] J. A. Monroe, D. Gehring, I. Karaman, R. Arroyave, D. W. Brown, and B. Clausen, “Tailored thermal expansion alloys,” *Acta Mater.*, vol. 102, pp. 333–341, Jan. 2016.

[96] R. D. Shannon, “Revised effective ionic radii and systematic studies of interatomic distances in halides and chalcogenides,” *Acta Crystallogr. Sect. A*, vol. 32, no. 5, pp. 751–767, 1976.

[97] M. Mrázová and A. Kloužková, “Leucite porcelain fused to metals for dental restoration,” *Ceramics - Silikaty*, vol. 53, no. 3. pp. 225–230, 2009.

[98] M. A. Carpenter and D. Cellai, “Microstructures and high-temperature phase transitions in kalsilite,” *Am. Mineral.*, vol. 81, no. 5–6, pp. 561–584, 1996.

[99] D. Cellai, T. M. Gesing, B. Wruck, and M. A. Carpenter, “X-ray study of the trigonal → hexagonal phase transition in metamorphic kalsilite,” *Am. Mineral.*, vol. 84, no. 11–12, pp. 1950–1955, 1999.

[100] J. F. Schairer, “The alkali-feldspar join in the system NaAlSiO4-KAlSiO4-SiO2,” *J. Geol.*, vol. 58, no. 5, pp. 512–517, 1950.

[101] H. E. Eaton, G. D. Linsey, K. L. More, J. B. Kimmei, J. R. Price, and N. Miriyala, “EBC protection of SiC/SiC composites in the gas turbine combustion environment,” in *Proceedings of the ASME Turbo Expo*, 2000, vol. 4.

[102] Y. Xu, X. Hu, F. Xu, and K. Li, “Rare earth silicate environmental barrier coatings: Present status and prospective,” *Ceramics International*, vol. 43, no. 8. Elsevier Ltd, pp. 5847–5855, 01-Jun-2017.

[103] D. Zhu, *Engineered Ceramics: Current Status and Future Prospects*. Hoboken: Wiley, 2016.

[104] Z. Tian, L. Zheng, W. Hu, L. Sun, J. Zhang, and J. Wang, “Tunable properties of (HoxY1-x)2SiO5 as damage self-monitoring environmental/thermal barrier coating candidates,” *Sci. Rep.*, vol. 9, no. 1, 2019.

[105] P. Dhé, “Tipping crucible for basalt furnaces,” US Patent No. 1462446.

[106] W. Weibull, “A statistical distribution function of wide applicability,” *J. Appl. Mech.*, vol. 13, pp. 293–297, 1951.

[107] ASTM International, “C1239 − 13 (Reapproved 2018) Standard Practice for Reporting Uniaxial Strength Data and Estimating Weibull Distribution Parameters for Advanced Ceramics.” American Society for Testing and Materials, West Conshohocken, PA, 2018.

[108] A. Benard and E. C. Bos-Levenbach, “Het uitzetten van waarnemingen op waarschijnlijkheids-papier,” *Stat. Neerl.*, vol. 7, no. 3, pp. 163–173, Jan. 1953.

[109] ASTM International, “C109/C109M − 16a Standard Test Method for Compressive Strength of Hydraulic Cement Mortars.” American Society for Testing and Materials, West Conshohocken, PA, 2016.

[110] ASTM International, “C78/C78M − 18 Standard Test Method for Flexural Strength of Concrete.” American Society for Testing and Materials, West Conshohocken, PA, 2018.

[111] ASTM International, “C1161 − 18 Standard Test Method for Flexural Strength of Advanced Ceramics at Ambient Temperature.” American Society for Testing and Materials, West Conshohocken, PA, 2018.

[112] D. Ribero and W. M. Kriven, “Properties of geopolymer composites reinforced with basalt chopped strand mat or woven fabric,” *J. Am. Ceram. Soc.*, vol. 99, no. 4, pp. 1192–1199, 2016.

[113] ASTM International, “D7078/D7078M − 19 Standard Test Method for Shear Properties of Composite Materials by V-Notched Rail Shear Method.” American Society for Testing and Materials, West Conshohocken, PA, 2019.

[114] ASTM International, “C1421 − 18 Standard Test Methods for Determination of Fracture Toughness of Advanced Ceramics at Ambient Temperature.” American Society for Testing and Materials, West Conshohocken, PA, 2018.

[115] S. Cho, “Geopolymer Composites and Their Applications in Stress Wave Mitigation,” University of Illinois at Urbana-Champaign, 2015.

[116] P. J. Tumidajski, L. Fiore, T. Khodabocus, M. Lachemi, and R. Pari, “Comparison of Weibull and normal distributions for concrete compressive strengths,” *Can. J. Civ. Eng.*, vol. 33, no. 10, pp. 1287–1292, 2007.

[117] J. Seuba, S. Deville, C. Guizard, and A. J. Stevenson, “The effect of wall thickness distribution on mechanical reliability and strength in unidirectional porous ceramics,” *Sci. Technol. Adv. Mater.*, vol. 17, no. 1, pp. 128–135, 2016.

[118] B. Chen and J. Liu, “Experimental study on AE characteristics of three-point-bending concrete beams,” *Cem. Concr. Res.*, vol. 34, no. 3, pp. 391–397, 2004.

[119] L. Ćurković, A. Bakić, J. Kodvanj, and T. Haramina, “Flexural strength of alumina ceramics: Weibull analysis,” *Trans. Famena*, vol. 34, no. 1, pp. 13–18, 2010.

[120] B. Djazmati and J. A. Pincheira, “Shear stiffness and strength of horizontal construction joints,” *ACI Struct. J.*, vol. 101, no. 4, pp. 484–493, 2004.

[121] C. Shih *et al.*, “Comparison of shear strength of ceramic joints determined by various test methods with small specimens,” in *Ceramic Materials for Energy Applications IV*, 2015, pp. 139–149.

[122] S. Seitl, J. D. Ríos, and H. Cifuentes, “Comparison of fracture toughness values of normal and high strength concrete determined by three point bend and modified disk-shaped compact tension specimens,” *Frat. ed Integrita Strutt.*, vol. 11, no. 42, pp. 56–65, 2017.

[123] G. A. Gogotsi, “Fracture toughness of ceramics and ceramic composites,” *Ceram. Int.*, vol. 29, no. 7, pp. 777–784, 2003.

[124] A. K. Gupta, “Ternary systems with feldspathoids,” in *Origin of Potassium-rich Silica-deficient Igneous Rocks*, New Delhi: Springer India, 2015, pp. 259–276.

[125] G. Sen, “Phase relations in simple systems: Key to magma generation, crystallization, and mixing,” in *Petrology: Principles and Practice*, Berlin, Heidelberg: Springer Berlin Heidelberg, 2014, pp. 51–78.

APPENDIX – SUPPLEMENTARY DATA

Table 8 – Empirical unit cell parameters for the $K_xCs_{1-x}[AlSi_2O_6]$ series

t-KAlSi2O6				c-KAlSi2O6		
Temperature (°C)	a [Å]	c [Å]	Unit cell volume (Å^3)	Temperature (°C)	a [Å]	Unit cell volume (Å^3)
30	13.07565	13.76021	2352.6193	535	13.50599953	2463.6567
320	13.18718	13.73603	2388.719	587	13.60869974	2520.2864
425	13.24689	13.71829	2407.2869	637	13.54428966	2484.6699
479	13.28559	13.70506	2419.0377	690	13.55313962	2489.5436
535	13.33429	13.68454	2433.156	740	13.55984026	2493.2379
587	13.4035	13.65	2452.2743	858	13.57011984	2498.9125
637	13.54429	13.54429	2484.6699	944	13.57829005	2503.4288
-	-	-	-	1042	13.5851402	2507.2196
-	-	-	-	1130	13.59080026	2510.3547
-	-	-	-	1210	13.59548004	2512.9488
-	-	-	-	1284	13.5998897	2515.3948
-	-	-	-	1360	13.60396961	2517.6593
-	-	-	-	1452	13.60869974	2520.2864
-	-	-	-	-	-	-
-	-	-	-	-	-	-

t-K80Cs20				c-K80Cs20		
Temperature (°C)	a [Å]	c [Å]	Unit cell volume (Å^3)	Temperature (°C)	a [Å]	Unit cell volume (Å^3)
30	13.2527	13.7333	2412.0352	30	13.46839998	2443.1381
39	13.2562	13.7319	2413.0634	39	13.48630051	2452.8924
238	13.3519	13.7067	2443.5378	365	13.53899962	2481.7597
365	13.4469	13.6626	2470.4594	427	13.55360035	2489.7975
-	-	-	-	485	13.58	2504.3583
-	-	-	-	601	13.6006	2515.8166
-	-	-	-	820	13.6209	2527.0486
-	-	-	-	911	13.653	2544.9985
-	-	-	-	1041	13.6785	2559.2906
-	-	-	-	1170	13.704	2573.5827
-	-	-	-	1299	13.7292	2587.8747
-	-	-	-	1428	13.7545	2602.1668
-	-	-	-	-	-	-
-	-	-	-	-	-	-
-	-	-	-	-	-	-

Table 8 (cont.)

K20Cs80			CsAlSi2O8		
Temperature (°C)	a [Å]	Unit cell volume (Å^3)	Temperature (°C)	a [Å]	Unit cell volume (Å^3)
30	13.6515	2544.1405	30	13.7251	2585.4869
227	13.6821	2561.2702	154	13.7276	2586.9305
352	13.6907	2566.1085	289	13.7314	2589.0818
475	13.6963	2569.2812	407	13.734	2590.5677
597	13.7012	2572.0569	494	13.734	2590.545
715	13.7059	2574.6654	578	13.7348	2591.0205
824	13.7096	2576.7679	658	13.7367	2592.0958
924	13.7128	2578.5557	741	13.7395	2593.6304
1027	13.7155	2580.0963	815	13.7421	2595.1537
1115	13.7178	2581.3774	889	13.7451	2596.8479
1188	13.7214	2583.4443	1002	13.7488	2598.923
1258	13.7241	2584.9356	1098	13.7527	2601.1524
1333	13.7268	2586.4561	1238	13.7572	2603.6954
1373	13.7288	2587.6148	1358	13.7616	2606.194
1409	13.7307	2588.6837	1456	13.7663	2608.8938

K60Cs40			K40Cs60		
Temperature (°C)	a [Å]	Unit cell volume (Å^3)	Temperature (°C)	a [Å]	Unit cell volume (Å^3)
30	13.4957	2458.0254	30	13.5658	2496.5224
358	13.5971	2513.8473	232	13.621	2527.1542
484	13.6183	2525.6131	359	13.6426	2539.151
608	13.6307	2532.5347	470	13.6528	2544.8449
728	13.6394	2537.3814	607	13.6614	2549.702
846	13.6458	2540.9326	700	13.6667	2552.6426
957	13.6511	2543.8947	823	13.6743	2556.9093
1061	13.6556	2546.4169	922	13.6777	2558.817
1160	13.659	2548.3529	1041	13.6805	2560.3775
1250	13.6617	2549.859	1116	13.6831	2561.8712
1332	13.6638	2551.0292	1206	13.6849	2562.888
1414	13.6651	2551.7685	1298	13.6864	2563.7031
1493	13.6663	2552.4353	1368	13.6878	2564.4899
1562	13.67	2554.5033	1458	13.6918	2566.7387
-	-	-	1533	13.6928	2567.3008

Table 9 – Empirical atomic parameters for t-K[$AlSi_2O_6$] through the temperature range

Temp.	Label	X	Y	Z	Occ.	U_iso	Mult.
30	K1	0.3656(3)	0.36380(30)	0.1147(4)	1	0.0886(17)	16
	Si2	0.05880(11)	0.39563(12)	0.16721(10)	0.67	0.0278(15)	16
	Al3	0.0588	0.39563	0.16721	0.33	0.0278	16
	Si4	0.16551(11)	0.61125(11)	0.12884(12)	0.67	0.0189(14)	16
	Al5	0.16551	0.61125	0.12884	0.33	0.0189	16
	Si6	0.39232(12)	0.64136(12)	0.08758(11)	0.67	0.0232(14)	16
	Al7	0.39232	0.64136	0.08758	0.33	0.0232	16
	O8	0.12976(22)	0.3080(6)	0.1102(3)	1	0.077(5)	16
	O9	0.0937(3)	0.5053(5)	0.13492(24)	1	0.040(4)	16
	O10	0.14763(17)	0.67834(24)	0.2240(5)	1	0.029(3)	16
	O11	0.13359(18)	0.67690(27)	0.0338(5)	1	0.0275(31)	16
	O12	0.2887(4)	0.57877(18)	0.12111(19)	1	0.0140(28)	16
	O13	0.4836(4)	0.61807(10)	0.16396(28)	1	0.0145(29)	16
320	K1	0.3670(4)	0.3632(4)	0.1171(5)	1	0.1136(22)	16
	Si2	0.06266(12)	0.39281(13)	0.16571(11)	0.67	0.0264(19)	16
	Al3	0.06266	0.39281	0.16571	0.33	0.0264	16
	Si4	0.16624(12)	0.60805(12)	0.12743(13)	0.67	0.0170(16)	16
	Al5	0.16624	0.60805	0.12743	0.33	0.017	16
	Si6	0.39027(13)	0.64347(13)	0.08732(12)	0.67	0.0180(17)	16
	Al7	0.39027	0.64347	0.08732	0.33	0.018	16
	O8	0.12969(24)	0.3034(7)	0.1108(4)	1	0.073(6)	16
	O9	0.1003(4)	0.5001(7)	0.13075(29)	1	0.068(6)	16
	O10	0.14339(19)	0.67299(28)	0.2244(6)	1	0.026(4)	16
	O11	0.13336(20)	0.6730(3)	0.0328(7)	1	0.038(4)	16
	O12	0.2873(5)	0.58238(19)	0.12158(23)	1	0.011(3)	16
	O13	0.4820(4)	0.61795(11)	0.1622(3)	1	0.028(4)	16
425	K1	0.3680(4)	0.3642(4)	0.1162(5)	1	0.1244(20)	16
	Si2	0.06524(11)	0.39179(11)	0.16476(10)	0.67	0.0332(19)	16
	Al3	0.06524	0.39179	0.16476	0.33	0.0332	16
	Si4	0.16693(11)	0.60581(11)	0.12620(11)	0.67	0.0323(18)	16
	Al5	0.16693	0.60581	0.1262	0.33	0.0323	16
	Si6	0.38949(11)	0.64395(11)	0.08714(10)	0.67	0.0270(17)	16
	Al7	0.38949	0.64395	0.08714	0.33	0.027	16
	O8	0.12935(20)	0.3035(6)	0.1132(3)	1	0.052(5)	16
	O9	0.1057(3)	0.5009(6)	0.12705(26)	1	0.061(5)	16
	O10	0.14074(17)	0.67001(25)	0.2262(6)	1	0.030(4)	16
	O11	0.13421(17)	0.67154(27)	0.0312(6)	1	0.046(4)	16

Table 9 (cont.)

	O12	0.2869(4)	0.58292(17)	0.12186(20)	1	0.0044(30)	16
	O13	0.4814(4)	0.61746(10)	0.16098(28)	1	0.016(3)	16
	K1	0.3681(4)	0.3641(4)	0.1173(5)	1	0.1381(22)	16
	Si2	0.06702(11)	0.39041(11)	0.16403(10)	0.67	0.0421(22)	16
	Al3	0.06702	0.39041	0.16403	0.33	0.0421	16
	Si4	0.16730(11)	0.60383(11)	0.12583(11)	0.67	0.0352(19)	16
	Al5	0.1673	0.60383	0.12583	0.33	0.0352	16
	Si6	0.38824(11)	0.64489(11)	0.08672(10)	0.67	0.0259(19)	16
479	Al7	0.38824	0.64489	0.08672	0.33	0.0259	16
	O8	0.12923(21)	0.3015(6)	0.1133(3)	1	0.055(5)	16
	O9	0.1079(4)	0.4967(6)	0.12563(27)	1	0.069(5)	16
	O10	0.13883(18)	0.66687(26)	0.2262(6)	1	0.030(4)	16
	O11	0.13395(18)	0.66937(29)	0.0305(6)	1	0.056(5)	16
	O12	0.2854(4)	0.58402(17)	0.12246(21)	1	0.012(3)	16
	O13	0.4819(4)	0.61715(10)	0.16040(28)	1	0.015(4)	16
	K1	0.3690(5)	0.3641(5)	0.1169(7)	1	0.1458(27)	16
	Si2	0.06973(12)	0.38876(13)	0.16372(12)	0.67	0.0479(28)	16
	Al3	0.06973	0.38876	0.16372	0.33	0.0479	16
	Si4	0.16765(12)	0.60166(12)	0.12544(13)	0.67	0.0398(24)	16
	Al5	0.16765	0.60166	0.12544	0.33	0.0398	16
	Si6	0.38691(13)	0.64617(13)	0.08669(12)	0.67	0.0281(23)	16
535	Al7	0.38691	0.64617	0.08669	0.33	0.0281	16
	O8	0.12962(25)	0.2993(8)	0.1136(4)	1	0.065(6)	16
	O9	0.1126(4)	0.4943(7)	0.1244(3)	1	0.089(7)	16
	O10	0.13613(21)	0.6632(3)	0.2257(8)	1	0.051(5)	16
	O11	0.13290(21)	0.6668(3)	0.0286(8)	1	0.065(6)	16
	O12	0.2848(6)	0.58596(20)	0.12334(24)	1	0.012(4)	16
	O13	0.4812(6)	0.61693(11)	0.1587(3)	1	0.020(5)	16
	K1	0.37208	0.36776	0.11714	1	0.141	16
	Si2	0.07036	0.38696	0.16254	0.67	0.06	16
	Al3	0.0703644	0.386956	0.162544	0.33	0.0597824	16
	Si4	0.16867	0.60064	0.12598	0.67	0.045	16
	Al5	0.168672	0.600641	0.125977	0.33	0.0452862	16
	Si6	0.38651	0.64677	0.08551	0.67	0.016	16
587	Al7	0.386508	0.64677	0.0855134	0.33	0.0156082	16
	O8	0.12588	0.30608	0.12102	1	0.106	16
	O9	0.11542	0.49472	0.12096	1	0.091	16
	O10	0.13476	0.6598	0.23023	1	0.008	16
	O11	0.13391	0.67032	0.02764	1	0.059	16
	O12	0.28436	0.58608	0.12492	1	-0.013	16
	O13	0.48758	0.61719	0.16106	1	0.001	16

Table 10 – Empirical atomic parameters for c-K[$AlSi_2O_6$] through the temperature range

Temp.	Label	X	Y	Z	Occ.	U_iso	Mult.
535	K1	0.125	0.125	0.125	1	0.361	16
	Al2	0.66078	0.58922	0.125	0.33	0.106	48
	Si3	0.66077	0.58923	0.125	0.67	0.049	48
	O4	0.10989	0.13153	0.71801	1	0.201	96
587	K1	0.125	0.125	0.125	1	0.269(7)	16
	Al2	0.66181(12)	0.58819	0.125	0.33	0.0622(25)	48
	Si3	0.66181	0.588186	0.125	0.67	0.0622	48
	O4	0.10788(12)	0.13201(7)	0.72239(25)	1	0.078(4)	96
637	K1	0.125	0.125	0.125	1	0.1873(21)	16
	Al2	0.66174(7)	0.58826	0.125	0.33	0.0365(6)	48
	Si3	0.66174	0.588265	0.125	0.67	0.0365	48
	O4	0.10814(7)	0.13206(5)	0.72159(13)	1	0.0668(12)	96
690	K1	0.125	0.125	0.125	1	0.1952(23)	16
	Al2	0.66184(8)	0.58816	0.125	0.33	0.0353(6)	48
	Si3	0.66184	0.588157	0.125	0.67	0.0353	48
	O4	0.10792(7)	0.13211(5)	0.72206(14)	1	0.0615(12)	96
740	K1	0.125	0.125	0.125	1	0.2112(25)	16
	Al2	0.66210(8)	0.5879	0.125	0.33	0.0358(7)	48
	Si3	0.6621	0.587896	0.125	0.67	0.0358	48
	O4	0.10753(7)	0.13220(5)	0.72300(14)	1	0.0570(12)	96
858	K1	0.125	0.125	0.125	1	0.2151(24)	16
	Al2	0.66202(8)	0.58798	0.125	0.33	0.0348(7)	48
	Si3	0.66202	0.587979	0.125	0.67	0.0348	48
	O4	0.10767(7)	0.13216(5)	0.72267(14)	1	0.0594(12)	96
944	K1	0.125	0.125	0.125	1	0.283	16
	Al2	0.66244(12)	0.58756	0.125	0.33	0.087	48
	Si3	0.66244	0.58756	0.125	0.67	0.0869017	48
	O4	0.10661(10)	0.13243(7)	0.72470(18)	1	0.01	96
1042	K1	0.125	0.125	0.125	1	0.245(3)	16
	Al2	0.66229(9)	0.58771	0.125	0.33	0.0352(8)	48
	Si3	0.66229	0.587706	0.125	0.67	0.0352	48
	O4	0.10716(8)	0.13221(6)	0.72383(16)	1	0.0580(15)	96

Table 10 (cont.)

1130	K1	0.125	0.125	0.125	1	0.251(3)	16
	Al2	0.66229(9)	0.58771	0.125	0.33	0.0349(8)	48
	Si3	0.66229	0.587715	0.125	0.67	0.0349	48
	O4	0.10715(8)	0.13222(6)	0.72388(16)	1	0.0585(15)	96
1210	K1	0.125	0.125	0.125	1	0.2506(28)	16
	Al2	0.66217(8)	0.58783	0.125	0.33	0.0370(7)	48
	Si3	0.66217	0.58783	0.125	0.67	0.037	48
	O4	0.10736(7)	0.13221(5)	0.72342(14)	1	0.0609(13)	96
1284	K1	0.125	0.125	0.125	1	0.2553(29)	16
	Al2	0.66213(8)	0.58787	0.125	0.33	0.0375(8)	48
	Si3	0.66213	0.587866	0.125	0.67	0.0375	48
	O4	0.10745(8)	0.13220(5)	0.72325(15)	1	0.0632(14)	96
1360	K1	0.125	0.125	0.125	1	0.2630(30)	16
	Al2	0.66216(8)	0.58784	0.125	0.33	0.0382(8)	48
	Si3	0.66216	0.587837	0.125	0.67	0.0382	48
	O4	0.10739(8)	0.13221(5)	0.72340(15)	1	0.0648(14)	96
1452	K1	0.125	0.125	0.125	1	0.2673(31)	16
	Al2	0.66216(8)	0.58784	0.125	0.33	0.0395(8)	48
	Si3	0.66216	0.587843	0.125	0.67	0.0395	48
	O4	0.10739(8)	0.13220(5)	0.72341(15)	1	0.0666(15)	96

Table 11 – Empirical atomic parameters for t-$K_{0.8}Cs_{0.2}[AlSi_2O_6]$ through the temperature range

Temp.	Label	X	Y	Z	Occ.	U_iso	Mult.
30	K1	0.3708(8)	0.3730(8)	0.1322(9)	0.8	0.0091(26)	16
	Si2	0.05623(20)	0.39698(23)	0.16118(19)	0.67	0.044(7)	16
	Al3	0.05623	0.39698	0.16118	0.33	0.044	16
	Si4	0.15313(22)	0.61007(23)	0.13176(24)	0.67	0.076(8)	16
	Al5	0.15313	0.61007	0.13176	0.33	0.076	16
	Si6	0.40370(21)	0.64485(23)	0.08668(20)	0.67	0.086(10)	16
	Al7	0.4037	0.64485	0.08668	0.33	0.086	16
	O8	0.1076(11)	0.3472(19)	0.1186(14)	1	0.46(6)	16
	O9	0.0730(8)	0.4975(25)	0.1349(12)	1	0.152(30)	16
	O10	0.1318(4)	0.6773(7)	0.2259(18)	1	0.066(15)	16
	O11	0.1306(8)	0.6679(12)	0.0456(21)	1	0.063(14)	16
	O12	0.3059(15)	0.5661(9)	0.1300(8)	1	0.085(14)	16
	O13	0.5122(17)	0.62599(23)	0.1571(5)	1	0.031(10)	16
	Cs14	0.3708	0.373	0.1322	0.2	0.0091	16
39	K1	0.3700(9)	0.3712(9)	0.1255(12)	0.8	0.0078(26)	16
	Si2	0.05482(22)	0.39497(24)	0.16360(21)	0.67	0.045(8)	16
	Al3	0.05482	0.39497	0.1636	0.33	0.045	16
	Si4	0.16226(23)	0.61186(24)	0.13513(24)	0.67	0.055(8)	16
	Al5	0.16226	0.61186	0.13513	0.33	0.055	16
	Si6	0.40222(20)	0.64163(22)	0.08598(20)	0.67	0.062(8)	16
	Al7	0.40222	0.64163	0.08598	0.33	0.062	16
	O8	0.1204(15)	0.321(3)	0.1198(21)	1	0.48(6)	16
	O9	0.0862(16)	0.5048(30)	0.1273(13)	1	0.156(31)	16
	O10	0.1385(7)	0.6744(8)	0.2448(25)	1	0.092(18)	16
	O11	0.1382(7)	0.6833(17)	0.0491(21)	1	0.047(14)	16
	O12	0.3065(15)	0.5711(8)	0.1300(7)	1	0.067(14)	16
	O13	0.5150(19)	0.62583(20)	0.1652(8)	1	0.051(13)	16
	Cs14	0.37	0.3712	0.1255	0.2	0.0078	16
238	K1	0.37674	0.37276	0.12624	0.8	0.01	16
	Si2	0.06583	0.38865	0.15802	0.67	0.058	16
	Al3	0.0658288	0.388648	0.15802	0.33	0.0584339	16
	Si4	0.16347	0.60159	0.12943	0.67	0.1	16
	Al5	0.163467	0.601586	0.129432	0.33	0.0998491	16
	Si6	0.40005	0.64728	0.08052	0.67	0.052	16
	Al7	0.400054	0.647272	0.0805223	0.33	0.0524188	16
	O8	0.1165(7)	0.3226(16)	0.1166(10)	1	0.01	16

Table 11 (cont.)

	O9	0.0893(7)	0.4701(19)	0.1274(9)	1	0.01	16
	O10	0.1323(4)	0.6725(5)	0.2443(14)	1	0.01	16
	O11	0.1340(5)	0.6606(9)	0.0456(13)	1	0.01	16
	O12	0.2991(13)	0.5771(4)	0.1247(5)	1	0.01	16
	O13	0.5212(16)	0.62859(18)	0.1715(5)	1	0.01	16
	Cs14	0.37674	0.37276	0.12624	0.2	0.01	16
365	K1	0.3786(16)	0.3658(13)	0.1305(14)	0.8	0.022(5)	16
	Si2	0.06882(17)	0.38899(19)	0.15881(19)	0.67	0.037(11)	16
	Al3	0.06882	0.38899	0.15881	0.33	0.037	16
	Si4	0.15626(26)	0.59608(29)	0.12494(28)	0.67	0.030(7)	16
	Al5	0.15626	0.59607	0.12494	0.33	0.03	16
	Si6	0.40707(20)	0.62884(24)	0.07646(20)	0.67	0.29(4)	16
	Al7	0.40707	0.62884	0.07646	0.33	0.29	16
	O8	0.0995(13)	0.3614(16)	0.1284(22)	1	0.22(5)	16
	O9	0.0870(7)	0.4958(24)	0.1425(16)	1	0.028(11)	16
	O10	0.1394(7)	0.6791(11)	0.2234(20)	1	0.027(10)	16
	O11	0.1163(12)	0.6615(12)	0.0020(30)	1	0.27(5)	16
	O12	0.3345(22)	0.5467(14)	0.1151(11)	1	0.21(4)	16
	O13	0.553(4)	0.6245(12)	0.1662(4)	1	0.109(28)	16
	Cs14	0.3786	0.3658	0.1305	0.2	0.022	16

Table 12 – Empirical atomic parameters for c-$K_{0.8}Cs_{0.2}[AlSi_2O_6]$ through the temperature range

Temp.	Label	X	Y	Z	Occ.	U_iso	Mult.
30	K1	0.125	0.125	0.125	0.8	0.083(22)	16
	Cs2	0.125	0.125	0.125	0.2	0.083	16
	Al3	0.66587(18)	0.58413	0.125	0.33	0.21(4)	48
	Si4	0.66587	0.584129	0.125	0.67	0.21	48
	O5	0.10019(16)	0.13313(8)	0.7391(4)	1	0.07(3)	96
39	K1	0.125	0.125	0.125	0.8	0.088(19)	16
	Cs2	0.125	0.125	0.125	0.2	0.088	16
	Al3	0.65818(17)	0.59182	0.125	0.33	0.30(5)	48
	Si4	0.65818	0.591822	0.125	0.67	0.3	48
	O5	0.11503(21)	0.12994(12)	0.7062(4)	1	0.38(7)	96
238	K1	0.125	0.125	0.125	0.8	1.312	16
	Cs2	0.125	0.125	0.125	0.2	1.31182	16
	Al3	0.66949	0.58051	0.125	0.33	0.55	48
	Si4	0.669488	0.58051	0.125	0.67	0.549651	48
	O5	0.09357(14)	0.13326(8)	0.7526(4)	1	0.01	96
365	K1	0.125	0.125	0.125	0.8	0.107(12)	16
	Cs2	0.125	0.125	0.125	0.2	0.107	16
	Al3	0.65951(18)	0.59049	0.125	0.33	0.066(9)	48
	Si4	0.65951	0.590495	0.125	0.67	0.066	48
	O5	0.11241(21)	0.13089(12)	0.7121(4)	1	0.042(10)	96
427	K1	0.125	0.125	0.125	0.8	0.117	16
	Cs2	0.125	0.125	0.125	0.2	0.117(4)	16
	Al3	0.66266(17)	0.58734	0.125	0.33	0.094(4)	48
	Si4	0.66266	0.58734	0.125	0.67	0.094	48
	O5	0.10635(16)	0.13233(10)	0.7257(3)	1	0.084(5)	96
485	K1	0.125	0.125	0.125	0.8	0.1098	16
	Cs2	0.125	0.125	0.125	0.2	0.1098(25)	16
	Al3	0.66170(13)	0.5883	0.125	0.33	0.0521(18)	48
	Si4	0.6617	0.588298	0.125	0.67	0.0521	48
	O5	0.10832(12)	0.13199(8)	0.72133(24)	1	0.0714(27)	96
601	K1	0.125	0.125	0.125	0.8	0.1108(29)	16
	Cs2	0.125	0.125	0.125	0.2	0.1108	16

Table 12 (cont.)

	Al3	0.66169(15)	0.58831	0.125	0.33	0.0408(17)	48
	Si4	0.66169	0.588309	0.125	0.67	0.0408	48
	O5	0.10823(14)	0.13196(9)	0.72140(28)	1	0.0687(31)	96
	K1	0.125	0.125	0.125	0.8	0.1246	16
	Cs2	0.125	0.125	0.125	0.2	0.1246(27)	16
820	Al3	0.66170(12)	0.5883	0.125	0.33	0.0448(15)	48
	Si4	0.6617	0.588301	0.125	0.67	0.0448	48
	O5	0.10821(12)	0.13197(8)	0.72149(23)	1	0.0683(25)	96

Table 13 – Empirical atomic parameters for c-$K_{0.6}Cs_{0.4}[AlSi_2O_6]$ through the temperature range

Temp.	Label	X	Y	Z	Occ.	U_iso	Mult.
30	Al1	0.0593	0.3957	0.1656	0.33	0.054	16
	O2	0.1286(23)	0.309(5)	0.121(3)	1	0.04(4)	16
	Si3	0.0593(6)	0.3957(6)	0.1656(6)	0.67	0.054(20)	16
	K4	0.3722(17)	0.3730(17)	0.1232(27)	0.6	0.10(11)	16
	Cs5	0.3722	0.373	0.1232	0.4	0.048(29)	16
358	Al1	0.125	0.66176(10)	0.58824	0.33	0.0430(11)	48
	O2	0.02819(18)	0.11799(6)	0.35800(9)	1	0.0709(19)	96
	Si3	0.125	0.66176	0.588244	0.67	0.043	48
	K4	0.125	0.125	0.125	0.6	0.0879(11)	16
	Cs5	0.125	0.125	0.125	0.4	0.0879	16
484	Al1	0.125	0.66169(10)	0.58831	0.33	0.0383(10)	48
	O2	0.02839(18)	0.11800(6)	0.35810(9)	1	0.0663(19)	96
	Si3	0.125	0.66169	0.588307	0.67	0.0383	48
	K4	0.125	0.125	0.125	0.6	0.096	16
	Cs5	0.125	0.125	0.125	0.4	0.0960(13)	16
608	Al1	0.125	0.66173(10)	0.58827	0.33	0.0317(9)	48
	O2	0.02840(18)	0.11802(6)	0.35809(9)	1	0.0609(18)	96
	Si3	0.125	0.66173	0.588266	0.67	0.0317	48
	K4	0.125	0.125	0.125	0.6	0.0975	16
	Cs5	0.125	0.125	0.125	0.4	0.0975(13)	16
728	Al1	0.125	0.66176(10)	0.58824	0.33	0.0278(9)	48
	O2	0.02833(19)	0.11801(7)	0.35807(10)	1	0.0582(19)	96
	Si3	0.125	0.66176	0.588241	0.67	0.0278	48
	K4	0.125	0.125	0.125	0.6	0.1012	16
	Cs5	0.125	0.125	0.125	0.4	0.1012(14)	16
846	Al1	0.125	0.66174(11)	0.58826	0.33	0.0289(10)	48
	O2	0.02839(21)	0.11802(7)	0.35810(11)	1	0.0599(20)	96
	Si3	0.125	0.66174	0.58826	0.67	0.0289	48
	K4	0.125	0.125	0.125	0.6	0.1092	16
	Cs5	0.125	0.125	0.125	0.4	0.1092(17)	16
957	Al1	0.125	0.66174(12)	0.58826	0.33	0.0298(11)	48
	O2	0.02836(23)	0.11803(8)	0.35810(12)	1	0.0627(23)	96

Table 13 (cont.)

	Si3	0.125	0.66174	0.588264	0.67	0.0298	48
	K4	0.125	0.125	0.125	0.6	0.1169(19)	16
	Cs5	0.125	0.125	0.125	0.4	0.1169	16
1061	Al1	0.125	0.66173(12)	0.58827	0.33	0.0301(11)	48
	O2	0.02842(22)	0.11804(7)	0.35813(11)	1	0.0631(23)	96
	Si3	0.125	0.66173	0.588266	0.67	0.0301	48
	K4	0.125	0.125	0.125	0.6	0.124	16
	Cs5	0.125	0.125	0.125	0.4	0.1240(20)	16
1160	Al1	0.125	0.66173(7)	0.58827	0.33	0.0358(7)	48
	O2	0.02841(13)	0.11805(4)	0.35816(6)	1	0.0592(12)	96
	Si3	0.125	0.66173	0.588269	0.67	0.0358	48
	K4	0.125	0.125	0.125	0.6	0.1313(12)	16
	Cs5	0.125	0.125	0.125	0.4	0.1313	16
1250	Al1	0.125	0.66170(7)	0.5883	0.33	0.0375(7)	48
	O2	0.02846(13)	0.11805(4)	0.35821(6)	1	0.0603(13)	96
	Si3	0.125	0.6617	0.588304	0.67	0.0375	48
	K4	0.125	0.125	0.125	0.6	0.1404(13)	16
	Cs5	0.125	0.125	0.125	0.4	0.1404	16
1332	Al1	0.125	0.66168(7)	0.58832	0.33	0.0372(7)	48
	O2	0.02854(13)	0.11807(4)	0.35825(6)	1	0.0615(13)	96
	Si3	0.125	0.66168	0.588319	0.67	0.0372	48
	K4	0.125	0.125	0.125	0.6	0.1495	16
	Cs5	0.125	0.125	0.125	0.4	0.1495(14)	16
1414	Al1	0.125	0.66169(7)	0.58831	0.33	0.0374(8)	48
	O2	0.02850(13)	0.11807(4)	0.35824(7)	1	0.0631(15)	96
	Si3	0.125	0.66169	0.588314	0.67	0.0374	48
	K4	0.125	0.125	0.125	0.6	0.18(3)	16
	Cs5	0.125	0.125	0.125	0.4	0.147(13)	16
1493	Al1	0.125	0.66162(8)	0.58838	0.33	0.0366(8)	48
	O2	0.02861(15)	0.11807(5)	0.35831(8)	1	0.0626(15)	96
	Si3	0.125	0.66162	0.588379	0.67	0.0366	48
	K4	0.125	0.125	0.125	0.6	0.1751(19)	16
	Cs5	0.125	0.125	0.125	0.4	0.1751	16
1562	Al1	0.125	0.66168(8)	0.58832	0.33	0.0385(9)	48
	O2	0.02855(15)	0.11807(5)	0.35828(8)	1	0.0645(16)	96
	Si3	0.125	0.66168	0.588323	0.67	0.0385	48
	K4	0.125	0.125	0.125	0.6	0.1786(19)	16
	Cs5	0.125	0.125	0.125	0.4	0.1786	16

Table 14 – Empirical atomic parameters for $K_{0.4}Cs_{0.6}[AlSi_2O_6]$ through the temperature range

Temp.	Label	X	Y	Z	Occ.	U_iso	Mult.
30	K1	0.125	0.125	0.125	0.4	0.0821	16
	Cs2	0.125	0.125	0.125	0.6	0.0821(30)	16
	Al3	0.6629	0.5871	0.125	0.33	0.054(4)	48
	Si4	0.6629	0.5871	0.125	0.67	0.054	48
	O5	0.10686(27)	0.13220(17)	0.7244(6)	1	0.044(6)	96
252	K1	0.125	0.125	0.125	0.4	0.0741	16
	Cs2	0.125	0.125	0.125	0.6	0.0741(7)	16
	Al3	0.66202(9)	0.58798	0.125	0.33	0.0381(8)	48
	Si4	0.66202	0.587976	0.125	0.67	0.0381	48
	O5	0.10766(8)	0.13206(5)	0.72255(15)	1	0.0466(15)	96
359	K1	0.125	0.125	0.125	0.4	0.0786	16
	Cs2	0.125	0.125	0.125	0.6	0.0786(7)	16
	Al3	0.66191(7)	0.58809	0.125	0.33	0.0311(7)	48
	Si4	0.66191	0.588093	0.125	0.67	0.0311	48
	O5	0.10790(7)	0.13199(4)	0.72209(13)	1	0.0407(12)	96
470	K1	0.125	0.125	0.125	0.4	0.098	16
	Cs2	0.125	0.125	0.125	0.6	0.098(5)	16
	Al3	0.6614(5)	0.5886	0.125	0.33	0.034(5)	48
	Si4	0.6614	0.588595	0.125	0.67	0.034	48
	O5	0.1086(4)	0.13197(30)	0.7208(8)	1	0.047(10)	96
607	K1	0.125	0.125	0.125	0.4	0.1	16
	Cs2	0.125	0.125	0.125	0.6	0.100(5)	16
	Al3	0.6618(4)	0.5882	0.125	0.33	0.031(4)	48
	Si4	0.6618	0.58824	0.125	0.67	0.031	48
	O5	0.1082(4)	0.13194(26)	0.7216(7)	1	0.040(7)	96
700	K1	0.125	0.125	0.125	0.4	0.093	16
	Cs2	0.125	0.125	0.125	0.6	0.093(5)	16
	Al3	0.6616(4)	0.5884	0.125	0.33	0.026(3)	48
	Si4	0.6616	0.588401	0.125	0.67	0.026	48
	O5	0.1083(4)	0.13189(25)	0.7212(7)	1	0.062(7)	96
823	K1	0.125	0.125	0.125	0.4	0.101	16
	Cs2	0.125	0.125	0.125	0.6	0.101(7)	16

Table 14 (cont.)

	Al3	0.6618(5)	0.5882	0.125	0.33	0.031(4)	48
	Si4	0.6618	0.588217	0.125	0.67	0.031	48
	O5	0.1081(5)	0.13199(31)	0.7218(10)	1	0.047(8)	96
922	K1	0.125	0.125	0.125	0.4	0.105(7)	16
	Cs2	0.125	0.125	0.125	0.6	0.105	16
	Al3	0.6616(5)	0.5884	0.125	0.33	0.031(5)	48
	Si4	0.6616	0.588368	0.125	0.67	0.031	48
	O5	0.1084(5)	0.13195(32)	0.7212(10)	1	0.042(9)	96
1041	K1	0.125	0.125	0.125	0.4	0.116(8)	16
	Cs2	0.125	0.125	0.125	0.6	0.116	16
	Al3	0.6613(5)	0.5887	0.125	0.33	0.036(4)	48
	Si4	0.6613	0.588659	0.125	0.67	0.036	48
	O5	0.1088(5)	0.13184(27)	0.7202(9)	1	0.042(8)	96
1116	K1	0.125	0.125	0.125	0.4	0.135	16
	Cs2	0.125	0.125	0.125	0.6	0.135(10)	16
	Al3	0.6611(5)	0.5889	0.125	0.33	0.040(5)	48
	Si4	0.6611	0.588889	0.125	0.67	0.04	48
	O5	0.1092(5)	0.13172(28)	0.7194(10)	1	0.040(7)	96
1206	K1	0.125	0.125	0.125	0.4	0.143	16
	Cs2	0.125	0.125	0.125	0.6	0.143(11)	16
	Al3	0.6612(5)	0.5888	0.125	0.33	0.039(5)	48
	Si4	0.6612	0.588768	0.125	0.67	0.039	48
	O5	0.1092(5)	0.13169(31)	0.7193(11)	1	0.045(7)	96
1298	K1	0.125	0.125	0.125	0.4	0.143	16
	Cs2	0.125	0.125	0.125	0.6	0.143(10)	16
	Al3	0.6615(5)	0.5885	0.125	0.33	0.036(5)	48
	Si4	0.6615	0.588474	0.125	0.67	0.036	48
	O5	0.1087(5)	0.13178(30)	0.7206(11)	1	0.053(8)	96
1368	K1	0.125	0.125	0.125	0.4	0.141	16
	Cs2	0.125	0.125	0.125	0.6	0.141(8)	16
	Al3	0.6618(5)	0.5882	0.125	0.33	0.038(4)	48
	Si4	0.6618	0.588188	0.125	0.67	0.038	48
	O5	0.1082(5)	0.13192(26)	0.7217(10)	1	0.065(7)	96
1458	K1	0.125	0.125	0.125	0.4	0.151	16
	Cs2	0.125	0.125	0.125	0.6	0.151(10)	16
	Al3	0.6621(5)	0.5879	0.125	0.33	0.036(5)	48
	Si4	0.6621	0.587866	0.125	0.67	0.036	48

Table 14 (cont.)

	O5	0.1076(5)	0.13203(29)	0.7229(10)	1	0.049(9)	96
1533	K1	0.125	0.125	0.125	0.4	0.14	16
	Cs2	0.125	0.125	0.125	0.6	0.140(8)	16
	Al3	0.6620(4)	0.588	0.125	0.33	0.038(5)	48
	Si4	0.662	0.588003	0.125	0.67	0.038	48
	O5	0.1076(4)	0.13205(26)	0.7230(9)	1	0.082(10)	96

Table 15 – Empirical atomic parameters for $K_{0.2}Cs_{0.8}[AlSi_2O_6]$ through the temperature range

Temp.	Label	X	Y	Z	Occ.	U_iso	Mult.
30	K1	0.125	0.125	0.125	0.2	0.0728	16
	Cs2	0.125	0.125	0.125	0.8	0.0728(11)	16
	Al3	0.66162(13)	0.58838	0.125	0.33	0.0449(19)	48
	Si4	0.66162	0.588379	0.125	0.67	0.0449	48
	O5	0.10828(12)	0.13195(8)	0.72132(25)	1	0.0543(29)	96
32	K1	0.125	0.125	0.125	0.2	0.0621	16
	Cs2	0.125	0.125	0.125	0.8	0.0621(12)	16
	Al3	0.6636(7)	0.5864	0.125	0.33	0.0552(26)	48
	Si4	0.6636	0.58636	0.125	0.67	0.0552	48
	O5	0.0989(7)	0.1342(6)	0.7174(7)	1	0.056(4)	96
227	K1	0.125	0.125	0.125	0.2	0.0613	16
	Cs2	0.125	0.125	0.125	0.8	0.0613(5)	16
	Al3	0.66155(6)	0.58845	0.125	0.33	0.0270(9)	48
	Si4	0.66155	0.588452	0.125	0.67	0.027	48
	O5	0.10840(6)	0.13191(4)	0.72119(12)	1	0.0373(14)	96
352	K1	0.125	0.125	0.125	0.2	0.0673	16
	Cs2	0.125	0.125	0.125	0.8	0.0673(6)	16
	Al3	0.66150(6)	0.5885	0.125	0.33	0.0292(10)	48
	Si4	0.6615	0.588496	0.125	0.67	0.0292	48
	O5	0.10851(6)	0.13188(4)	0.72098(13)	1	0.0403(16)	96
475	K1	0.125	0.125	0.125	0.2	0.0771	16
	Cs2	0.125	0.125	0.125	0.8	0.0771(7)	16
	Al3	0.66150(6)	0.5885	0.125	0.33	0.0307(10)	48
	Si4	0.6615	0.588498	0.125	0.67	0.0307	48
	O5	0.10850(6)	0.13188(4)	0.72102(13)	1	0.0421(17)	96
597	K1	0.125	0.125	0.125	0.2	0.0799(8)	16
	Cs2	0.125	0.125	0.125	0.8	0.0799	16
	Al3	0.66143(7)	0.58856	0.125	0.33	0.0320(12)	48
	Si4	0.66143	0.58855	0.125	0.67	0.032	48
	O5	0.10862(7)	0.13185(4)	0.72074(15)	1	0.0428(19)	96

Table 15 (cont.)

715	K1	0.125	0.125	0.125	0.2	0.0891	16
	Cs2	0.125	0.125	0.125	0.8	0.0891(10)	16
	Al3	0.66141(7)	0.58859	0.125	0.33	0.0328(12)	48
	Si4	0.66141	0.588591	0.125	0.67	0.0328	48
	O5	0.10871(7)	0.13183(4)	0.72058(14)	1	0.0424(20)	96
824	K1	0.125	0.125	0.125	0.2	0.0908	16
	Cs2	0.125	0.125	0.125	0.8	0.0908(11)	16
	Al3	0.66148(7)	0.58852	0.125	0.33	0.0310(13)	48
	Si4	0.66148	0.588517	0.125	0.67	0.031	48
	O5	0.10854(7)	0.13187(4)	0.72095(14)	1	0.0406(21)	96
924	K1	0.125	0.125	0.125	0.2	0.0993	16
	Cs2	0.125	0.125	0.125	0.8	0.0993(11)	16
	Al3	0.66141(7)	0.58859	0.125	0.33	0.0348(13)	48
	Si4	0.66141	0.588589	0.125	0.67	0.0348	48
	O5	0.10868(7)	0.13183(4)	0.72063(14)	1	0.0439(21)	96
1027	K1	0.125	0.125	0.125	0.2	0.0993	16
	Cs2	0.125	0.125	0.125	0.8	0.0993(11)	16
	Al3	0.66148(7)	0.58852	0.125	0.33	0.0320(13)	48
	Si4	0.66148	0.588521	0.125	0.67	0.032	48
	O5	0.10856(7)	0.13187(4)	0.72089(15)	1	0.0460(21)	96
1115	K1	0.125	0.125	0.125	0.2	0.1252	16
	Cs2	0.125	0.125	0.125	0.8	0.1252(15)	16
	Al3	0.66157(10)	0.58843	0.125	0.33	0.0445(16)	48
	Si4	0.66157	0.588427	0.125	0.67	0.0445	48
	O5	0.10838(10)	0.13192(6)	0.72126(20)	1	0.0601(26)	96
1188	K1	0.125	0.125	0.125	0.2	0.1181	16
	Cs2	0.125	0.125	0.125	0.8	0.1181(14)	16
	Al3	0.66161(9)	0.58839	0.125	0.33	0.0404(14)	48
	Si4	0.66161	0.588394	0.125	0.67	0.0404	48
	O5	0.10832(9)	0.13193(5)	0.72139(19)	1	0.0566(24)	96
1258	K1	0.125	0.125	0.125	0.2	0.1252	16
	Cs2	0.125	0.125	0.125	0.8	0.1252(15)	16
	Al3	0.66157(10)	0.58843	0.125	0.33	0.0445(16)	48
	Si4	0.66157	0.588427	0.125	0.67	0.0445	48
	O5	0.10838(10)	0.13192(6)	0.72126(20)	1	0.0601(26)	96
1333	K1	0.125	0.125	0.125	0.2	0.135	16
	Cs2	0.125	0.125	0.125	0.8	0.1350(16)	16

Table 15 (cont.)

	Al3	0.66161(10)	0.58839	0.125	0.33	0.0466(16)	48
	Si4	0.66161	0.58839	0.125	0.67	0.0466	48
	O5	0.10830(10)	0.13193(6)	0.72145(20)	1	0.0625(26)	96
1373	K1	0.125	0.125	0.125	0.2	0.1374	16
	Cs2	0.125	0.125	0.125	0.8	0.1374(17)	16
	Al3	0.66158(10)	0.58842	0.125	0.33	0.0477(17)	48
	Si4	0.66158	0.58842	0.125	0.67	0.0477	48
	O5	0.10836(10)	0.13192(6)	0.72133(20)	1	0.0629(27)	96
1409	K1	0.125	0.125	0.125	0.2	0.1(4)	16
	Cs2	0.125	0.125	0.125	0.8	0.138(30)	16
	Al3	0.66155(11)	0.58845	0.125	0.33	0.05(8)	48
	Si4	0.66155	0.58845	0.125	0.33	0.05	48
	O5	0.10836(11)	0.13192(6)	0.72133(22)	1	0.062(4)	96

Table 16 – Empirical atomic parameters for $Cs[AlSi_2O_6]$ through the temperature range

Temp.	Label	X	Y	Z	Occ.	U_iso	Mult.
30	Cs1	0.125	0.125	0.125	1	0.1340(15)	16
	Al2	0.66208(12)	0.58792	0.125	0.33	0.0398(16)	48
	Si3	0.66208	0.587917	0.125	0.67	0.0398	48
	O4	0.10751(12)	0.13209(7)	0.72323(23)	1	0.0505(25)	96
154	Cs1	0.125	0.125	0.125	1	0.0637(5)	16
	Al2	0.66205(9)	0.58795	0.125	0.33	0.0162(7)	48
	Si3	0.66205	0.587949	0.125	0.67	0.0162	48
	O4	0.10758(8)	0.13210(5)	0.72283(16)	1	0.0276(13)	96
289	Cs1	0.125	0.125	0.125	1	0.0703(6)	16
	Al2	0.66204(9)	0.58796	0.125	0.33	0.0175(9)	48
	Si3	0.66204	0.58796	0.125	0.67	0.0175	48
	O4	0.10761(9)	0.13209(6)	0.72281(17)	1	0.0281(15)	96
407	Cs1	0.125	0.125	0.125	1	0.0741(8)	16
	Al2	0.66202(12)	0.58798	0.125	0.33	0.0128(11)	48
	Si3	0.66202	0.587983	0.125	0.67	0.0128	48
	O4	0.10762(12)	0.13208(8)	0.72272(23)	1	0.0338(21)	96
494	Cs1	0.125	0.125	0.125	1	0.0825(7)	16
	Al2	0.66201(9)	0.58799	0.125	0.33	0.0221(10)	48
	Si3	0.66201	0.587995	0.125	0.67	0.0221	48
	O4	0.10760(9)	0.13210(6)	0.72287(17)	1	0.0334(16)	96
578	Cs1	0.125	0.125	0.125	1	0.0861(9)	16
	Al2	0.66203(11)	0.58797	0.125	0.33	0.0197(12)	48
	Si3	0.66203	0.587965	0.125	0.67	0.0197	48
	O4	0.10755(11)	0.13211(7)	0.72295(21)	1	0.0370(21)	96
658	Cs1	0.125	0.125	0.125	1	0.0915(8)	16
	Al2	0.66207(10)	0.58793	0.125	0.33	0.0245(11)	48
	Si3	0.66207	0.587932	0.125	0.67	0.0245	48
	O4	0.10753(9)	0.13212(6)	0.72306(19)	1	0.0338(18)	96
741	Cs1	0.125	0.125	0.125	1	0.0962(9)	16
	Al2	0.66208(10)	0.58792	0.125	0.33	0.0260(11)	48
	Si3	0.66208	0.587923	0.125	0.67	0.026	48

Table 16 (cont.)

	O4	0.10752(9)	0.13212(6)	0.72311(18)	1	0.0339(17)	96
815	Cs1	0.125	0.125	0.125	1	0.1003(8)	16
	Al2	0.66209(9)	0.58791	0.125	0.33	0.0275(10)	48
	Si3	0.66209	0.587906	0.125	0.67	0.0275	48
	O4	0.10749(9)	0.13212(6)	0.72316(17)	1	0.0361(17)	96
889	Cs1	0.125	0.125	0.125	1	0.1046(9)	16
	Al2	0.66210(9)	0.5879	0.125	0.33	0.0285(10)	48
	Si3	0.6621	0.587899	0.125	0.67	0.0285	48
	O4	0.10749(9)	0.13211(6)	0.72317(17)	1	0.0375(17)	96
1002	Cs1	0.125	0.125	0.125	1	0.1079(10)	16
	Al2	0.66211(11)	0.58789	0.125	0.33	0.0294(12)	48
	Si3	0.66211	0.587891	0.125	0.67	0.0294	48
	O4	0.10746(10)	0.13213(7)	0.72321(20)	1	0.0398(20)	96
1098	Cs1	0.125	0.125	0.125	1	0.1148(10)	16
	Al2	0.66209(10)	0.58791	0.125	0.33	0.0330(11)	48
	Si3	0.66209	0.587909	0.125	0.67	0.033	48
	O4	0.10751(9)	0.13210(6)	0.72317(18)	1	0.0444(18)	96
1238	Cs1	0.125	0.125	0.125	1	0.1225(11)	16
	Al2	0.66207(10)	0.58793	0.125	0.33	0.0354(12)	48
	Si3	0.66207	0.587926	0.125	0.67	0.0354	48
	O4	0.10753(9)	0.13209(6)	0.72315(19)	1	0.0463(19)	96
1358	Cs1	0.125	0.125	0.125	1	0.1297(12)	16
	Al2	0.66206(10)	0.58794	0.125	0.33	0.0373(13)	48
	Si3	0.66206	0.587939	0.125	0.67	0.0373	48
	O4	0.10755(10)	0.13208(6)	0.72314(20)	1	0.0482(21)	96
1456	Cs1	0.125	0.125	0.125	1	0.1340(15)	16
	Al2	0.66208(12)	0.58792	0.125	0.33	0.0398(16)	48
	Si3	0.66208	0.587917	0.125	0.67	0.0398	48
	O4	0.10751(12)	0.13209(7)	0.72323(23)	1	0.0505(25)	96

Table 17 – Empirical mechanistic distortion parameters for $K[AlSi_2O_6]$ through the temperature range

	Framework Distortions						
Temp. (°C)	Tetrahedral flattening, Ring 1 (deg)	Ring 2 (deg)	Tetrahedral rotation, Ring 1, α (deg)	Ring 2 (deg)	Basal O-plane corrugation, Ring 1 (pm)	Ring 2 (pm)	W-W spacing [Å]
30(3)	0.02(8)	0.0(8)	103.8(3)	116.3(3)	73.1(2)	95.4(2)	5.9160(9)
320	0.00	-0.01	105	115.6	72.6	94.3	5.9731
425	0.00	0.00	105.7	115.3	74.3	94.3	5.9451
479	0.00	-0.01	106.4	115	62.8	354.6	5.9721
535 (t-phase)	0.00	0.00	107	114.6	74.3	88.6	5.9652
587 (t-phase)	0.01	0.00	108.4	114.1	83.3	86.8	5.8781
535 (c-phase)	0.00	0.00	110.3	110.3	83.6		5.8484
587 (c-phase)	0.05	0.05	111.1	111.1	81.3		5.8927
637	0.05	0.05	110.8	110.8	81.8		5.8649
690	0.05	0.05	110.8	110.8	81.6		5.8687
740	0.06	0.06	111	111	80.9		5.8716
858	0.06	0.06	110.9	110.9	81.2		5.876
944	0.04	0.04	111.2	111.2	80.2		5.8796
1042	0.05	0.05	111.1	111.1	80.3		5.8825
1130	0.05	0.05	111.1	111.1	80.3		5.885
1210	0.05	0.05	111.1	111.1	80.7		5.887
1284	0.05	0.05	111	111	80.9		5.8889
1360	0.05	0.05	111.1	111.1	80.8		5.8907
1452	0.05	0.05	111.1	111.1	80.8		5.8927

	Tetrahedral Distortions			
Temp. (°C)	Avg. bond length (Å)	Distortion index	Quadratic elongation	Bond angle variance (deg^2)
30(3)	1.6372(9)	0.0192(2)	1.0008(3)	0.00(1)
320	1.6323	0.0142	1.0004	0
425	1.6308	0.0076	1.0001	0
479	1.6277	0.0079	1.0002	0
535 (t-phase)	1.6241	0.0126	1.0004	0
587 (t-phase)	1.626	0.0505	1.0055	0
535 (c-phase)	1.6024	0.0379	1.0024	0
587 (c-phase)	1.6151	0.02	1.0006	0.02
637	1.6077	0.0011	1	0.03
690	1.6087	0.006	1.0001	0.03
740	1.6095	0.0161	1.0004	0.03
858	1.6107	0.0126	1.0003	0.03
944	1.6121	0.034	1.0019	0.05
1042	1.6123	0.0246	1.001	0.02
1130	1.6129	0.0251	1.001	0.02
1210	1.6136	0.0202	1.0007	0.02
1284	1.6141	0.0184	1.0005	0.02
1360	1.6145	0.0199	1.0006	0.02
1452	1.6151	0.02	1.0006	0.02

Table 18 – Empirical mechanistic distortion parameters for $K_{0.8}Cs_{0.2}[AlSi_2O_6]$ through the temperature range

	Framework Distortions		
Temp. (°C)	Tetrahedral rotation, Ring 1(deg)	Ring 2 (deg)	W-W spacing [Å]
30(3) (t-phase)	104.85(8)	116.3(8)	6.0230(9)
39 (t-phase)	108.34	115.8	5.9530
365 (t-phase)	106.42	114.8	6.0340
30 (c-phase)	113.53		6.4688
39 (c-phase)	108.58		11.4185
365 (c-phase)	109.36		10.6385
427	111.44		5.8689
485	110.78		5.8803
601	110.78		5.8893
820	110.80		5.8980

	Tetrahedral Distortions			
Temp. (°C)	Avg. bond length (Å)	Distortion index	Quadratic elongation	Bond angle variance (deg^2)
30(3) (t-phase)	1.6596(9)	0.1536(2)	1.0551(3)	0.01(1)
39 (t-phase)	1.6563	0.1010	1.0231	0.02
365 (t-phase)	1.6897	0.2331	1.1842	0.01
30 (c-phase)	1.5973	0.1845	1.0582	0.00
39 (c-phase)	1.5996	0.1608	0.1608	0.00
365 (c-phase)	1.6066	0.0988	0.0988	0.01
427.0000	1.6083	0.0436	1.0031	0.01
485.0000	1.6117	0.0017	1.0000	0.20
601.0000	1.6141	0.0010	1.0000	0.02
820.0000	1.6165	0.0002	1.0000	0.01

Table 19 – Empirical mechanistic distortion parameters for $K_{0.6}Cs_{0.4}[AlSi_2O_6]$ through the temperature range

	Framework Distortions	
Temp. (°C)	Tetrahedral rotation (deg)	W-W spacing [Å]
30(3)	5.22(8)	5.8960(9)
358	9.19	5.8877
484	9.22	5.8969
608	9.22	5.9023
728	9.21	5.9060
846	9.22	5.9088
957	9.20	5.9111
1061	9.21	5.9130
1160	9.21	5.9145
1250	9.21	5.9157
1332	9.22	5.9166
1414	9.21	5.9172
1493	9.21	5.9177
1562	9.20	5.9193

	Tetrahedral Distortions			
Temp. (°C)	Avg. bond length (Å)	Distortion index	Quadratic elongation	Bond angle variance (deg^2)
30(3)	1.6529(9)	0.0472(2)	1.0047(3)	0.01(1)
358	1.6138	0.0032	1.0000	0.02
484	1.6163	0.0010	1.0000	0.02
608	1.6178	0.0012	1.0000	0.02
728	1.6188	0.0020	1.0000	0.02
846	1.6195	0.0013	1.0000	0.02
957	1.6201	0.0015	1.0000	0.02
1061	1.6206	0.0009	1.0000	0.02
1160	1.6209	0.0009	1.0000	0.01
1250	1.6212	0.0002	1.0000	0.01
1332	1.6214	0.0007	1.0000	0.01
1414	1.6215	0.0003	1.0000	0.01
1493	1.6217	0.0018	1.0000	0.00
1562	1.6221	0.0009	1.0000	0.01

Table 20 – Empirical mechanistic distortion parameters for $K_{0.4}Cs_{0.6}[AlSi_2O_6]$ through the temperature range

	Framework Distortions	
Temp. (°C)	Tetrahedral rotation (deg)	W-W spacing [Å]
30(3)	8.77(8)	5.8877(9)
232	9.07	5.8981
359	9.13	5.9074
470	9.27	5.9118
607	9.17	5.9156
700	9.27	5.9179
823	9.16	5.9212
922	9.26	5.9226
1041	9.36	5.9238
1116	9.46	5.9250
1206	9.46	5.9258
1298	9.26	5.9264
1368	9.16	5.9270
1458	8.96	5.9287
1533	8.96	5.9292

	Tetrahedral Distortions			
Temp. (°C)	Avg. bond length (Å)	Distortion index	Quadratic elongation	Bond angle variance (deg^2)
30(3)	1.6099(9)	0.0339(2)	1.0018(3)	0.2(1)
232	1.6166	0.0116	1.0002	0.03
359	1.6190	0.0066	1.0001	0.02
470	1.6203	0.0085	1.0001	0.01
607	1.6211	0.0013	1.0000	0.02
700	1.6218	0.0034	1.0000	0.01
823	1.6227	0.0032	1.0000	0.01
922	1.6231	0.0036	1.0000	0.01
1041	1.6235	0.0144	1.0000	0.01
1116	1.6237	0.0231	1.0000	0.00
1206	1.6239	0.0232	1.0000	0.01
1298	1.6238	0.0098	1.0000	0.01
1368	1.6240	0.0021	1.0000	0.01
1458	1.6246	0.0149	1.0004	0.02
1533	1.6247	0.0150	1.0004	0.00

Table 21 – Empirical mechanistic distortion parameters for $K_{0.2}Cs_{0.8}[AlSi_2O_6]$ through the temperature range

	Framework Distortions	
Temp. (°C)	Tetrahedral rotation (deg)	W-W spacing [Å]
30(3)	9.25(8)	5.9113(9)
227	9.25	5.9245
352	9.28	5.9282
475	9.27	5.9307
597	9.30	5.9328
715	9.33	5.9348
824	9.28	5.9364
924	9.32	5.9378
1027	9.28	5.9390
1115	9.24	5.9400
1188	9.21	5.9416
1258	9.23	5.9427
1333	9.20	5.9439
1373	9.21	5.9448
1409	9.21	5.9456

	Tetrahedral Distortions			
Temp. (°C)	Avg. bond length (Å)	Distortion index	Quadratic elongation	Bond angle variance (deg^2)
30(3)	1.6201(9)	0.0022(2)	1.0000(3)	0.0(1)
227	1.6235	0.0041	1.0000	0.0
352	1.6245	0.0063	1.0001	0.0
475	1.6252	0.0060	1.0000	0.0
597	1.6257	0.0089	1.0000	0.0
715	1.6262	0.0106	1.0000	0.0
824	1.6267	0.0068	1.0000	0.0
924	1.6271	0.0101	1.0000	0.0
1027	1.6274	0.0073	1.0000	0.0
1115	1.6277	0.0040	1.0000	0.0
1188	1.6282	0.0019	1.0000	0.0
1258	1.6285	0.0033	1.0000	0.0
1333	1.6288	0.0014	1.0000	0.0
1373	1.6290	0.0027	1.0000	0.0
1409	1.6293	0.0029	1.0000	0.0

Table 22 – Empirical mechanistic distortion parameters for $Cs[AlSi_2O_6]$ through the temperature range

	Framework Distortions			
Temp. (°C)	Tetrahedral flattening (deg)	Tetrahedral rotation (deg)	Basal O-plane corrugation (pm)	W-W spacing [Å]
30(3)	0.03(8)	9.06(8)	106.0(2)	5.9431(9)
154	0.05	9.02	81.9	5.9442
289	0.05	9.02	81.9	5.9459
407	0.05	9.04	81.0	5.9470
494	0.03	9.00	81.9	5.9470
578	0.04	9.00	81.9	5.9474
658	0.04	8.97	81.7	5.9482
741	0.04	8.96	80.8	5.9494
815	0.03	8.95	81.7	5.9505
889	0.04	8.95	81.7	5.9518
1002	0.04	8.95	81.7	5.9534
1098	1.09	8.94	81.7	5.9551
1238	0.03	8.93	81.7	5.9570
1358	0.03	8.93	81.7	5.9590
1456	0.03	8.91	81.6	5.9610

	Tetrahedral Distortions			
Temp. (°C)	Avg. bond length (Å)	Distortion index	Quadratic elongation	Bond angle variance (deg^2)
30(3)	1.6290(9)	0.0124(2)	1.0002(3)	0.0(1)
154	1.6292	0.0142	1.0003	0.02
289	1.6296	0.0139	1.0003	0.02
407	1.6299	0.0130	1.0003	0.02
494	1.6299	0.0142	1.0003	0.03
578	1.6300	0.0150	1.0004	0.01
658	1.6302	0.0162	1.0004	0.01
741	1.6304	0.0167	1.0004	0.01
815	1.6308	0.0172	1.0005	0.01
889	1.6311	0.0173	1.0005	0.01
1002	1.6316	0.0178	1.0005	0.01
1098	1.6145	0.0199	1.0006	0.02
1238	1.6324	0.0169	1.0005	0.01
1358	1.6329	0.0167	1.0004	0.00
1456	1.6334	0.0176	1.0005	0.00

Table 23 – Empirical data for $Rb[AlSi_2O_6]$ through the temperature range

T (°C)	Lattice Parameter a (Å)	Lattice Parameter c (Å)	Unit Cell Volume (Å^3)	CTE (10^-5/°C)
30	13.4191(5)	13.8741(5)	2498.3403(2)	2.9288(4)
73	13.4305	13.8680	2501.4867	6.4715
379	13.6045	13.8034	2554.7667	6.3569
385	13.6063	13.7995	2554.7208	6.8740
456	13.6686	13.7638	2571.4994	7.8677
506	13.7364	13.7364	2591.9035	6.5988
657	13.7537	13.7537	2601.7085	5.8610
772	13.7630	13.7630	2606.9898	5.8722
795	13.7693	13.7693	2610.5715	5.0235
946	13.7741	13.7741	2613.3026	4.7122
1025	13.7779	13.7779	2615.4774	4.4664
1097	13.7813	13.7813	2617.4028	4.2651
1157	13.7831	13.7831	2618.4285	4.0870
1233	13.7879	13.7879	2621.1765	3.9315
1304	13.7920	13.7920	2623.4756	3.8722
1335	13.7939	13.7939	2624.5885	3.5676
1490	13.8007	13.8007	2628.4719	3.4876
1559	13.8061	13.8061	2631.5643	3.3787
1638	13.8105	13.8105	2634.0754	3.3817
1642	13.8113	13.8113	2634.5332	2.9288

Table 24 – Empirical data for $K[AlSiO_4]$ through the temperature range

T (°C)	Lattice parameter a (Å)	Lattice parameter c (Å)	Unit cell volume (Å^3)	CTE (10^-5/°C)
30(3)	5.2778(6)	8.7426(6)	210.90(5)	1.9355(3)
640	5.2989	8.7754	213.39	3.3284
748	5.3233	8.7991	215.94	3.5531
808	5.3300	8.8090	216.73	3.6118
861	5.3351	8.8124	217.23	3.8353
909	5.3409	8.8251	218.01	3.8865
956	5.3451	8.8305	218.49	3.9407
1001	5.3491	8.8365	218.97	3.9202
1046	5.3522	8.8396	219.30	3.9761
1083	5.3553	8.8468	219.73	3.9220
1135	5.3582	8.8497	220.04	3.9381
1163	5.3604	8.8535	220.31	4.0353
1178	5.3630	8.8595	220.67	3.9809
1233	5.3657	8.8636	221.00	4.0350
1258	5.3680	8.8699	221.35	4.0699
1336	5.3730	8.8839	222.11	4.1309
1412	5.3774	8.9020	222.94	4.2501
1477	5.3814	8.9263	223.87	1.9355

Table 25 – Empirical data for compressive loading tests

KGPMB		KGPF	
ID	Ultimate Compressive Strength (MPa)	ID	Ultimate Compressive Strength (MPa)
1	57.45(8)	1	58.46(3)
2	61.62	2	58.79
3	62.81	3	58.80
4	62.92	4	60.44
5	64.85	5	61.38
6	65.66	6	61.92
7	66.66	7	62.04
8	69.61	8	64.12
9	72.28	9	64.22
10	75.81	10	65.06
11	75.97		

Table 26 – Empirical data for flexural loading tests

KGPMB		KGPF	
ID	Ultimate Flexural Strength (MPa)	ID	Ultimate Flexural Strength (MPa)
1	5.17(6)	1	5.03(3)
2	7.89	2	5.08
3	10.23	3	5.70
4	10.86	4	5.84
5	11.77	5	6.58
6	12.43	6	6.91
7	12.70	7	9.42
8	14.85	8	10.42
9	15.21	9	11.67
10	16.53	10	11.75
		11	12.97
		12	14.82

Table 27 – Empirical data for shear loading tests

KGPMB		KGPF	
ID	Ultimate Shear Stress (MPa)	ID	Ultimate Shear Stress (MPa)
1	6.26(2)	1	5.15(9)
2	11.36	2	5.85
3	7.70	3	6.65
4	7.42	4	6.77
5	8.10	5	6.77
6	6.02	6	6.81
		7	7.78
		8	8.36
		9	8.37
		10	9.62
		11	10.81

Table 28 – Empirical data for fracture toughness tests

KGPMB		KGPF	
ID	Fracture Toughness (MPa√m)	ID	Fracture Toughness (MPa√m)
1	1.88(8)	1	1.17(9)
2	2.50	2	1.34
3	3.32	3	1.35
4	3.53	4	1.40
5	4.18	5	1.43
6	4.50	6	4.61
7	4.70	7	9.77
8	5.64		
9	5.85		
10	8.57		
11	9.45		
12	10.04		